



# UNIVERSITÀ DI PISA

Department of Physics "E. Fermi"

Master's Degree in Physics

Study of monolithic CMOS pixel sensors in the  
Belle II experiment upgrade

Candidate:

**Mara Stefania Caló**

Supervisor:

**Prof. Francesco Forti**

Academic year 2022/2023

# Contents

<b>Introduction</b>	<b>5</b>
<b>1 Belle II and SuperKEKB (SKB) accelerator</b>	<b>7</b>
1.1 Physics program of the B-factories . . . . .	7
1.1.1 Open questions in SM . . . . .	8
1.1.2 Peculiarity of asymmetric B factories . . . . .	8
1.2 SuperKEKB accelerator . . . . .	10
1.2.1 The facility . . . . .	10
1.2.2 "Nano-beam" scheme . . . . .	11
1.3 Belle II detector . . . . .	12
1.3.1 Vertex Detector (VXD) . . . . .	12
1.3.2 Central Drift Chamber (CDC) . . . . .	15
1.3.3 Particle identification system (TOP e ARICH) . . . . .	15
1.3.4 Electromagnetic calorimeter (ECL) . . . . .	16
1.3.5 $K_L$ muon detector (KLM) . . . . .	16
1.3.6 Trigger system . . . . .	17
1.4 Current state of data taking . . . . .	17
<b>2 Belle II Upgrade</b>	<b>19</b>
2.1 Purposes of the upgrade . . . . .	19
2.2 Background sources and limitations in Belle II . . . . .	19

2.2.1	Main background sources . . . . .	20
2.2.2	Current background status and future predictions . . . . .	21
2.3	Summary of possible VXD upgrade . . . . .	22
2.3.1	Depleted Field Effect Transistor (DEPFET) . . . . .	23
2.3.2	Thin and Fine-Pitch SVD . . . . .	24
2.3.3	CMOS Monolithic Active Pixels Sensor . . . . .	24
2.3.4	Silicon On Insulator (SOI) . . . . .	25
<b>3</b>	<b>CMOS MAPS sensors</b>	<b>27</b>
3.1	Semiconductor detectors . . . . .	27
3.1.1	Movement of charge carriers and signal formation in semiconductors . . . . .	28
3.1.2	The pn junctions as detector . . . . .	29
3.1.3	Metal-Oxide-Semiconductor (MOS) . . . . .	30
3.2	Hybrid and monolithic pixel sensors . . . . .	31
3.2.1	Hybrid pixel detector . . . . .	31
3.2.2	Monolithic pixel detector . . . . .	32
3.3	CMOS Monolithic Active Pixel Sensors technology . . . . .	33
3.3.1	MAPS pixel detectors . . . . .	33
3.3.2	Depleted MAPS pixel detectors . . . . .	34
3.3.3	Silicon On Insulator (SOI) technology . . . . .	35
3.4	History of Monopix developments . . . . .	36
3.4.1	Developments of DMAP devices . . . . .	36
3.4.2	TJ-Monopix line . . . . .	36
<b>4</b>	<b>VTX detector</b>	<b>42</b>
4.1	VTX Layout and mechanical structure . . . . .	42
4.1.1	iVTX . . . . .	43
4.1.2	oVTX . . . . .	44
4.2	Performance simulation . . . . .	47
4.2.1	VTX geometries . . . . .	47
4.2.2	Tracking efficiency at low momentum and impact parameter resolution . . . . .	47

4.2.3	Vertexing resolution . . . . .	48
4.3	OBELIX chip design . . . . .	51
4.3.1	Sensor specification . . . . .	51
4.3.2	Sensor implementation . . . . .	52
<b>5</b>	<b>TJ-Monopix2 characterization</b>	<b>55</b>
5.1	Matrix and flavors . . . . .	56
5.1.1	Flavors . . . . .	56
5.1.2	Pixel design . . . . .	57
5.1.2.1	Improved front-end circuit design . . . . .	57
5.2	Threshold and noise . . . . .	59
5.2.1	Injection circuit . . . . .	59
5.2.2	S-Curve method . . . . .	59
5.2.2.1	Normal FE . . . . .	60
5.2.2.2	Cascode FE . . . . .	62
5.2.2.3	HV-Cascode FE . . . . .	62
5.2.2.4	HV-Normal FE . . . . .	62
5.2.2.5	Summary Table . . . . .	64
5.2.3	Threshold dispersion and tuning . . . . .	64
5.2.3.1	First results from threshold tuning . . . . .	66
5.3	ToT calibration with internal injection . . . . .	67
5.3.1	Time Over Threshold (TOT) curves and fit . . . . .	69
5.4	Response to radioactive source and absolute calibration . . . . .	69
5.4.1	$^{55}\text{Fe}$ . . . . .	71
5.4.2	$^{241}\text{Am}$ . . . . .	71
5.4.3	$^{109}\text{Cd}$ . . . . .	71
5.4.4	Injection capacitance calibration . . . . .	72
5.4.5	Check on calibration curve ToT vs $Q_{inj}$ with radioactive sources . . . . .	76
5.5	Operation with low threshold . . . . .	76
5.5.1	Register optimization . . . . .	77

5.5.2	Comparison between data and simulation . . . . .	78
5.5.2.1	some nice picture of the optimized thr and tuning . . . . .	80
5.6	Cross talk issue and mitigation . . . . .	80
5.6.1	Hot pixel issue . . . . .	81
5.6.2	Hot pixel strategy (study) . . . . .	83
5.6.3	Cross-talk (Results) . . . . .	84
5.6.4	Mitigation . . . . .	86
5.6.4.1	Final results? . . . . .	88
5.7	Test Beam results . . . . .	88
5.7.1	Experimental apparatus and DUTs . . . . .	89
5.7.2	Hit detection efficiency measurements . . . . .	90
<b>6</b>	<b>Conclusions</b>	<b>92</b>
<b>Bibliography</b>		<b>93</b>

# Introduction

Belle II is a particle physics experiment located at the KEK laboratory in Tsukuba (Japan). The detector is a general-purpose spectrometer to study electron-positron collisions produced by the SuperKEKB accelerator, a second generation flavor-factory which operates at the luminosity frontier, holding the world record of instantaneous luminosity with  $L_{peak} = 4.7 \times 10^{34} \text{ cm}^{-2} \text{ s}^{-1}$ .

SuperKEKB is the upgrade of the preceding facility KEKB (operational from 1998 to 2016) and it consists in a 3 km-circumference asymmetric accelerator which collides electrons and positrons beams at a center-of-mass energy near the  $\Upsilon(4S)$  resonance ( $\sqrt{s} = 10.58 \text{ GeV}$ ). It started its data taking in March 2019.

In the next decade, the collider aims to collect an unrivaled dataset of  $50 \text{ ab}^{-1}$  (x50 Belle dataset, x100 BaBar dataset) and to reach a peak luminosity of  $6 \times 10^{35} \text{ cm}^{-2} \text{ s}^{-1}$ . This will allow to study the charge-parity violation in B mesons system with more precision and to search for new hints of physics beyond the Standard Model.

To achieve these challenging targets, it will be necessary a significant upgrade of the accelerator and its main components (like the injection system and the equipment nearby the interaction region), probably requiring the installation of a new vertex detector. As a matter of fact, to the increase in luminosity corresponds not only large data collected and greater possibility to study rare processes, but also higher doses of radiation and larger backgrounds, which could undermine the integrity and the operation of the Belle II detector. In particular the subdetectors which are closest to the beam pipe are those more exposed to severe conditions, like the vertex detector (VXD), composed of the inner pixel detector (PXD, made of layers of pixels) and the outermost silicon vertex detector (SVD, made of layers of strips). They allow the reconstruction of charged particle tracks and of decay vertices with high performance. Recent studies have shown that the current detector could operate efficiently up to a luminosity of  $L_{inst} = 2 \times 10^{35} \text{ cm}^{-2} \text{ s}^{-1}$ , but safety margins are not large. Consequently, in this context, different upgrade projects have been proposed, which intend to design a new vertex detector, making it more resistant even in harsher working conditions, while the luminosity will be gradually increased.

This work focuses especially on the VerTeX Detector (VTX) proposal (the one chosen for the upgrade), replacing the whole VXD with five layers of fully pixelated sensors based on the CMOS Depleted Monolithic Active Pixel Sensor (DMPAS) technology.

The good results achieved by the ALICE experiment (LHC, CERN), which employed the same technology, have suggested this solution which has proven to be reliable and the current developments, aimed at making the chips much faster than in ALICE, are promising in maintaining low occupancy, despite the worse expected background environment, and good radiation hardness even after irradiation.

In order to fulfill the physics requirements of Belle II experiment, a new silicon sensor is being designed, called OBELIX, exploiting the 180 nm TowerJazz Semiconductor process. Developments will ensure a faster, lighter and highly granular chip, reducing the material budget and improving tracks and vertices reconstruction.

OBELIX planning is based on studies done on previous prototypes, among which TJ-Monopix 2, whose characterization is the main topic of this thesis. Laboratory and beam tests have been conducted and are still in progress, in order to study the efficiency of the chip before and after irradiation, its power consumption, and to fully characterize its electrical characteristics. In particular, we have characterized the response of the pixel matrix, extracting important results that have allowed to interpret data taken during the Test Beam at Desy (July 2022), and that are being used in the design of the OBELIX chip. In more details, the threshold distributions for all the different types of front-end circuits implemented in the matrix have been studied, together with their dispersion and noise distributions. The calibration of the Time Over Threshold curves (which is a time width signal processing method used in this prototype) has been done by internal injection tests. The absolute calibration of the whole matrix has been achieved, employing a  $^{55}\text{Fe}$  radioactive source. Other radioactive sources have been used too, in order to check the trend of the ToT curves for charge values not accessible by internal injection. Additionally, different register settings have been examined in the interest of operating the matrix at low threshold, that is crucial to keep high efficiency even after irradiation. For this reason, several tests have been conducted to tune the threshold, in order to reduce the dispersion and make the threshold on the matrix as uniform as possible. During this investigation, a cross-talk issue has been discovered and therefore studied to understand its causes and possible solutions to mitigate this effect.

Chapter 1 briefly introduces some of the open questions in the Standard Model, in order to depict the background of the Belle II physics program. Then a short description of the SuperKEKB accelerator and Belle II detector is given, too.

Chapter 2 presents the fundamental reasons behind the choice of an upgrade. The primary sources of the experiment background are summarized, to understand the limitation of the detector and the accelerator, for increasingly higher luminosity values. Eventually a summary of the four main upgrade proposals for the vertex detector is presented, which are distinguished by the different type of sensors employed: Depleted Field Effect Transistor (DEPFET), Thin and Fine-Pitch SVD, Silicon On Insulator (SOI) and CMOS Monolithic Active Pixels Sensors.

Chapter 3 describes the principles underlying the operation of semiconductor detectors and some different type of sensors which use this technology, like the hybrid and monolithic pixel sensors. In particular the CMOS Monolithic Active Pixel Sensors technology is presented, on which the entire developments of the OBELIX chip is based. In the end, the history of the developments that led to the TJ-Monopix chip series is retraced, in order to better understand the main features of the last one, TJ-Monopix 2, which represents the starting point for OBELIX design, and whose characterization is the work of this thesis.

Chapter 4 examines in depth the VerTeX detector (VTX) upgrade program, which involves the CMOS Monolithic Active Pixel Sensors as fundamental components of the five layers of the final vertex detector. Studies and simulations are ongoing to test the performance, and some of them are shown here. The specifications and the implementation of the new chip (OBELIX) under design for this proposal are described. The innovative sensor has to fulfill the requirements of Belle II experiment, even in extreme environment due to higher doses of radiation and backgrounds.

Chapter 5 lastly shows the results obtained from laboratory measurements and tests conducted on the TJ-Monopix 2 chip. The response of the matrix has been studied in different working conditions, in order to analyze the behaviour at high and low threshold. The absolute calibration of the all front-end circuits implemented in the chip, has been done too. Moreover a cross-talk issue have been discovered and analyzed, in order to understand its causes and a possible mitigation of this effect since it prevented from using the matrix at low threshold.

# 1. Belle II and SuperKEKB (SKB) accelerator

The first chapter introduces some of the main unexplained aspects of the Standard Model (SM), on which the Belle II physics program is focused. A short description of the SuperKEKB accelerator and the Belle II detector's structure is also presented and in conclusion some highlights on the current state of measurements.

## 1.1 Physics program of the B-factories

The SM is a very successful theory describing three of the fundamental forces involving elementary particles: the strong, weak and electromagnetic interactions, with the exclusion of the gravitational force. It classifies all the elementary constituents of matter in 4 main groups, as shown in Figure 1.1: quarks and leptons, constituting the matter fields; the gauge bosons, representing the interactions; and the Higgs boson, whose non-zero vacuum expectation value is needed to give mass to the otherwise massless matter fields.



Figure 1.1: Particle classification in the Standard Model.

### 1.1.1 Open questions in SM

Despite the undeniable success of the SM in providing predictions for all known physics phenomena, which have been experimentally verified with high precision over the years, there are many fundamental aspects of nature on which it is unable to give answers [1]. Some of them are listed in the following.

- Three generations of quark and leptons have been discovered, but it is not known whether they are the only ones and why.
- The reasons behind quark and leptons mass hierarchy are unknown.
- Although the Higgs mechanism is able to explain the cause of elementary particles' masses through spontaneous electro-weak symmetry breaking, it is not clear whether neutrinos can get their non-zero but very small masses through the interaction with the Higgs boson.
- Another open question is the matter-antimatter asymmetry in the Universe. Charge-Parity (CP) violation is necessary to explain the asymmetry, but the SM mechanism would predict a value several orders of magnitude smaller than what is needed to explain the matter domination over antimatter, which allowed the evolution of the universe as we know it today.
- The flavour-changing currents are phenomenologically described with two mixing matrices: the Cabibbo-Kobayashi-Maskawa (CKM) matrix for the quarks and the Pontecorvo-Maki-Nakagawa-Sakata (PMNS) matrix for the neutrinos. The SM fails to provide any explanation neither for the structure of the matrices (only charged for the quarks, only neutral for the neutrinos), nor for the values of their elements (nearly diagonal for the quarks, highly non diagonal for the neutrinos).
- Astrophysical observations indicate the existence of dark matter, but its origin and nature have not been explained yet.

All these open questions stimulate the search for new particles and processes that could provide more fundamental explanations.

At the energy frontier, experiments at the Large Hadron Collider (LHC) at CERN (CH) are looking for new particles created from the proton-proton collision with a center mass energy up to 14 TeV.

At the luminosity frontier, instead, new particles and interactions are searched through precision measurements of suppressed reactions or deviations from SM. The discrepancies could be interpreted as a clue of new physics beyond SM. The Belle II experiment at the SuperKEKB is following this last approach .

In particular, the experiment investigates the CP violation in the B mesons system and searches for new physics evidence in the decays of B and D mesons, in  $\tau$  leptons and in the dark matter sector (DM).

### 1.1.2 Peculiarity of asymmetric B factories

The SuperKEKB  $e^+e^-$  collider operates with a center-of-mass energy of  $\sqrt{s} = 10.58$  GeV at the  $\Upsilon(4S)$  resonance, which decays almost instantaneously into a pair of B - anti B mesons in nearly 96% of cases.

In SuperKEKB the beam energies are different, leading to a center-of-mass boost in the laboratory that allows the reconstruction of the B-mesons decay vertices, their lifetimes, and the time-dependent decay rate asymmetries.

In a beams symmetric situation, the B-mesons would be produced almost at rest, decaying roughly at the same point with undetectable decay lenght. The investigation of CP violating processes instead, requires measuring the decay time difference of the two B mesons and its uncertainty is dominated by that of the decay vertex measurement (order of hundreds microns). Let us look at this in more details.

SuperKEKB collides an electrons beam of 7 GeV (High Energy Ring, HER) with a positrons beam of 4 GeV (Low Energy Ring, LER) with a Lorentz boost factor of the  $\Upsilon(4S)$  of  $(\beta\gamma)_{\Upsilon(4S)} \approx 0.28$ .

The same boost is also acquired by the B-mesons, because they are produced almost at rest ( $m_{\Upsilon(4S)} - m_{B_0} \approx 19$  MeV). Moreover knowing that  $\tau_B \simeq 1.5 \times 10^{-12}$  s and so  $c\tau_B \simeq 450 \mu\text{m}$ , we can compute the average flight distance travelled before decaying:

$$l = (\beta\gamma)_{\Upsilon(4S)} c\tau_B \approx 126 \mu\text{m} \quad (1.1)$$

This value must be within the vertex detector sensitivity in order to distinguish the vertex decay and as consequence to make precision measurements of lifetimes, mixing parameters and CP violation. The main task of the VerteX Detector (VXD) is to reconstruct the production and decay vertices of the particles originated from the beam collisions. This aspect is crucial to perform time-dependent measurements, core of the Belle II physics program. The six-layer VXD can determines the position of the vertices with a precision better than  $100 \mu\text{m}$ , allowing to reconstruct secondary vertices, i.e. the decay position of the particles coming from B decays, and also from  $\tau$  leptons and D mesons.

The event kinematics is illustrated in Figure 1.2. The two B mesons are produced in an entangled quantum state, so when from the decay products of one of the two it is possible to assign its flavor (for example  $B^0$ , identified as  $B_{tag}^0$ ) accordingly can be assigned that of the second, which will be the opposite ( $\bar{B}^0$ , called  $\bar{B}_{phys}^0$ ).

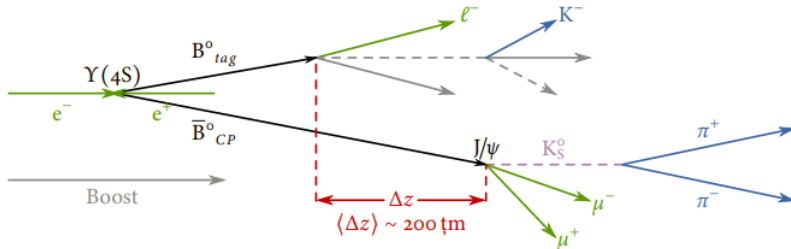


Figure 1.2: Example of the kinematics of the golden channel of Belle II experiment.

After this reconstruction, both B decay vertex positions in the longitudinal direction  $z_1$  and  $z_2$  are evaluated, in order to compute their difference:

$$\Delta z = z_1 - z_2 = (\beta\gamma)_{\Upsilon(4S)} c\Delta t \quad (1.2)$$

where  $\Delta t$  is the proper time decay difference. Therefore this topology allows to transform a temporal information in a spatial one that we are

able to measure using a high precision vertex detector. Without the boosted center of mass none of it could be possible, and this is an essential feature for an asymmetric B-factory.

## 1.2 SuperKEKB accelerator

Belle II sensitivity in the precision measurements is feasible especially thanks to the extraordinary performance of the SuperKEKB accelerator which host the (almost) hermetic detector. This complex facility is the result of efforts and efficient collaboration between the researches of KEK laboratory and all the international working groups that participate to the experiment.

### 1.2.1 The facility

SuperKEKB[2] (Figure 1.3) is an asymmetric  $e^+e^-$  collider with a circumference of 3 km and a center of mass energy peak equal to  $\sqrt{s} = 10.58$  GeV, which corresponds to the mass of the  $\Upsilon(4S)$  resonance. Compared to its predecessor KEKB (which started its operation in 1998 and concluded it in 2010), the current accelerator has allowed to obtain the highest luminosity ever achieved, equal to  $4.7 \times 10^{34} \text{ cm}^{-2}\text{s}^{-1}$  in July 2022. This target was possible using a new scheme to accelerate and collide the beams, the so called *nano-beam scheme* (section 1.2.2).

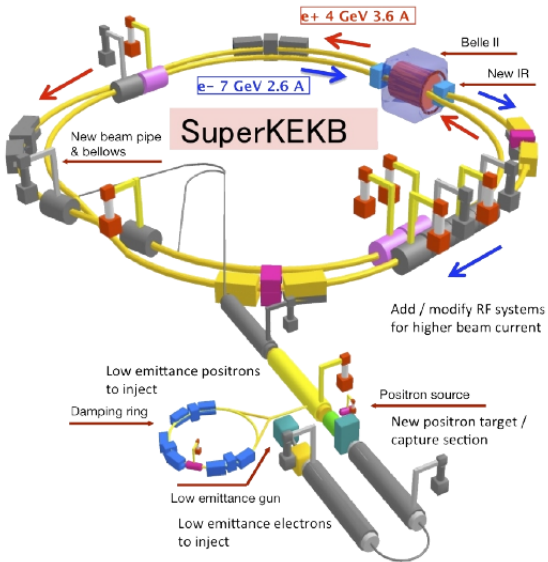


Figure 1.3: SuperKEKB accelerator structure.

### Luminosity

Instantaneous luminosity is one of the key parameters of any accelerator and it represents the interaction rate per unit of cross section between colliding particles. Inverting this equation is possible to obtain  $N$ , namely the number of the physical events produced in the interaction with a given luminosity:

$$L = \frac{1}{\sigma} \frac{dN}{dt} \quad \Rightarrow \quad N = \int_0^T L \sigma dt \quad (1.3)$$

where  $T$  is the duration of the experiment and  $\sigma$  the cross section of the physical process of interest. Luminosity is dependent from both machine and beam parameters. With respect to this, it can be expressed as:

$$L = \frac{N_- N_+}{2\pi \sqrt{\sigma_{x_-}^2 + \sigma_{x_+}^2} \sqrt{\sigma_{y_-}^2 + \sigma_{y_+}^2}} n_b f_{rev} R \quad (1.4)$$

where "±" denotes respectively positrons and electrons beam,  $\sigma_{x,y\pm}$  represent the horizontal and vertical beam size,  $N_{+,-}$  are the number of particles in a bunch,  $n_b$  the number of bunches,  $f_{rev}$  the revolution frequency, and  $R$  the geometrical loss factor. In the interaction region, where the beam-beam interaction becomes important, the following formula is commonly used:

$$L = \frac{\gamma_\pm}{2e r_e} \left(1 + \frac{\sigma_y^*}{\sigma_x^*}\right) \left(\frac{I_\pm \xi_{y\pm}}{\beta_y^*}\right) \left(\frac{R_L}{R_{\xi_{y\pm}}}\right) \quad (1.5)$$

where the starred parameters refer to their value at the Interaction Point (IP).  $I$  is the beam current,  $\beta_y^*$  the vertical beta function at the IP.  $\xi_{y\pm}$  is the vertical beam parameter which include the horizontal beta function at the IP, the horizontal emittance, the bunch length and the crossing angle between the beams.  $R_L$  and  $R_{\xi_{y\pm}}$  are the reduction factors due to geometrical loss such as the hourglass effect and finite crossing.

As already mentioned, SuperKEKB holds the current world record in luminosity (with  $\beta_y^* = 1.0$  mm) and in the future the target will be to reach  $6 \times 10^{35} \text{ cm}^{-2} \text{s}^{-1}$  (by the 2030s), by increasing currents beam and reducing their size at the IP, through the decrease of the betatron function down to  $\beta_y^* = 0.3$  mm. However, the increase in charge in the bunch, causes a reduction of the Touschek lifetime and the injection system is unable to compensate for the loss. This process makes also the beam-induced background increase significantly, risking deterioration and poor functioning of the detector. It has been estimated that the background should remain acceptable up to a luminosity value equal to  $2.8 \times 10^{35} \text{ cm}^{-2} \text{s}^{-1}$  with  $\beta_y^* = 0.6$  mm [3]. So the chance to achieve higher luminosity is closely related to an upgrade plan of both the whole detector and the accelerator.

### 1.2.2 "Nano-beam" scheme

We have seen that the *beta function*  $\beta$  at the IP ( $\beta^*$ ) is a decisive factor to define the luminosity. To be able to ramp the luminosity up, it is necessary to reduce the value of  $\beta$  depending also, but not only, on the variation of the other machine parameters that appear in the equation 1.5.

The mechanism used in SuperKEKB is called *nano-beam scheme*, and it allows to obtain luminosity 40 times greater than that of KEKB, managing to decrease the  $\beta^*$  by a factor 20 compared to KEKB [2].

This new scheme, originally designed by P. Raimondi[4], dictates that the beam bunches have to collide with sufficiently small  $\sigma_x^*$  and at large angle. In case of SuperKEKB the angle is equal to 83 mrad at the IP (larger with respect to the crossing angle used in KEKB) with the beam size of 50 nm in the vertical direction and 100  $\mu\text{m}$  in the horizontal direction (in Figure 1.4 a simplified representation of the differences).

This strategy also helps to reduce the *hourglass effect*, which happens when the  $\beta^*$  is comparable or smaller than the bunch length, causing a decrease in luminosity. With a large crossing angle, the overlap length, which is the effective bunch length, is much shorter than the bunch length along the beam axis.

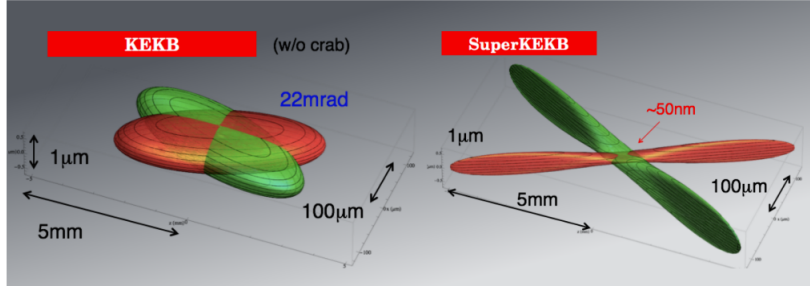


Figure 1.4: Comparison between the beam schemes used in KEKB and SuperKEKB.

Using a crossing angle large enough has other positive implications on the operation of the accelerator and its further improvements, like allowing the placement of a new focusing system at the IP (which may require more space), considering a future redesign of the interaction region.

## 1.3 Belle II detector

The Belle II detector is a general-purpose spectrometer which consists of a concentric subdetectors sequence placed around the berillium beam pipe of 10 mm radius, nearby the IP of the two beams. Here we will go through a brief description of the subdetectors (Figure 1.5) going in order from the beam pipe outwards: the Vertex Detector, the Central Drift Chamber, the TOP and the ARICH, the Electromagnetic Calorimeter and the  $K_L$  Muon detector.

In Table 1.1 a summary of the main characteristics of all subdetectors.

### 1.3.1 Vertex Detector (VXD)

The **VerteX Detector (VXD)** is composed by two devices divided into layers, the silicon Pixel Detector (PXD) and the Silicon Vertex Detector (SVD), for a total of six layers around the beam pipe.

The inner two layers of PXD (L12) consist of pixelated sensors based on the depleted field effect transistor (DEPFET) technology, realised with very thin ( $< 100 \mu\text{m}$ ) sensors which allows to minimise multiple scattering, thus improving the tracking resolution for low-momentum particles. They are at a radius of 14 mm and 22 mm, respectively.

The remaining four layers of SVD (L3456) instead, are equipped with double-sided silicon strip (DSSD) sensors (at 39 mm, 80 mm, 104 mm and 135 mm respectively). Since a lower background rate is expected with respect to PXD, DSSD allow to achieve similar performance with a much smaller number of readout channels. These layers are mainly used for tracking/vertexing and also for particle identification (PID), through the measurement of the energy loss ( $dE/dx$ ).

We can notice in Figure 1.6 that because of the essential asymmetric configuration of the beam energies and the consequent boost of the particles produced in the collisions (section 1.1.2), the

Table 1.1: Summary of the detector components[1].

Purpose	Name	Component	Configuration	Readout channels	$\theta$ coverage
Beam pipe	Beryllium		Cylindrical, inner radius 10 mm, $10 \mu\text{m}$ Au, 0.6 mm Be, 1 mm paraffin, 0.4 mm Be		
Tracking	PXD	Silicon Pixel (DEPFET)	Sensor size: $15 \times (L1 = 136,$ $L2 = 170) \text{ mm}^2$ , Pixel size: $50 \times (L1a = 50, L1b = 60, L2a$ $L2b = 85) \mu\text{m}^2$ ; two layers at radii: 14, 22 mm Rectangular and trapezoidal, strip pitch: $50(p)/160(n) -$ $75(p)/240(n) \mu\text{m}$ , with one floating intermediate strip; four layers at radii: 38, 80, 115, 140 mm	10M	[17°;150°]
	SVD	Silicon Strip		245k	[17°;150°]
	CDC	Drift Chamber with $\text{He-C}_2\text{H}_6$ gas	14336 wires in 56 layers, inner radius of 160mm outer radius of 1130 mm	14k	[17°;150°]
Particle ID	TOP	RICH with quartz radiator	16 segments in $\phi$ at $r \sim 120 \text{ cm}, 275 \text{ cm long, } 2 \text{ cm thick quartz bars with } 4 \times 4$ channel MCP PMTs	8k	[31°;128°]
	ARICH	RICH with aerogel radiator	$2 \times 2 \text{ cm}$ thick focusing radiators with different $n$ , HAPD photodetectors	78k	[14°;30°]
Calorimetry	ECL	CsI(Tl)	Barrel: $r = 125 - 162 \text{ cm, end-cap: } z = -102 - +196 \text{ cm}$	6624	(Barrel), [12.4°;31.4°], [32.2°;128.7°], [130.7°;155.1°]
Muon ID	KLM	barrel:RPCs and scintillator strips	2 layers with scintillator strips and 12 layers with 2 RPCs	16k, $\phi$ 16k	[40°;129°]
	KLM	end-cap: scintillator strips	12 layers of $(7\text{-}10) \times 40 \text{ mm}^2$ strips	17k	[25°;40°], [129°;155°]

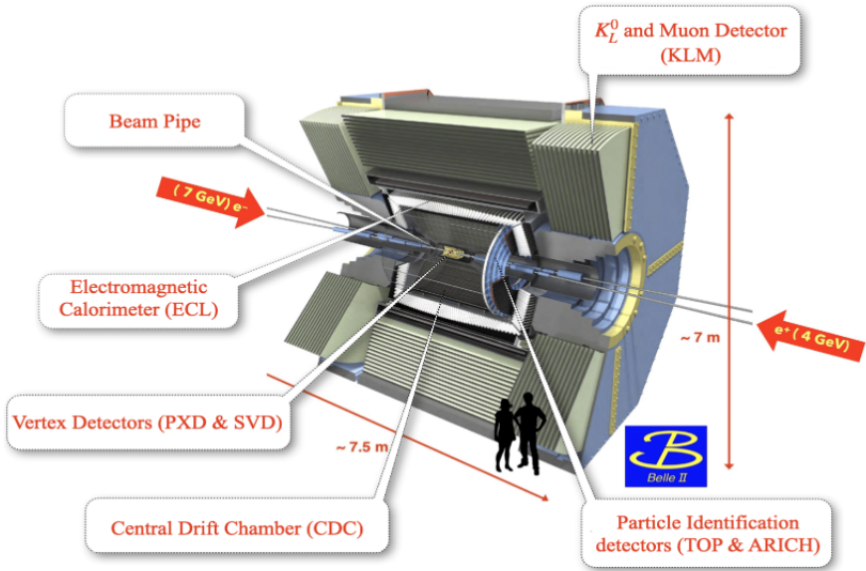


Figure 1.5: Belle II detector.

structure of the vertex detectors is also asymmetric along the longitudinal axis.

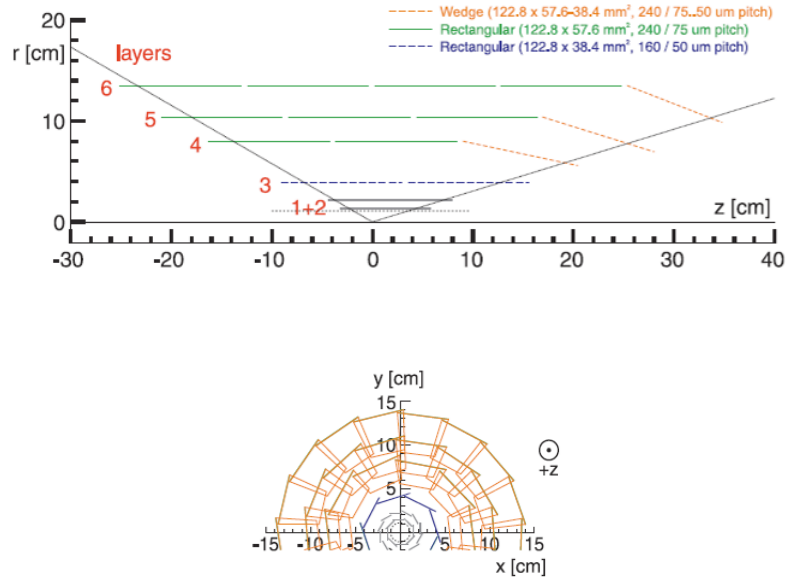


Figure 1.6: A schematic view of the Belle II vertex detector with a Be beam pipe and the six layers of PXD and SVD.

### 1.3.2 Central Drift Chamber (CDC)

This is the central tracking device, with a large-volume drift chamber and small drift cells. The chamber gas is composed of a He–C<sub>2</sub>H<sub>6</sub> (50:50) mixture with an average drift velocity of 3.3 cm  $\mu$ s<sup>-1</sup> and a maximum drift time of about 350 ns for a 17 mm cell size.

The CDC contains 14336 wires arranged in 56 layers either in *axial* (aligned with the solenoidal magnetic field) or *stereo* (skewed with respect to the axial wires) orientation (Figure 1.7). In fact by combining information from both the axial and the stereo layers it is possible to reconstruct full three-dimensional helix charged tracks and measure their momenta. It also provides information for PID by measuring ionization energy loss, which is particularly useful for low-momentum particles.

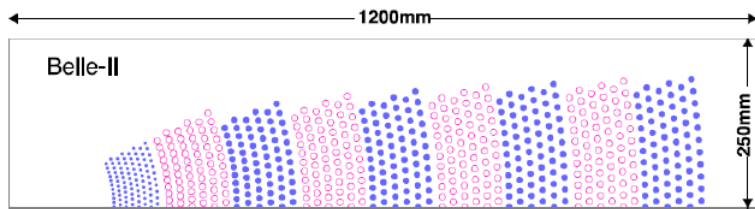


Figure 1.7: Schematic view of the CDC drift cells: blue dots represent the axial wires and the pink empty ones the stereo wires.

### 1.3.3 Particle identification system (TOP e ARICH)

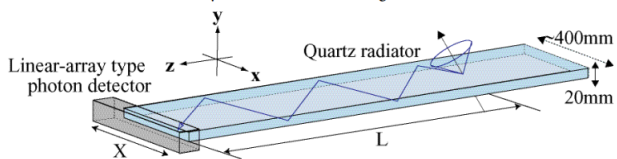
The **TOP** (**T**ime **O**f **P**ropagation) is a special kind of Cherenkov detector used for PID in the barrel region. It employs the two-dimensional information of a Cherenkov ring image, obtained from the time of arrival and the impact position of Cherenkov photons at the photodetector at one end of a 2.6 m quartz bar. It is composed by 16 detector modules, each one consisted in a 45 × 2 cm quartz bar (Cherenkov radiator) with a small expansion volume (about 10 cm long) at the sensor end of the bar (Figure 1.8).

In order to achieve a single-photon time resolution of about 100 ps (required for a good PID), 16-channel microchannel plate photomultiplier tubes (MCP-PMT) are employed, specially developed for this purpose.

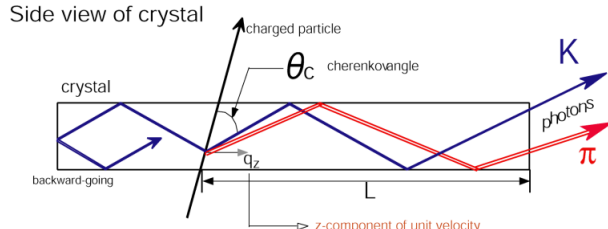
The **ARICH** (**A**erogel **R**ing **I**maging **C**herenkov) is used to identify charged particles and it is placed in the forward endcap region. It is a proximity focusing Cherenkov ring-imaging detector which adopts aerogel as Cherenkov radiator. In particular this detector employs a novel method to increase the number of detected Cherenkov photons: two 2 cm-thick layers of aerogel with different refractive indices ( $n_1 = 1.045$  upstream,  $n_2 = 1.055$  downstream) that increase the yield without degrading the Cherenkov angle resolution (Figure 1.9).

Hybrid avalanche photon detectors (HAPD) are exploited as single-photon-sensitive high-granularity sensors. Here photo-electrons are accelerated over a potential difference of about 8 KV and are detected in avalanches photodiodes (APD).

The main task of these detectors is to improve the K/ $\pi$  separation from about  $\approx 1$  GeV until 3.5 and 4 GeV/c of momentum, respectively.



(a) A schematic view of the TOP radiator.



(b) A side view of the TOP radiator.

Figure 1.8: TOP detector.

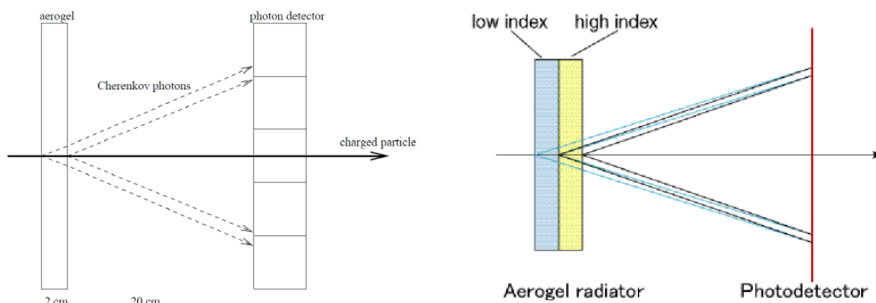


Figure 1.9: ARICH detector.

### 1.3.4 Electromagnetic calorimeter (ECL)

The **ECL** is a highly segmented array of tellurium-doped caesium iodide CsI(Tl) crystals assembled in a 3 m long barrel section with a radius of 1.25m, and two endcaps discs located at 2 m (forward) and 1 m (backward). All of them are instrumented with a total of 8736 crystal, covering about 90% of the solid angle in center-of-mass system.

This detector is used to detect gamma rays and to identify electrons in order to separate the latter from hadrons, especially pions.

### 1.3.5 $K_L$ muon detector (KLM)

It consists of an alternating sandwich of 4.7 cm-thick iron plates and active detector elements located outside the volume of the superconducting solenoid that provides a 1.5 T magnetic field. The iron plates serve as the magnetic flux return joke for the solenoid. They also provide 3.9 interaction lengths or more of material, beyond the 0.8 interaction lengths of the calorimeter in which  $K_L^0$  mesons can shower hadronically. The active detector elements have been chosen in order to cope with the reduction of the detector efficiency under the SuperKEKB background

rates: resistive plate chambers (RPCs) for the outermost active layers and in the two innermost layers of the barrel and endcaps regions, scintillator strips with wavelength-shifting fibers are used, readout by silicon photomultipliers (SiPMs).

### 1.3.6 Trigger system

The trigger system of Belle II has a non-trivial role to identify events of interest during data-taking at SuperKEKB, where high background rates are expected. This system is divided into two levels: a hardware-based low-level trigger (L1) and a software-based high-level trigger (HLT), implemented in the data acquisition (DAQ) system.

- **L1**: based mainly on fast track reconstruction in the CDC and on ECL energy, has a latency of  $5\ \mu s$  and a maximum trigger output rate of 30 kHz, limited by the read-in rate of the DAQ.
- **HLT**: is a key component of the DAQ, used to fully reconstruct events that pass the L1 trigger selection. It has to reduce online event rates to 10 kHz for offline storage and it must identify track regions of interest for PXD readout in order to reduce data flux. It fully recreates events with offline reconstruction algorithms, using all detectors information except for the PXD.

## 1.4 Current state of data taking

SuperKEKB accelerator reached a peak luminosity of  $4.7 \times 10^{34} \text{ cm}^{-2}\text{s}^{-1}$  and Belle II accumulated almost  $428 \text{ fb}^{-1}$  before the beginning of Long Shutdown 1 (LS1) in July 2022. (Figure 1.10).

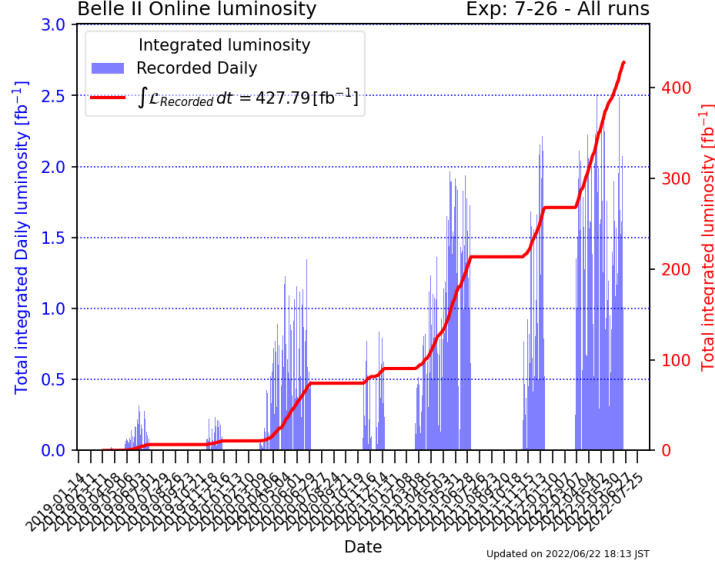


Figure 1.10: Total recorded integrated luminosity before Long Shutdown 1.

The target of SuperKEKB is to achieve a  $L_{inst} = 6 \times 10^{35} \text{ cm}^{-2}\text{s}^{-1}$  and to increase the integrated luminosity from  $428 \text{ fb}^{-1}$  (current value, starting in 2019) to  $50 \text{ ab}^{-1}$  (as shown in

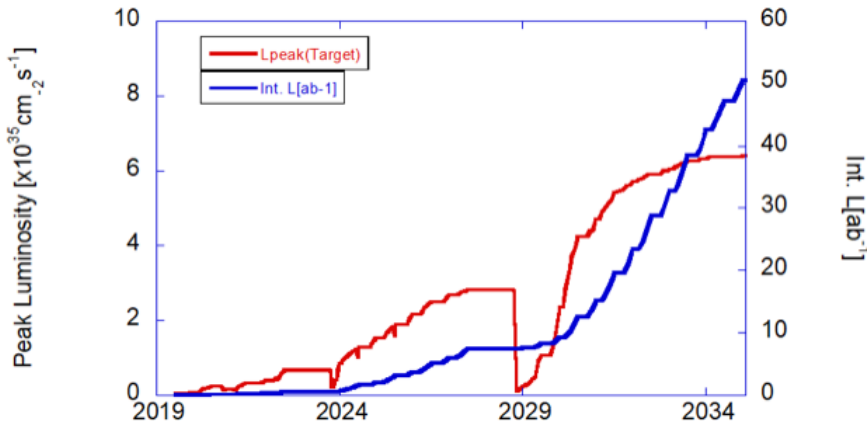


Figure 1.11: Luminosity projection plot (plan for the coming years).

the projection plot in Figure 1.11).

A three-phase program has been drawn up[5]:

- **short term:** year 2023. Long Shutdown 1 (LS1) started in July 2022, and will be concluded at the end of 2023. The main purpose of the shutdown was the installation of a complete PXD, since in the 2019 installation only two ladders were included in layer 2. In addition, significant maintenance and improvement work has been carried out both for Belle II and SuperKEKB.
- **medium term:** approximately year 2028-29. Long Shutdown 2 (LS2) will probably be needed for the upgrade of the Interaction Region (IR) to reach a new luminosity target  $L_{peak} = 6 \times 10^{35} \text{ cm}^{-2} \text{s}^{-1}$ . Several open questions and difficulties have triggered many studies and discussions about a possible redesign of the machine lattice during this phase. In particular it would be necessary to deal with the limitation of the optics of the machine, concerning the further increasing of the luminosity and accordingly of the backgrounds rates. A new Vertex Detector might be also required, to accommodate the new IR design, and other sub-detector upgrades are possible.
- **long term:** years > 2032. Studies have started to explore upgrades beyond the currently planned program, such as beam polarization and ultra-high luminosity and so possibly  $L_{peak}$  in excess of  $1 \times 10^{36} \text{ cm}^{-2} \text{s}^{-1}$ . While the beam polarization has a concrete proposal, for ultra-high luminosity studies have just started.

At time of writing we are in the period of a long shut-down (LS1), last since June 2022 and the installation of a complete pixel detector (PXD) is almost done. The restart of data taking is planned at the beginning of 2024.

## 2. Belle II Upgrade

This second chapter wants to address some of the main reasons in favor of the upgrade of Belle II. We will give an overview of the primary background sources in the experiment to understand how to mitigate them in order to achieve a better performance of the whole detector, even ramping up the luminosity. Eventually we will also introduce some of the proposals made for the enhancement of the vertex detector.

### 2.1 Purposes of the upgrade

Machine background play an important role in the safety, efficiency, and performance of data taking. Current studies foresee that SuperKEKB may reach higher luminosity targets with the existing accelerator complex, but in order to achieve the established final value of  $6 \times 10^{35} \text{ cm}^{-2} \text{s}^{-1}$ , an enhancement of the interaction region are under consideration.

As already mentioned, to reach a luminosity target of  $50 \text{ ab}^{-1}$ , two long shutdown have been decided: LS1 in 2022 to install a complete VXD, and LS2 in 2028 or later for the upgrade of the interaction region and the accelerator components. LS2 offers the opportunity for a significant detector upgrade, improving robustness against backgrounds and physics performance.

Belle II detector is also designed to operate efficiently under the high levels of backgrounds extrapolated to luminosity target, but safety margins are not so large. Moreover in the case of a redesign of the interaction region large uncertainties in the background extrapolations are unavoidable.

Therefore the global upgrade program is justified by many considerations, among them:

- improve detector's resistance to higher levels of background;
- make each subdetectors long-lived against radiation damage;
- push forward safety margins for running at higher luminosity;
- develop the technology to cope with different future paths;
- improve overall physics performance.

### 2.2 Background sources and limitations in Belle II

SuperKEKB is already the world's highest-luminosity collider and it aims to reach a new peak in the near future and also to increase the collected statistics, to become more sensitive to rare processes and precise measurements of Belle II physics program. But to be able to do this

without loosing the good functionality of the entire detector, it is necessary to understand how to reduce the beam background where possible and how to cope with the consequent challenges.

Several simulations and measurements of beam background are still being done in order to guess possible future machine scenarios, under new luminosity conditions. This is necessary to study the vulnerability of the subdetectors (and more generally of the machine) and so to design the countermeasures to adopt against the deterioration of performance and materials.

### 2.2.1 Main background sources

In the following some of the primary *single-beam* and *luminosity-dependent* background sources are discussed.

**Touschek effect** : It is an intra-bunches scattering process, where the Coulomb scattering of two particles in the same beam bunch causes a variation of their energies, increasing the value of one of them and lowering that of the other from the nominal value. This interaction among the bunch particles is the first beam background source at SuperKEKB.

**Beam-gas scattering** : this represents the collision of beam particles with residual gas molecules in the beam pipe. It is the second beam background source and it can occur via two processes: *Coulomb interaction*, which changes the direction of the beam particles and *bremsstrahlung scattering*, which instead decreases their energy.

In these two processes, the scattered particles fall out the stable orbit and hit the beam pipe while they move around the ring. This mechanism causes electromagnetic showers that can reach the detector if their origin (loss position) is near the interaction region. Collimators are in place to reduce these backgrounds by absorbing the off-orbit particles. These backgrounds are present even if the beams are not colliding and are therefore called *single-beam* backgrounds.

**Radiative Bhabha scattering** : It is the electron-positron scattering process  $e^+e^- \rightarrow e^+e^-\gamma$ , an undesirable collision processes at the IP which have very high cross sections but only little interest for the physics studied in the experiment. The emitted photon can interact with the magnets near the detector producing a large amounts of neutrons via the photo-nuclear resonance mechanism (such neutrons are the main background source for the outermost Belle II detector).

**Two-photon process** : it consists in the process  $e^+e^- \rightarrow e^+e^-e^+e^-$ . The produced electron-positron pairs can spiral around the solenoid field lines and leave multiple hits in the inner layers of the detector.

These backgrounds are called *Luminosity backgrounds* because their strength is proportional to the luminosity. They can be reduced with a careful design of the interaction region including neutron shielding.

**Synchrotron Radiation (SR)** : X-rays emitted from the beam when electrons and positrons pass through the strong magnetic field near the IP. The HER beam is the main source of this type of background, because SR power is proportional to the square of beam energy and magnetic field. SR can potentially damage the inner layers of the vertex detector due to an higher radiation dose in that region. Absorbing structures have been implemented inside the beam pipe to protect the detector from SR.

The rate of these processes is relatively high for small beams and high currents, leading to a beam lifetime in the order of only few minutes. This requires a continuous injection mechanism, in which particles are added to individual bunches to keep the charge constant. While this is essential for high luminosity operation, it is also the source of an additional background, since the perturbed bunches are noisy for a number of turns. The injection background is particularly hard to model and estimate.

### 2.2.2 Current background status and future predictions

Several monitoring devices are located all along the accelerator to measure radiation doses on both detector and delicate regions of the ring, in such a way to intervene as soon as possible in case too high levels are reached.

Dedicated beam background studies have been performed and for example, in Figure 2.1 are shown rates measured in June 2021 with a betatron function at the IP of  $\beta_y^* = 1$  mm and a collision luminosity of  $L = 2.6 \times 10^{34} \text{ cm}^{-2}\text{s}^{-1}$ . Current background rates in Belle II are acceptable and in most cases, well below the limits listed in table Table 2.1.

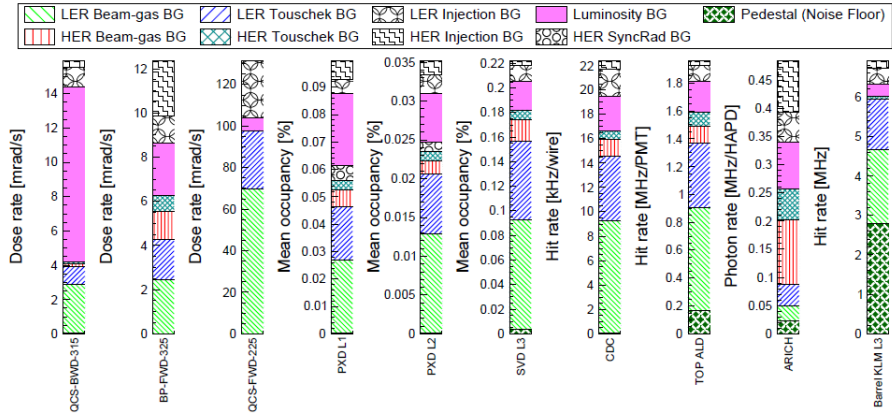


Figure 2.1: Measured Belle II background in June 2021. Each column shows different background sources for Belle II sub-detectors and also for superconducting quadrupole magnet (backward and forward) and the beam pipe.

Event though the current level is of no concern in terms of occupancy for the innermost layers of the vertex detector, a larger amount of localized SR, for example, could cause inhomogeneities in PXD modules, which would be very difficult to compensate by adjusting the operation voltages of the affected ones.

Until now it can be said that SuperKEKB and Belle II are operating stably. Beam-induced background rates are well below the limits of the detector and do not prevent from increasing further the current and hence the luminosity, as demonstrated by the predictions for the background rates *before LS2* with a known machine configuration. For what concern the predictions at  $L_{inst} = 3 \times 10^{35} \text{ cm}^{-2}\text{s}^{-1}$  instead, called *after LS2* operation, there are several uncertainties tied to the machine configuration. In fact at the moment, the *working machine lattice* to reach the target luminosity is not known and in addition the final design of the IR and beam pipes is not concluded yet.

Detector	BG rate limit	Measured BG
Diamonds	1 rad/s to 2 rad/s	< 132 mrad/s
PXD	3 %	0.1 %
SVD L3, L4, L5, L6	4.7 %, 2.4 %, 1.8 %, 1.2 %	< 0.22 %
CDC	200 kHz/wire	22.3 kHz/wire
ARICH	10 MHz/HAPD	0.5 MHz/HAPD
Barrel KLM L3	50 MHz non-luminosity BG	4 MHz
Before LS1		After LS1
TOP ALD		3 MHz/PMT + luminosity BG
		5 MHz/PMT
		1.8 MHz/PMT

Table 2.1: Background rate limits for Belle II detector sub-systems. The third column shows the total measured background rate in June 2021

Therefore an alternative solution is employed to roughly estimated the background rates. The background predicted Before LS2 phase is considered as a starting point and then different scaling factors are applied for single-beam background component, considering three different possible scenarios:

- **x2 - optimistic Scenario-1(v1)**
- **x5 - nominal Scenario-2(v2)**
- **x10 - conservative Scenario-3(v3)**, an arbitrary factor assuming that all single-beam backgrounds will be increased by a order of magnitude After LS2.

The luminosity background sources are instead scaled with luminosity ratio. These are then used to simulate the behaviour of the whole detector in future perspectives, as we will see in the following.

## 2.3 Summary of possible VXD upgrade

The Vertex Detector is particularly sensitive to machine background because it is the closest to the beam pipe and therefore subject to high doses of radiation. As we have already seen, current studies are trying to extrapolate how it could be affected by reaching the future luminosity target, but there are a lot of uncertainties due to models and still not well defined design of the interaction region. Moreover a completely new detector might be required, in the event of a considerable redesign of the IR. However in this case, also the physics performance could be improved, taking advantage of the more recent technology developments.

In particular all different upgrade ideas of the whole Belle II detector intend to ensure its proper functioning at the higher level of luminosity, condering also further improvements of the lattice machine and so of the colliding beams. The current detector configuration is not expected to maintain its performance level when facing higher beam background level or higher rates.

Concerning the Vertex Detector, all proposed improvements aim to:

- reduce occupancy level by employing fully pixelated and fast detector (CMOS technology has been chosen);

- increase robustness against tracking efficiency and resolution losses from beam background;
- improve radiation hardness to reduce detector ageing effects and performance degradation;
- reduce the inserted material budget between subdetectors in order to achieve good resolution by lessening the multiple scattering, especially important at lower momenta.

In the following we will present in a few words the four main proposals for future upgrade: Depleted Field Effect Transistor (DEPFET) pixel, thin strip sensor, CMOS Monolithic Active Pixel Sensor and SOI technology. The first two are more conservative and try to exploit as much as possible of the existing detector, making some appropriate adjustments to the sensor type, readout or mechanical structure. The last ones instead, plan to build an entirely new detector.

The reference background levels determining radiation robustness requirements of the innermost layers are the following:

- Hit rate capability:  $120 \text{ MHz}/\text{cm}^2$ ;
- Total Ionizing Dose:  $10 \text{ Mrad}/\text{year}$ ;
- NIEL fluence:  $5 \times 10^{13} n_{eq}/\text{cm}^2/\text{year}$ .

At this time, the main effort is focused in the development of the CMOS MAPS system, with the SOI as a possible backup option, although still requiring significant R&D. The DEPFET and thin strip sensors are substantially abandoned, but we present the, here to provide the full picture.

### 2.3.1 Depleted Field Effect Transistor (DEPFET)

This first proposal intend to minimize risks and costs of the project, preserving the general layout of the PXD system. The upgrade consists to improve the sensor to provide higher safety factor for the allowed occupancy and to prevent some issues that at the moment weaken the good functionality of the detector.

Some of the main improvements are listed below:

- improve signal transmission on the pixel matrix and the signal processing in the read-out, in order to reduce the read-out time per row from the current 100 ns to 50 ns. In this way the frame time and the background occupancy might be reduced by factor 2, while leaving unchanged the optimized size and number of PXD pixels as it stands;
- increase the robustness against beam losses which could make inefficient or even inoperative gate lines on almost all PXD modules. This reaction seems to be due to a high photocurrent on the chip because of the high instantaneous dose. It could be mitigated by adding protection circuits on-chip;
- Total Ionizing Dose (TID) effect on the chip provokes an unexpected avalanche current that does not compromise the sensor performance but requires more power supply to provide enough current. This issue might be solved by bringing some changes in the DEPFET pixel layout.

The DEPFET improvement R&D is currently inactive because of lack of person power and dedicated funding.

### 2.3.2 Thin and Fine-Pitch SVD

The Thin and Fine-Pitch SVD (**TFP-SVD**) is a new detector concept that aims to improve not only SVD, but potentially also the inner part of the CDC, whose functionality could be threatened by future beam background condition. This proposal uses Double-sided Silicon Strip Detectors (DSSDs) for the inner and middle detector volume since a single sensor can cover a large dimension. In the current detector the DSSD technology is already used in the SVD.

The major improvement of this proposal would be the reduction of the material budget. Currently SVD has about  $0.7\%X_0$  material budget per layer. TFP-SVD instead, decreasing the sensor thickness to  $140\ \mu\text{m}$ , intends to reduce it to  $0.41\%X_0$ .

Moreover, a reduced sensor thickness is expected to reduce the voltage needed to reach the full depletion, even after radiation damage. The front-end developed for TFP-SVD, the SNAP128 chip, has 128 input channels with a 127 MHz clock binary hit information sampled. It also offers a reduction of the amount of cables.

Some concerns about TFP-SVD are the feasibility and efficiency of the final sensor production and the small signal charge due to the short path length of the particles through the sensor.

A first prototype has been produced by Micron-Semiconductor Ltd (UK), with a size of  $52.6 \times 59.0\ mm^2$ . The characterization studies are in agreement with the expectation and also a lower full depletion voltage is confirmed.

The development of the TFP-SVD option has been abandoned because of the small signal to noise ratio (10 or less) and difficulties in the chip design optimization.

### 2.3.3 CMOS Monolithic Active Pixels Sensor

The VTX proposal, that we will analyze in more details in the next chapter, aims to replace the entire current VXD detector using Monolithic Active Pixel Sensors (MAPS) based on CMOS (Complementary Metal-Oxide Semiconductor) technology.

In CMOS MAPS the basic commercial CMOS technology is minimally modified to allow the collection of the charge released by a charged particle traversing the epitaxial layer where the readout electronics is fabricated. There are many technological variants sharing this same concept.

The Belle II chip is called OBELIX (Optimized BELLe II pIXel sensor), based on the pixel matrix of the TJ-Monopix2 chip, whose characterization is the main topic of this work (Chapter 5) and is developed with the technology of the TowerJazz company with a minimum feature size of 180 nm. The size of the sensor is expected to be  $3 \times 1.9\ cm^2$  with a pixel pitch between  $30\ \mu\text{m}$  and  $40\ \mu\text{m}$ , achieving a spatial resolution below  $15\ \mu\text{m}$ , required by the VTX upgrade program. The timestamp clock signal have to reach down to 25 ns, in order to deal with the target hit rate of  $120\ \text{MHz}/cm^2$ . All these characteristics allow to obtain a sensor with high granularity in time and space.

The VTX detector consists in 5 concentric layers of monolithic sensors with a barrel geometry. The global target thickness for the air-cooled two inner layers and for the water-cooled three outer layers, is expected to be of about  $2\% X_0$ .

The VTX solution intends to reduce the current PXD integration time by at least two orders of magnitude introducing other improvements:

- lower detector occupancy which allows to cope with higher background and to mitigate data-transmission bottlenecks.
- Better tracking efficiency and improved momentum resolution and impact parameter resolution at low transverse momentum.

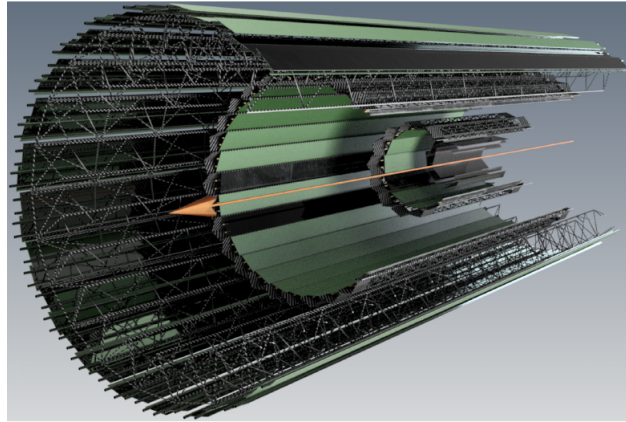


Figure 2.2: Overall VTX layout.

- Smaller data cables cross sections and less complex cooling system which might lighten the needed services.
- Simplified control and power systems due to the employment of a single sensor chip for all layers.

At the current state of art intense R&D is being carried out, taking advantage from other experiments experiences like ALICE, with the same type of sensor.

After this briefly review of the main upgrade proposals, we can now elaborate the VTX program in the following chapter.

### 2.3.4 Silicon On Insulator (SOI)

An alternative proposal employs a new pixel design, called Dual Timer Pixel (DuTiP), based on SOI technology. In Silicon-On-Insulator (SOI) technology, electronics is fabricated in a silicon layer separated by a  $SiO_2$  isolation layer from the main detector substrate. This new sensor concept has been developed to fulfill the requirements of a new vertex detector with faster readout, lower occupancy, smaller data size and smaller data transfer. In particular, it aims to store at least two hits during Belle II trigger latency ( $5\ \mu s$ ), to avoid loss information in higher background environment.

The size of the new designed pixel is  $45\ \mu m$  and the sensor layer thickness of  $50\ \mu m$ , which gives an intrinsic resolution better than  $15\ \mu m$ . The analog part is quite standard for a binary detector and consists of a sequence of preamplifier, shaper and comparator. ALPIDE was chosen as analog circuit with some modification to adapt it to SOI technology. The quite complex digital circuit has to be assembled on each pixel, and Lapis semiconductor  $2.0\ \mu m$  FD-SOI CMOS technology has been chosen, based on the experience gained in the successful development of other detectors like the pixel detector for the future ILC (SOFIST).

DuTiP pixel detector is designed to cover the current VXD acceptance with 7 layers. For the inner layer of the detector might be possible the cooling with airflow at room temperature; for the outer layers instead, a combination of air and water flows.

The DuTiP R&D are ongoing and the chip prototypes seems to work fine, in agreement with the expectation.

## 3. CMOS MAPS sensors

The fourth chapter aims to introduce the essential features of the semiconductor detector technology, going through the history of its advancements, which have led to the currently most promising sensors based on CMOS logic structure, the Monolithic Active Pixel Sensors (MAPS). The VTX program wants to make the most of the technologies that have already proven reliable in precision measurements, ensuring fast readout and high radiation tolerance, like the TJ-Monopix development line. We will briefly present it, mentioning the peculiarities of its prototypes, to better understand how they could fulfill the Belle II requirements.

### 3.1 Semiconductor detectors

The detection of elementary particles, nuclei and radiations occurs through their interaction with matter. In particular, charged particles are often detected by atom ionization or excitation of the sensitive detector layers along their path passing through. This detection method can be used in gases, liquids and semiconductors. We want to focus on detectors that use semiconductors as sensitive material.

All solids can be divided into three categories based on their electrical conductivity: conductors, semiconductors and insulators. In a solid state lattice, the constituent atoms have a dense periodic arrangement and the energy levels of some level groups lie energetically so dense (order of meV) that one speaks of *energy bands*, separated from each other by a *band gap*, which represents the distance in energy between them ( $E_G$ , energy gap). The electrical conduction properties of materials are determined by the two highest energy bands, which are the **valence band (VB)** and the **conduction band (CB)**. The energy levels within the same band are so close that the transitions to unoccupied levels, if they are not completely filled, are easily possible. Therefore the electrical conduction properties depend on the band gap between the two levels and on the band occupation, as we can see in Figure 3.1.

In insulators the valence band electrons are strongly bonded to neighbouring atoms, they are not free and they do not contribute to the conduction. In fact the VB is entirely occupied, the CB instead, is empty. As a consequence of the strong interatomic bond, there are large energy gaps between the VB and the CB (typically  $E_G$  of about 9 GeV). Thus current flow is practically impossible.

In semiconductors weaker bonds between neighbouring atoms result in a smaller energy gap with respect to the insulator (for example 1.12 eV in silicon). In this way electrons from VB can easily overcome the gap, moving on the CB by thermal excitations or by external electric fields. When an electron makes this transition, it leaves a hole in the VB, which could be filled in turn, by another electrons of the VB. Applying an external electric field, the free electrons in the CB and the holes in the VB start to move producing two different current flows, one negative and

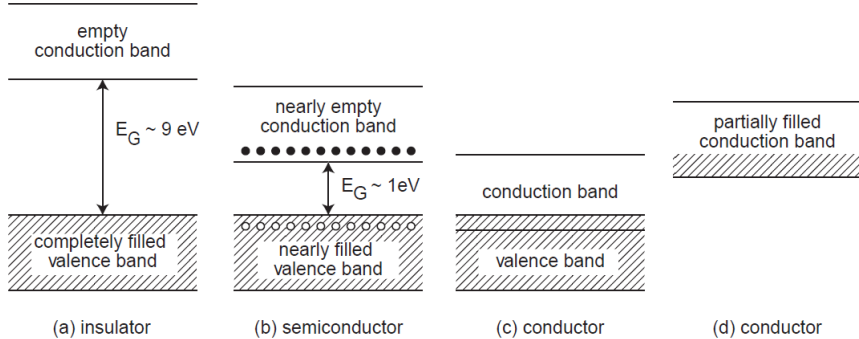


Figure 3.1: Schematic structure of the energy bands in insulators (a), semiconductors (b) and conductors (c,d).

the other positive, respectively.

In conductors, either the conduction and valence bands overlap or the conduction band is partially filled, so transitions within the same band and between the two different bands are easy and current conduction requires minimal energy.

### 3.1.1 Movement of charge carriers and signal formation in semiconductors

Semiconductor materials are the only ones that allow the detection of charged particles by ionization of the sensitive matter (in conductors a current is always present, not only in case of particle or radiation crossing).

When a charged particle or a photon pass through the medium, they release a certain amount of energy mainly by ionization, atom excitation and bremsstrahlung radiation the first, absorption by semiconductor the second. Most part of this energy loss, in turn, causes the formation of positive and negative charges, which in this context, are defined charge carriers (the rest is absorbed by the lattice). In semiconductors these carriers are the hole electron pairs created by ionization, which start to move in opposite direction due to an external electric field: the holes (positive) migrate towards the **catode** and the electrons (negative) towards the **anode**, which sense the signal induced by this movement. In fact, their drift induces an accumulation of charges on the electrode surfaces, and it is possible to record this charge induction as a charge, current or voltage signal. It is worth to notice that the generation of the signal depends on the movement of the carriers relative to the electrodes, and not when they actually arrive, that is the moment in which the signal stops.

The charge carrier density of semiconductors can be modified by doping the material with specific chemical elements, and this process causes a modification of their conduction properties. Undoped semiconductors are called *intrinsic semiconductors*.

*Extrinsic semiconductors* instead, are artificially doped with external impurities like:

- Pentavalent elements (P, As, Sb), called *donors*, added in a tetravalent material (Si, Ge) produce an excess of conduction electrons with respect to the holes (n doping, Figure 3.2 (a)).

- Trivalent atoms (B, Al, Ga), called *acceptors*, create an excess of holes (p doping, Figure 3.2 (b)).

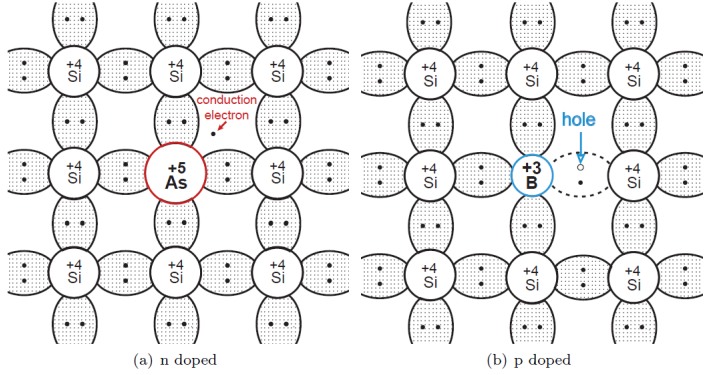


Figure 3.2: Schematic representation of atom bonding structure in n-doped and p-doped semiconductors.

### 3.1.2 The pn junctions as detector

The base material employed in semiconductor detectors is silicon, because it is stable, abundant and it has a low band gap which allows to produce an adequate amount of charge to be detected. When a p-doped semiconductor get in contact with a n-doped material, a *pn junction* is formed. In particular, the p-doped part is the one where holes are the dominant charge carriers, called **majority carriers**; in the n-doped part of the crystal instead, the majority carriers are the electrons. The presence of these excesses of opposite charge in the two parts of the junction, generates a potential difference across the junction, which causes a migration of the majority carriers from each part to the opposite one. At the boundary the charges recombine (when a conduction band electron occupies a valence band hole, losing energy), and this process creates a zone which is free of charge carriers, called **depletion zone**. After the recombination, the atoms of this depletion region are ionized, and so it is no longer neutral, but features a *space-charge*(Figure 3.3): a positive one in the n-layer, and negative in the p-layer. Moreover these space charge densities are opposite in sign, so they generate an intrinsic electric field that stops the original diffusion.

Moreover, the application of an external voltage  $V_{ext}$  between the two sections of the junction, provokes a variation of the width of the depletion region, depending on the size and polarity of the applied voltage. It is possible to distinguish:

- *forward bias*,  $V_{ext} > 0$ : a positive external voltage applied to the p side with respect to the n side, causes a reduction of the depletion region;
  - *reverse bias*,  $V_{ext} < 0$ : if a negative voltage at the p side or positive at the n side relative to the respectively opposite side is applied, the depletion region gets wider.

Depleted region is a zone without free charge carriers (do not come from the signal), and with the presence of an external electric field (reverse bias), it is a fundamental for semiconductor detectors.

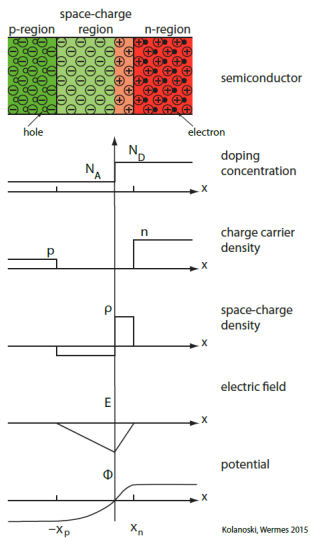


Figure 3.3: Doping concentration, charge carrier and space charge densities, electric field strength and electric potential in a p-junction.

The performance of the junction as a detector is determined above all, by the boundary properties between p-and n- doped silicon. Boundaries of the same doping type, but with different concentration, also create a similar pn structure, like for example  $n^{++}n$  or  $p^{++}p$ . There are also Metal-semiconductor boundaries, used in metal contact with the outside and Metal-Oxide-Semiconductor interfaces (MOS) that we will see in more details in the following.

### 3.1.3 Metal-Oxide-Semiconductor (MOS)

A MOS structure is a double interface made of three different media: an insulator (oxide) placed between the metal and the semiconductor, as shown in Figure 3.4.

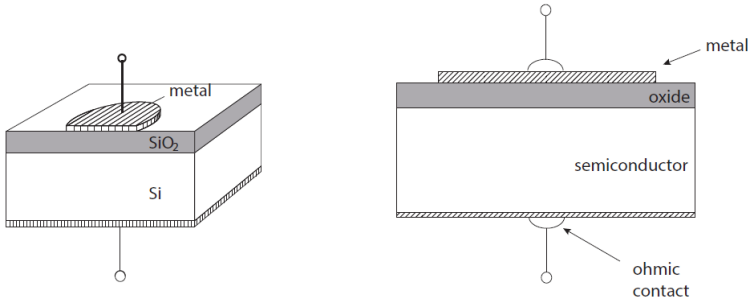


Figure 3.4: A perspective (on the left) and a cross-sectional illustration (on the right) of a MOS structure.

In recent transistor technology, the metal is almost entirely replaced by highly doped polysilicon, like  $n^{++}$  and  $p^{++}$  since these materials are more resistant to high temperature. Despite this, the physics remains essentially the same. The MOS structure plays a very important role in

chip electronics, including the readout of detectors, which employ a combination of NMOS and PMOS transistors, embedded in the substrate. This is at the base of the *Complementary* MOS (CMOS) electronics, which allows to develop more complex circuits. This technique consists in accomodate one of the two transistor type in a differently doped area, called *well*. For example, in a p-type substrate, a PMOS transistor are accomodate in n-wells, and vice versa with a n-type substrate.

## 3.2 Hybrid and monolithic pixel sensors

Nowadays the most important sensors used as tracking detectors are the semiconductor detectors, especially at high rates and high radiation levels. We have already seen that the particle passing through semiconductors, releases energy producing electron-hole pairs in the depletion region, which in turn, are separated by an external electric field. Moreover, the signal produced depends on the number of pairs generated, the carriers velocity drifting towards the electrodes, and the electrode geometry. In particular, the drift velocity depends on the charge carriers mobility, which is a function of the electric field, and on the electric field applied (Drude model):

$$v_D = \mu(E)E \quad (3.1)$$

At high electric field values, the mobility starts to saturate. Spatially sensitive semiconductor detectors, like microstrip or pixel detector, are usually very thin (200 - 300  $\mu\text{m}$ ) with typical velocities of about 50  $\mu\text{m}/\text{ns}$ . So the time needed to pass through the space charge region is of  $\approx 4\text{-}6 \text{ ns}$ .

There are several type of semiconductor detectors which are distinguished from their geometry, their micro-structure, their arrangement and other features. We want to see in more details, two among them: *hybrid* and *monolithic* pixel sensors, where the sensor and the readout could be separate entities or integrated in the same silicon crystal, respectively.

### 3.2.1 Hybrid pixel detector

Differently from *monolithic* sensors, *Hybrid* pixel detectors are composed by two different parts: a silicon layer structured in pixel cells, which represents the pixel sensor, and the readout chips with the same cell pattern, that process, digitize, store and transmit the hit data. At each pixel, they are connected by a conducting microconnection (called *bump bond*). In Figure 3.5 is shown an example of a detector module.

When a particle crosses the sensor, a signal is generated on the electrodes due to the drift of the charge carriers in the depleted region. This signal passes through the conductive bump in the readout chip, where it is amplified and discriminated.

One of the advantage of the pixel detectors with respect to the strip sensors, is the higher tolerance to radiation damage. The *leakage current* increases as the radiation doses become higher, it depends on the volume of the sensors and it is distributed over all the electrode. In pixel detectors this current is shared among more electrodes with respect to the strip detectors, so the leakage current per electrode is smaller. Moreover, as separate entities, sensor and readout could be independently optimize.

Among the disadvantages instead, there are the cost and complexity of the implementation processes, but also large material thickness together with the necessity to add support and cooling structures, which worsen the track reconstruction and momentum resolution because of the multiple scattering.

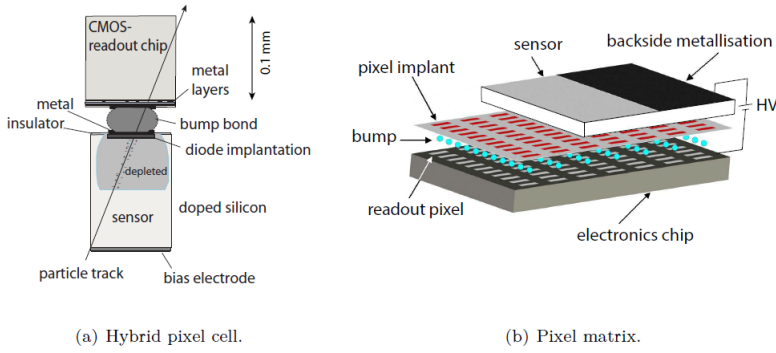


Figure 3.5: On the left (a), the structure of a single pixel cell, made by the sensor and the electronic readout. On the right (b), an exploiting representation of the entire hybrid pixel matrix arrangement.

### 3.2.2 Monolithic pixel detector

We have seen that hybrid detectors are made by the active sensor and the passive readout chip in two separate structures, connected by micro-connections. Since both of them are made of silicon, in principle, it could be possible to build them in a monolithic unit. In this way the amount of material decreases, enhancing the tracking performance and momentum resolution.

Developments of this sensors have tried to exploit industrial technologies already available, like the CMOS technologies. They have to reach a large depletion zone in order to improve the signal-to-noise ratio, but also design electrode with small capacitance, to reduce the power consumption and the noise. High radiation tolerance is also required.

An example of this type of sensor is the DEPFET pixel detector, which contains only one active transistor in every pixel. Monolithic Active Pixel Sensors (MAPS) employed CMOS technologies to include a readout circuit in their structure and we will see them in more details in section 3.3

#### Depleted p-channel field effect transistor (DEPFET)

In a DEPFET pixel detector, each pixel implements only one transistor. In Figure 3.6 is shown an example of a DEPFET pixel.

The depletion region extends between the backside  $p^+$  contact and the several  $p^+$  regions near the transistor element (drain, source and a  $n^+$  clear contact installed in a  $p$  region) and the  $n^-$  substrate. When a traversing particle releases energy, ionizing the medium, electrons drift towards the top surface, and the holes towards the backside due to the external potential.

The transistor is a p-channel MOSFET that produces a hole current from source to drain, controlled by the potential on the external gate. In addition, there is a deep  $n^+$  implant placed a few micrometers under the transistor. It is the most positive point in the pixel structure and so it is a local minimum for the electrons. In fact this implant features an electron accumulation, which changes the potential making it an *internal gate*. Electrons collected on this electrode, and the external gate influence the current flow in the DEPFET transistor channel. After the measurement, they are removed applying a positive voltage on the *clear contact*. In order to not compete as a collection electrode for the electrons, this element is embedded in a  $p$  region (*deep p-well*).

With some variations in the pixel structure, this is the type of sensors that PXD is made of.

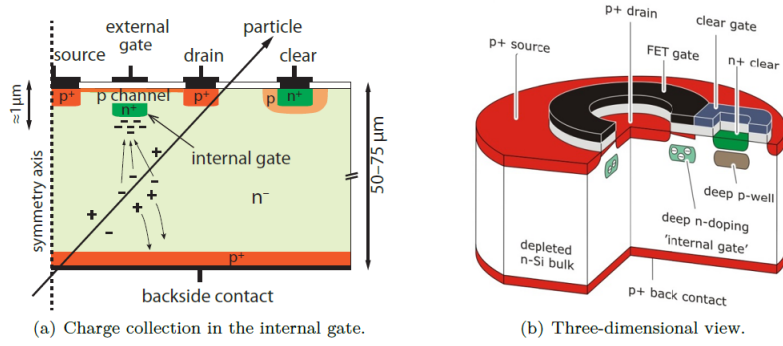


Figure 3.6: On the left (a) a cross section of a circular DEPFET pixel cell, where the charge collection is also sketched. On the right (b), a three-dimensional view of the same pixel cell.

### 3.3 CMOS Monolithic Active Pixel Sensors technology

First prototypes of pixel detector, which employed the CMOS technology to fabricate both the sensor and the readout circuit in the same silicon die, date back to the early 1990s. Further developments have led to the *monolithic active pixel sensors* (MAPS) with an epitaxial silicon layer for charge collection and then to the Depleted MAPS (DMAPS), where the depleted region is extended throughout the volume.

#### 3.3.1 MAPS pixel detectors

This type of sensors have been exploited the CMOS technologies for optical application, where the structure have an epi-layer with high resistivity to detect the light, and the electronic circuitry on the top of it. In this case, not the entire area is sensitive to the charge production. The effectively active fraction of the pixel area is called **fill factor**. In Figure 3.7 is shown a schematic of their structure.

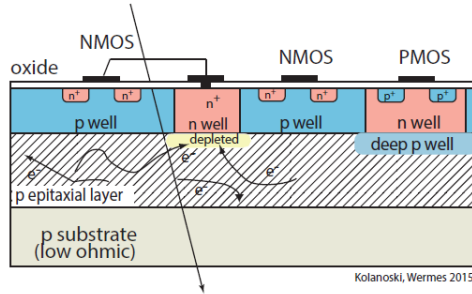


Figure 3.7: Schematic of a monolithic pixel detector (MAPS).

In MAPS pixel detector, charge collection is mostly achieved by diffusion, because the sensitive region is not fully depleted. The collection electrode is a  $n^+$  contact in a n-well, embedded in a p-epitaxial layer put on the top of a p substrate. Other n-wells can be necessary, for example to host PMOS transistors, and for this reason they have to be shielded by deep p-well,

to prevent them to become competitive for charge collection. These highly doped deep layers assume a negative potential with respect to the collection electrode and hence a repulsive effect. Due to the absence of a drift field in the epi-layer, with the exception of the region immediately below the collection electrode, collection charge occurs mainly by diffusion and thus it is slow and incomplete. Typical values of the epi-layer thickness are within the range of 1 - 20  $\mu\text{m}$  [6].

These MAPS detector cannot be used in high rates experiments because they have charge collection time of the order of 100 ns, thus too slow. The signal in this standard process is very small (typically  $\geq 1500 e^-$ ), due to the small thickness of the epitaxial layer, not even fully depleted, and they also have limited radiation tolerance. In fact due to Non-Ionising Energy Loss (NIEL) effects [7], radiation produces displacement damage in the sensor bulk also creating energy levels in the band gap that acts as trap centers. Electrons and holes can be trapped and then be released again after some time. This produce a decrease of the signal amplitudes if the de-trapping time constant is longer than the time of signal formation.

Although their limited radiation tolerance MAPS sensors have been successfully employed for heavy ions collisions, like STAR experiment at RHIC (Relativistic Heavy Ion Collider) [8] and the ALICE upgrade at the LHC [9].

### 3.3.2 Depleted MAPS pixel detectors

In order to obtain fast and fully collection of released charge, it is necessary to drift the carriers toward the electrodes, by an external electric field. A fully depletion of the sensitive zone enhances the charge collection, producing large signal (thus a better signal-to-noise ratio).

The depletion depth depends on the substrate resistivity and the bias voltage, according to the relation:

$$d \propto \sqrt{\rho V} \quad (3.2)$$

For this reason, new processing techniques have been employed to allow applying higher voltage or to process high-ohmic substrate wafers. Both of them are used to increase the depletion region underneath the collection electrode (typically to 25–150  $\mu\text{m}$ ) and so to provide sufficiently large and fast signal.

We can distinguish two main variants of DMAPS pixel detector [6]: with a *large* or *small* collection electrode, shown in Figure 3.8.

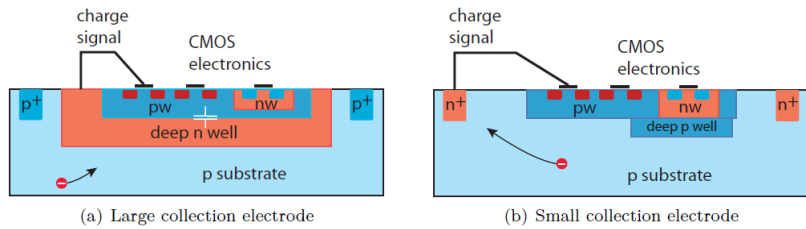


Figure 3.8: On the left (a) a schematic of the large electrode design. On the right (b) the small electrode design.

The *large collection electrode* DMPAS features a deep n-well acting as electrode but also as shield for the entire CMOS electronic readout, which is embedded within it. This architecture improves the radiation tolerance because the reduced average drift distance of the charge carriers decreases the probability of trapping. At the same time though, large size of the electrode im-

plicates higher values of capacitance (several hundred fF) which increases the noise and worsens the timing performance.

The *small collection electrode* variant has a small n-well collection node, distanced from the CMOS circuitry which is embedded in p-well and deep p-well layers. In this design, low capacitance of about 5-20 fF can be obtained, improving noise and timing performance. Radiation tolerance instead, is more difficult to reach due to larger average distance travelled by the carriers. Smaller pixel dimensions are preferred for small electrode (to reduce the path), and therefore higher power density is accepted in exchange of increased robustness against radiation.

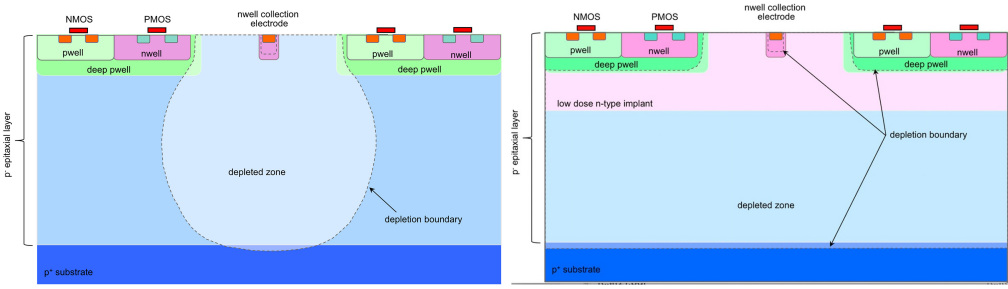


Figure 3.9: Small electrode design adopted in the ALPIDE sensor with the standard process (left) and the process modification with the addition of a low dose n-doped layer used to implement a planar junction and deplete the epitaxial layer over the full pixel area.

In the standard process adopted for the ALPIDE sensor [10] it is difficult to deplete the epitaxial layer over its full width as it is shown in Figure 3.9 left side. In order to achieve the full depletion of the sensitive layer, combined with a low capacitance collection electrode, a planar junction separated from the small collection electrode has been implemented. A low dose deep n-type implant has been used to realize a planar junction in the epitaxial layer within the pixel matrix below the wells containing circuitry, as shown in Figure 3.9. The epi-layer is thus depleted from two pn junctions: the deep p-wells and the low dose n-implant, the n-implant and the p-epitaxial layer [11]. This addition creates a potential minimum for electron collection underneath the deep p-well with a field direction towards the n collection well, thus strengthening collection of charges laterally[7]. The epi-layer is 25  $\mu\text{m}$  thick and the collection electrode is on positive potential. This modification of the technology has allowed to further improve radiation tolerance.

The most probable value (MPV) of the signal released by a Minimum Ionizing Particle (MIP) in the thin MAPS sensitive thickness ( $\approx 25 \mu\text{m}$ ) is only about 2000  $e^-$ .

The small charge signal achieved in the thin epi-layer (typically 1600  $e^-$ ) becomes a sizable voltage signal (about 50 mV) due to the small ( $\geq 5 \text{ fF}$ ) capacitance according to  $dV = dQ/CD$ . Therefore voltage (rather than charge) amplification is employed for the readout of small electrode MAPS.

### 3.3.3 Silicon On Insulator (SOI) technology

*Silicon on Insulator* (SOI) technology represents another way to combine the sensitive region and the readout circuit in a single monolithic unit. In this architecture, the transistor is isolated by vertical trenches and is divided from the bulk by a  $\text{SiO}_2$  layer, called *buried oxide* (BOX). An high resistivity bulk wafer allows to depleted the volum in the region below the BOX, in order to generate a large charge signal when a particle passes through the detector. The bulk and the

CMOS electronics are connected by vertical connections, called *vias*.

In Figure 3.10 is displayed a monolithic SOI pixel, with a doped volume placed between the CMOS circuitry and the BOX. This variation prevents the capacitive coupling from the substrate into the electronics, through the BOX.

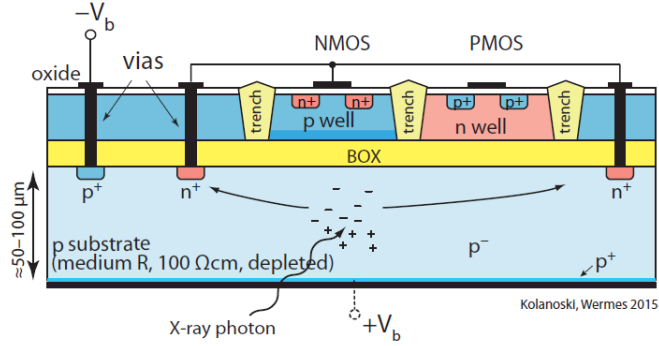


Figure 3.10: An example of a Monolithic SOI pixel.

## 3.4 History of Monopix developments

In recent years, advances in CMOS technologies have led to the development of a new generation of monolithic pixel sensors (DMAPS) with fast readout and high radiation tolerance. These new devices become promising candidate for high-energy physics experiment with high rates and high radiation environments.

### 3.4.1 Developments of DMAP devices

Specifically two different DMAPS development lines have been followed, distinguished by different pixel architectures, entrusted to two different implementation process technologies:

- **large fill factor** line: with large collection electrode and the electronics inside the charge collection well, these prototypes are indicate to experiments with high rate and high radiation conditions, because they could ensure a greater tolerance to huge doses of radiation. They have been fabricated in LFOUNDRY 150 nm design [12]. In Figure 3.11 are shown some of these chip developments.
- **small fill factor** line: with small collection electrode and the electronics outside the charge collection well, these devices need a process modification to enhance the radiation hardness. They are faster compared to the previous type, and due to less values of total capacitance, they implicate much less power consumption . They are fabricated in a TowerJazz 180 nm CMOS imaging process.

### 3.4.2 TJ-Monopix line

In Figure 3.12 is displayed the TowerJazz development line that have allowed to design the last iteration of this series, TJ-Monopix2, whose characterization results will be shown in Chapter 5.

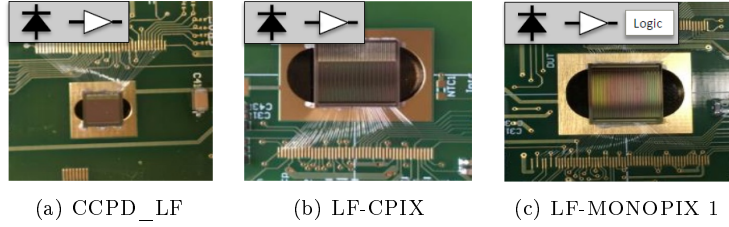


Figure 3.11: LFOUNDRY 150 nm development line.



Figure 3.12: TowerJazz 180 nm development line.

The standard TowerJazz 180 nm process has been employed to realize the ALPIDE monolithic active pixel sensor, selected for the ALICE Inner Tracking System (ITS) upgrade [9].

The chip proved to be suitable for the modest ALICE requirements, but the standard process do not ensure the full depletion volume, which is crucial to limit the signal degradation especially after irradiation. For this reason, the aforementioned process modification have been developed by CERN in collaboration with the foundry [11], that allows full depletion of sensitive layer. This new implementation has been tested in a dedicated chip called TJ-Investigator, and the obtained results have been demonstrated the effectiveness of the modified process.

Therefore two large scale demonstrator chips have been realized, called TJ-Monopix1 and TJ-Malta1 [13], whose main difference lies in the different readout architecture. The TJ-Malta1 chip implemented an *asynchronous* readout architecture, which eliminate the Bunch Crossing ID (BCID, timestamp), in order to reduce the digital power consumption. For TJ-Monopix1 instead, a *column-drain* readout architecture was chosen, which will be described in the following. Both chips have been fully tested and irradiated to investigate their functionality and efficiency, which however has decreased from 97 % to 70 % after irradiation with an equivalent neutron fluence of  $10^{15} \text{ n}_{\text{eq}}/\text{cm}^2$  [14].

The main reason for the efficiency drop has been discovered to be related to the weak lateral electric field at the pixel edges. So the process has been further optimized in order to resolve this issue. Two different approaches were found to increase the lateral electric field at the pixel borders [15]: creating a gap in the deep n-implant **n-gap** variant, requiring only a mask change, or introducing an additional p-type implant at the pixel border **extra deep p-well** variant. The n-gap variant is shown in Figure 3.13 compared to the previous version.

It can be seen the significant improvement of the electric lateral field, which results in turn in faster charge collection and so high efficiency even after irradiation.

Further optimization of the pixel size, which is critical to take full advantage of field shap-

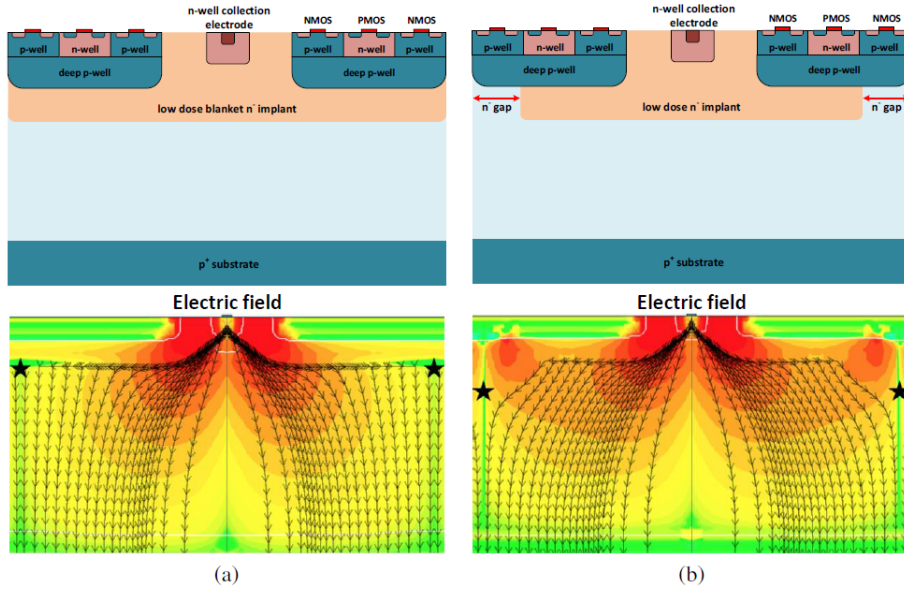


Figure 3.13: In the left, the Full deep p-well (FDPW) structure and its lateral electric field, compared with te Removed deep p-well (RDPW) variation. Both of them implemented the process modification with a low dose n implant.

ing through process modifications and to improve charge collection, have been implemented in the last iteration of this development line: TJ-Monopix2, considered as starting point for the development of the OBELIX final chip, designed for the upgrade of the Belle II vertex detector.

Now we want to describe the analog circuit and the readout architecture chosen for TJ-Monopix2.

### The Column-drain readout architecture

As we have seen in the previous, due to small capacitance of the small electrode MAPS, voltage amplification can be used to transform the charge signal arriving on the sensing node into a voltage signal.

In Figure 3.14 a schematic of the voltage amplification and the readout stages.

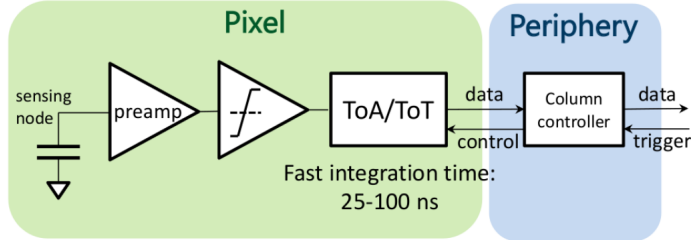


Figure 3.14: Sketch of the voltage amplification stages and the readout.

The charge signal produced by particles passing through and collected by the collection node, is converted in a voltage signal through a small capacitance. It goes in input to a pre-amplifier

which amplifies the signal and then send it to a discriminator. At this stage, the discriminator decides if discriminate the signal or not, on the base of its voltage threshold value. If the signal arriving from the pre-amplifier remains under the discriminator threshold, then it is not discriminate. If the signal goes above the threshold instead, the pulse is discriminate and its Time Over Threshold is measured (more about this in the following). Discriminator threshold is set by the means of some chip registers that we will see in . Data collected are send to the periphery in order to communicate and store them outside the chip.

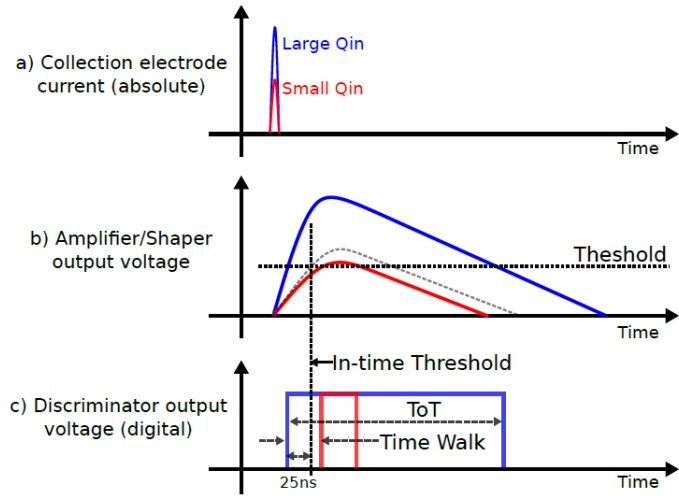


Figure 3.15: Time Over Threshold (ToT) technique.

The *column-drain* architecture implemented in TJ-Monopix ensures fast readout by encoding the analog charge information using the standard **Time Over Threshold (ToT)** technique Figure 3.15. This procedure exploits two timing information: the **Leading Edge (LE)** which corresponds to the hit time of arrival (when the signal value goes beyond the threshold), and the **Trailing Edge (TE)** that is when the signal goes below the threshold value. From the difference between the TE and the LE, the ToT can be calculated.

The *in-pixel* circuitry implemented a Random Memory Acces (RAM) where to store the LE and TE timing info, a Read-Only Memory (ROM) to store the pixel address and the control and arbitration logic, which we will see more about in the following.

The readout is *column-based*, so all pixels of each double column share a common column-bus which could be accessed by one pixel at a time, with a defined priority logic. The column bus includes the BCID timestamp, the data (LE, TE, address) and the control signals. The *periphery* includes the End Of Column (EoC) block which deals with the transmission and the readout of the column-bus signals, and the Digital Chip Bottom (DCB) that instead, processes the hit information.

The readout could be triggered or full-readout. In TJ-Monopix line hit data is continuously transmitted to the DAQ. In case of triggered readout instead, hit data is stored in a trigger memory, and the information is transmitted only when the trigger signal arrives.

In Figure 3.16 is displayed an example of the readout of two hits.

The readout sequence starts when the TE pulse arrived. A hit flag is set and it activates the **TOKEN** signal, which in turn is arised to warn that the pixel is available to be read out. This signal propagates across the double column with a priority logic until it arrives to a readout

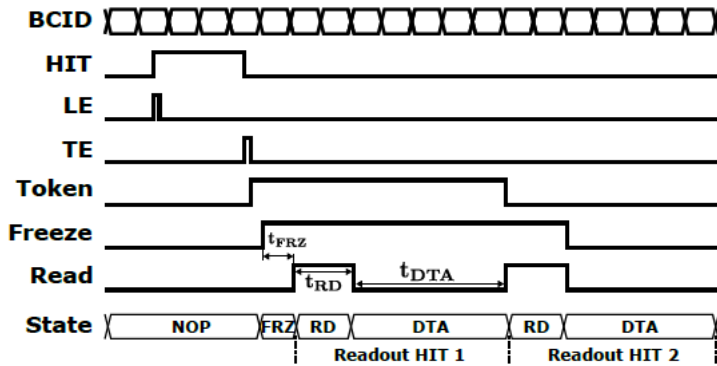


Figure 3.16: Schematic of a readout sequence where two hits are being processed.

controller, which uses other two global signals, the **FREEZE** and **READ**, to control the readout progression. They are distributed across the EoC blocks and local copies are transmitted only to the double column that has been hit and that has the higher priority (It is a different priority logic among each double column which goes from left to right across the matrix). The first ensures that new hits do not interrupt the pixel priority logic setting other new hit flag, which means that they could not transmit new hit information, but they could store it for the next readout sequence. In this way the pixel priority in each readout sequence is well defined. The **READ** signal instead, allows to the pixel with the hit flag and highest priority to access the data bus and transmit the hit information to the periphery. A series of **READ** cycles allow all pixels in the sequence to be read out.

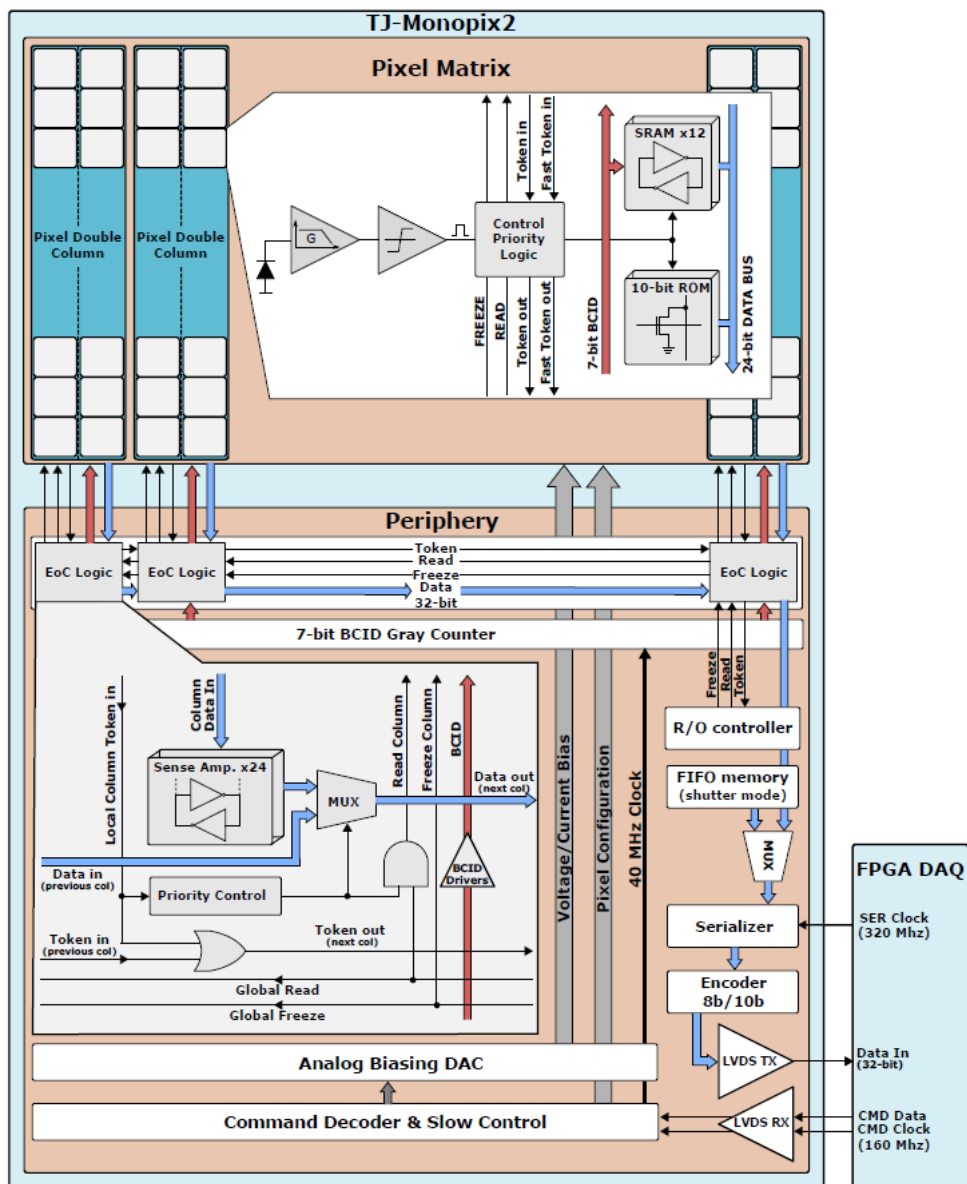


Figure 3.17: Architecture of TJ-Monopix2.

## 4. VTX detector

This chapter focuses on the vertex detector upgrade of Belle II, VTX. We will go through the VTX concept and layout, designed with a different geometry with respect VXD and with a new pixel sensors (OBELIX). We will discuss the motivations for some of the design choices and present some of the detector performance studies demonstrating the robustness against backgrounds.

### 4.1 VTX Layout and mechanical structure

As previously discussed, reaching full luminosity will entail higher backgrounds and will probably require a re-design of the interaction region. It is therefore necessary to use a radiation-hard technology, with high granularity to reduce occupancy, and with a reduced material budget to improve the already excellent performance of VXD.

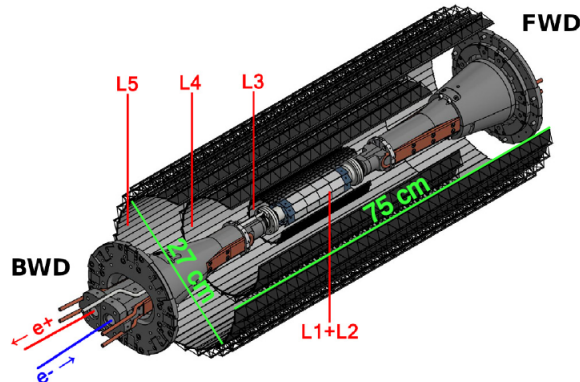


Figure 4.1: Concept of VTX layout with 5 barrel layers, filling the current VXD volume.

The VTX project aims to replace the all VXD with a fully pixelated detector based on Depleted Monolithic Active Pixel Sensors (DMAPS) arranged on five layers at different distance from the beam pipe (Figure 4.1). The radii and the number of the layers are currently subject to several studies and simulations, in order to achieve an optimized arrangement. Currently two layers are planned in the innermost part (*i*VTX) and three in the outer part (*o*VTX). The active length of the ladders varies from 12 to 70 cm to cover the required acceptance of  $17^\circ < \theta < 150^\circ$ . As already discussed for the other upgrade proposals, it is important to try to reduce the material budget, in order to minimize the multiple Coulomb scattering which particularly affects the very soft particles produced in Belle II, down to 50 MeV. By using the MAPS sensors, it is expected a reduction of the overall material budget down to 2% of radiation length, against the present

3% of VXD, which uses two DEPFETs and double-sided strip detectors.

#### 4.1.1 iVTX

The *internalVTX* consists of the first two detector layers assembled with a self-supported air-cooled all-silicon ladder concept, where four contiguous sensors are diced out of a single wafer, thinned and interconnected with post-processed redistribution layers. They are designed to be at 14 and 22 mm respectively from the beam pipe, and target an individual material budget of about 0.1% radiation length. This is achievable because the overall surface of these layers is moderate, below  $400 \text{ cm}^2$ , the sensor power dissipation is expected to be low, and the connections needed for the operation to be only a few. Air cooling should be a workable solution to remove the heat produced.

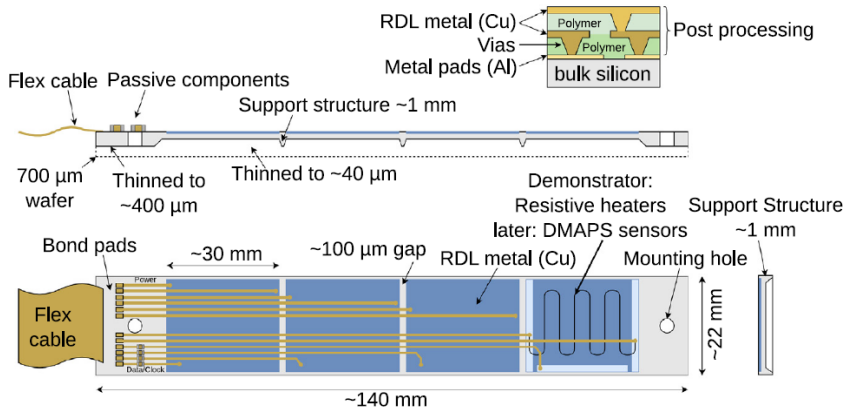


Figure 4.2: Sketch of the all-silicon ladder concept of the iVTX. Four dummy sensors are shown in blue on the silicon support in grey. The yellowish lines instead, indicate power and data transmission lines. Power is delivered to the ladder by a flex cable, which also transmits data to and from the chips in the final one.

The ladder has to be equipped with four OBELIX chips and thinned to 50  $\mu\text{m}$  except in some border regions, where a few hundreds of  $\mu\text{m}$  are necessary to ensure mechanical stability. In order to interconnect the sensors along the ladder and provide a unique connector at the backward end, during the post-processing metal strips are etched on the redistribution layer (RDL). The latter has the main purpose to route power and data via impedance-controlled transmission lines to a flex cable, added at the end of the ladder. After the RDL processing, the ladder is thinned as discussed above. Mounting holes will be added via laser-cutting.

Figure 4.2 shows a sketch of the iVTX demonstrator ladder (currently under production), 140 mm long and 22 mm wide (grey). Instead of the actual sensors, it is equipped with four dummy chips with a length of about 30 mm (blue), holding resistors to mimic the expected heat load to test the air cooling system and more generally to characterize the electrical, mechanical and thermal performance of the ladder. A redistribution layer for power and data is also added to the demonstrator, to connect the chips with a flex cable at the end of the ladder (yellowish lines). The wafer thickness is reduced to 400  $\mu\text{m}$ , while the sensitive areas are thinned down to 40  $\mu\text{m}$  with the purpose to test the mechanical integrity of the whole structure.

The R&D is ongoing and the full-silicon ladder concept is currently being assessed with industrial partners. The first thin ladders have been produced and characterised with different

thicknesses and geometries.

Several tests are focused on evaluating power delivery efficiency, the quality of the signals which travel through the ladder and also the process used to fully assembly it. Figure 4.3 shows eye diagrams from simulation with a transfer rate of 640 Mbps, indicating that 320 Mbps of data rate will be possible.

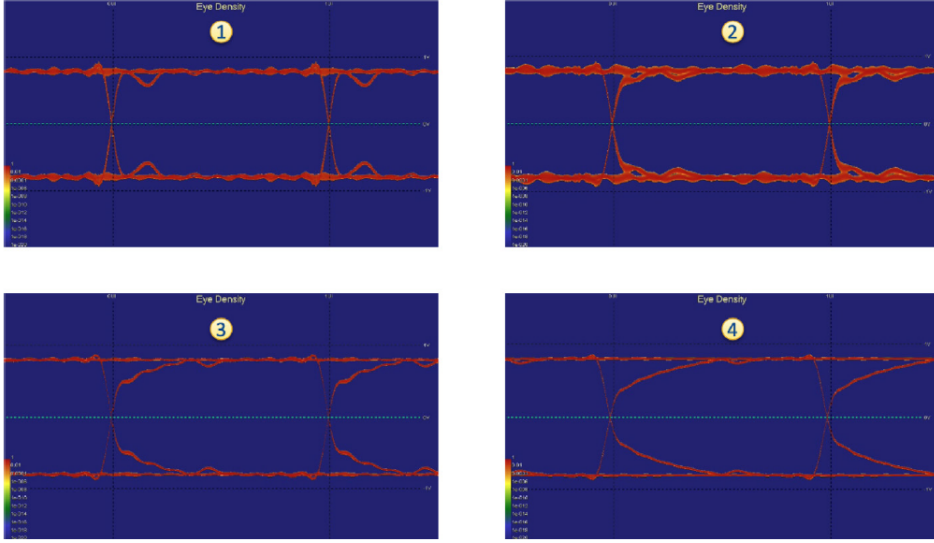


Figure 4.3: Eye diagrams of the iVTX data transmission lines at four different locations on the ladder. They represent the overlap of multiple samples of the output of transmission line triggered by the clock cycle.

Moreover it has been demonstrated that air at the temperature of 15 °C and flowing with a speed of 10 m/s succeeds to cool a single inner module, assuming power is uniformly dissipated on the sensor surface. The maximum temperature reached is 20 °C.

Through very first estimates it is expected that an equivalent section of 6 tubes with 10 mm of diameter is necessary to expel the heat from the inner layers, roughly equal to 65 W. So it is essential to design a mechanical structure which provides for the space needed to the tubes in order to bring the air at the IP and also compatible with the new interaction region.

#### 4.1.2 oVTX

The **outer VTX** consists of three layers respectively at radii of 39 or 69, 89 and 140 mm from the beam pipe. Because of the larger distance required to cover the acceptance, they cannot be self-supporting. They follow a more traditional approach, inspired by the design developed for the ALICE ITS2 [16]. Each ladder is water cooled and supported by a light carbon fiber support structure, which provides the mechanical stiffness. Its truss design is shown in Figure 4.4 : 70 cm long and 5.8 g of weight, it is able to support more than 40 sensors in two rows next to each other with a small overlap, leading to a material budget of 0.3%  $X_0$  for the first two layers and 0.8%  $X_0$  for the outermost one.

For the cooling of the ladder a cold-plate concept is under development (Figure 4.5), on which the sensors are glued and that in turn is installed on the *truss*. For each row there is a polyimide cooling tube that runs over all the sensors and turns back at the other end, so that the heated

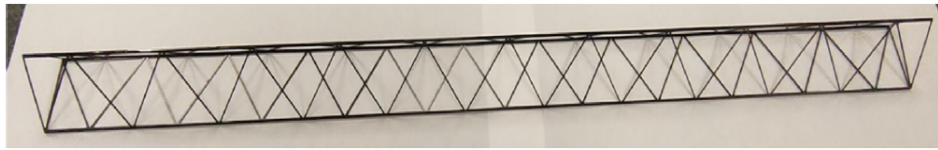


Figure 4.4: Prototype of the layer 5, called *truss*, which is the longest, made from thin carbon fibre structures.

coolant leaves on the same side. Then two flex print cables connect the two halves of the ladder to the connector.



Figure 4.5: A prototype of the cold-plate for cooling. One coolant tube(golden) is connected to the cold plate(black) and turns  $180^\circ$  on the other end (not shown) so that the coolant flows in both directions and thus leaves on the same side it starts.

For layer 3 instead, only one flex print cable in the backward side is considered, in order to leave more space in the forward for other possible services and accelerator components. For the third layer two different solutions are under study: at radius of 39 mm e 69 mm respectively. In Figure 4.6 are displayed schematic examples of some design hypotheses.

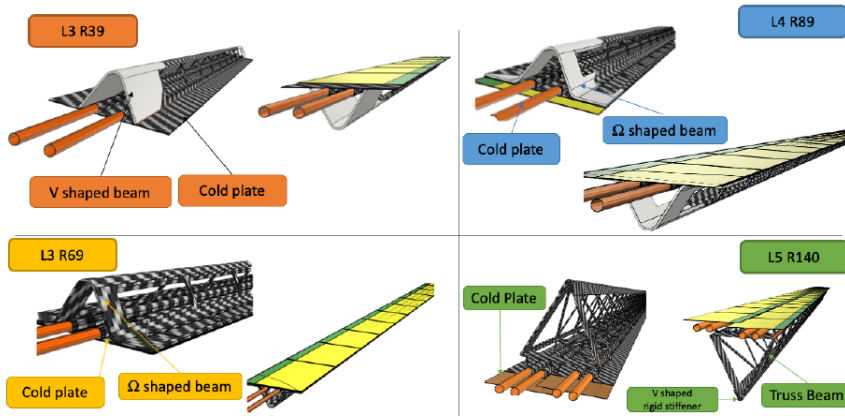


Figure 4.6: Schematic view of possible solutions for the three outermost layers.

In Figure 4.7 are shown the several substructures described before, that constitute a ladder of the outermost layer 5. From bottom to top come in succession the carbon fibre structure, two cold-plates for the two neighbouring sensor rows (indicated as "Chips", in grey) and the flex cables for power and data transmission (green).

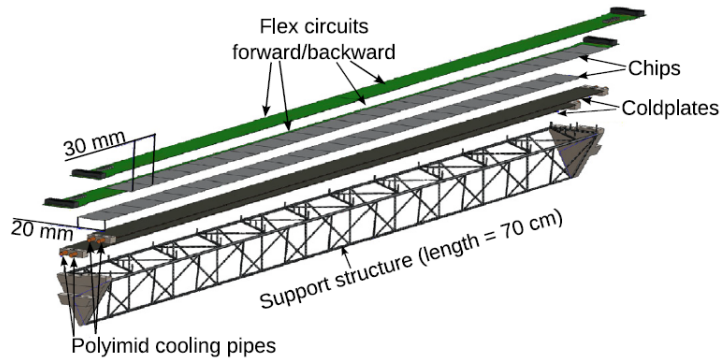


Figure 4.7: An exploding drawing of a fully assembled layer 5 ladder.

The carbon fiber support structure and flex cable have been designed and fabricated for layer 5, which is also the longest. Services for the last two layers, like electrical connections and cooling, can be provided both on forward and backward sides. A Multiline Power Bus has been realized in order to power each OBELIX chip along the ladder.

Mechanical tests have been performed showing that the first resonance frequency is at 200 Hz, which is safely far from the frequencies of the typical earthquakes in Japan.

To reduce as much as possible the material budget, the transmission lines and the flex cables must be as thin as possible, but they also have to ensure safe data transmission.

For this reason, the outermost ladders (70 cm long) are equipped with two flex cables, one from each side of the *truss*. In Figure 4.8 the resulting eye diagram from testing the signal integrity of one of the 35 cm long transmission lines for data transmission rate of 500 Mbps is shown. This result demonstrates that the bandwidth is large enough to allow the needed 160 Mbps for data transmission.

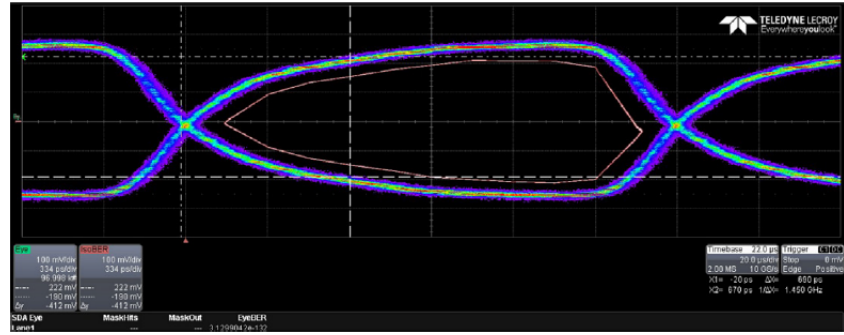


Figure 4.8: Eye diagram for the oVTX transmission line signal integrity of the layer 5 flex cable.

In addition, thermal tests have been performed for the last layer prototypes using kapton heaters to emulate the power dissipation of the chips. The coolant (demineralized water) has been set to a temperature of 10 °C at the beginning, the environment at 20 °C with a negative pressure of 0.2 bar. Results have demonstrated that for three different configurations of the flow

(such as monodirectional, bi-directional and with an U-turn at one end) the average temperature stands at  $24^{\circ}\text{C}$  with a maximum gradient of  $\Delta T \approx 4^{\circ}\text{C}$  along the full length of the ladder.

All these investigations validate the design of the longest ladder, which is the most challenging, and therefore the possibility to operate the chips safely.

## 4.2 Performance simulation

As we have seen in Chapter 2, increasing the luminosity implies higher level of machine related background and so larger doses of radiation, especially in the inner layers of the whole detector. For these reasons simulations and studies are focusing on ensuring that the main physics goals of the experiment will be achieved despite the more severe working conditions.

The VTX detector, with high granularity in both space and time and thin sensors, could bring significant improvements in tracking efficiency and resolution especially at low momentum, in the impact parameter resolution, and in the robustness against backgrounds. Moreover, better vertexing performance entails not only improved time-dependent analyses of B and D mesons, but also an enhanced capability to distinguish among different decay topologies, and a more powerful rejection of background events.

### 4.2.1 VTX geometries

Two different VTX geometries are currently under study, which differ only in the position of the third layer (Figure 4.6).

The *nominal* geometry is expected to maximize the track impact parameter resolution and it places the third layer at 39 mm from the IP. The *alternative* geometry instead, aims to improve the  $K_S^0$  reconstruction efficiency and the third layer is located at 69 mm from the IP.

Simulations are ongoing to compare the performance of these two different layouts with that of the current Belle II detector (utilizing a full Geant4 simulation of the detector in the study of specific decay modes of interest). Moreover, the different machine background predictions are also simulated, to compare the detector performance under different background conditions.

### 4.2.2 Tracking efficiency at low momentum and impact parameter resolution

Tracking efficiency at low momentum is one of the areas where the VTX upgrade provides the most promising results, particularly for the *soft pions* originated from the decays of  $D^{*\pm}$  mesons.

Studies are based on the reconstruction of the decay chain  $B^0 \rightarrow D^{*-} l^+ \nu$ , with  $D^{*-} \rightarrow \bar{D}^0 \pi_{soft}^-$  and  $\bar{D}^0 \rightarrow K^+ \pi^-$  or  $K^+ \pi^- \pi^+ \pi^-$ . All background scenarios mentioned in section 2.2.2 are considered in the evaluation of the *nominal* VTX performance and they are compared with the nominal Belle II geometry in the intermediate (**v2**) background hypothesis.

We can see in Table 4.1 that the VTX reconstruction efficiency<sup>1</sup> in all three background hypotheses, is improved by almost a factor 1.7 with respect to the nominal Belle II, with comparable purity<sup>2</sup>. Moreover, efficiency remains practically stable in all background conditions, even in the most severe one.

---

<sup>1</sup>Efficiency is defined as the ratio between the number of correctly reconstructed signal events and the total number of candidates.

<sup>2</sup>In a few words, the probability that a correctly reconstructed signal is a "signal event".

	Belle II (v2)	VTX (v1)	VTX (v2)	VTX (v3)
Generated events	32533	32559	32559	30255
Correctly reconstructed signal	10059	16913	16848	15583
Combinatorial	28495	51375	51826	47527
Efficiency	30.9%	51.9%	51.7%	51.5%
Purity	26.1%	24.8%	24.5%	24.7%

Table 4.1: Reconstruction efficiency and purity for the decay chain  $B^0 \rightarrow D^{*-} l^+ \nu$ , with  $D^{*-} \rightarrow \bar{D}^0 \pi_{soft}^-$  and  $\bar{D}^0 \rightarrow K^+ \pi^-$ , for the nominal Belle II detector at the intermediate background conditions (**v2**) and the nominal configuration of VTX in all three background scenarios.

This enhancement in tracking efficiency relies in particular on improved tracking efficiency for the  $\pi_{soft}^-$  mesons, as we can see in Figure 4.9 where the efficiency is shown as a function of momentum and polar angle.

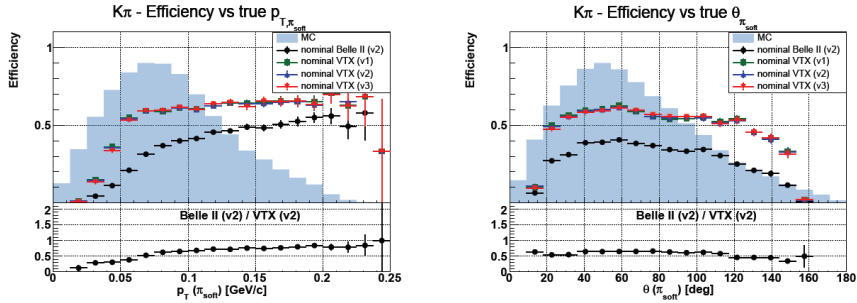


Figure 4.9: Reconstruction efficiency of  $B^0 \rightarrow D^{*-} l^+ \nu$  as a function of the transverse momentum of the  $\pi_{soft}^-$  (from  $D^{*-} \rightarrow \bar{D}^0 \pi_{soft}^-$ ) in the plot on the left and of the polar angle of the  $\pi_{soft}^-$  on the right. The shaded blue histograms represents the momentum spectrum of the  $\pi_{soft}^-$ . The nominal Belle II geometry efficiency in the intermediate background scenario (**v2**) is represented by black dots and it is compared with the nominal VTX configuration in the optimistic (**v1**, green squares), medium (**v2**, blue upward pointing triangles) and pessimistic (**v3**, red downward pointing triangles) background hypotheses. The bottom plots show the ratio between nominal Belle II and nominal VTX in the **v2** background scenario.

#### 4.2.3 Vertexing resolution

Studies on vertexing performance have been conducted using samples of one million  $B^0 \rightarrow J/\psi K_S^0$  events generated and reconstructed with all the aforementioned combinations. The distributions of the decay vertex resolution  $\sigma_z$  (i.e. the width of the distribution obtained considering the differences between the measured and the true simulated positions) along the  $z$  axis of the B decay signal are shown in Figure 4.10 .

In Table 4.2 a summary of the results that shows that the new geometries achieve a better resolution on the B decay vertex of about 35% on average and they also do not suffer of any significant degradation as the background conditions varies, unlike the nominal Belle II configuration.

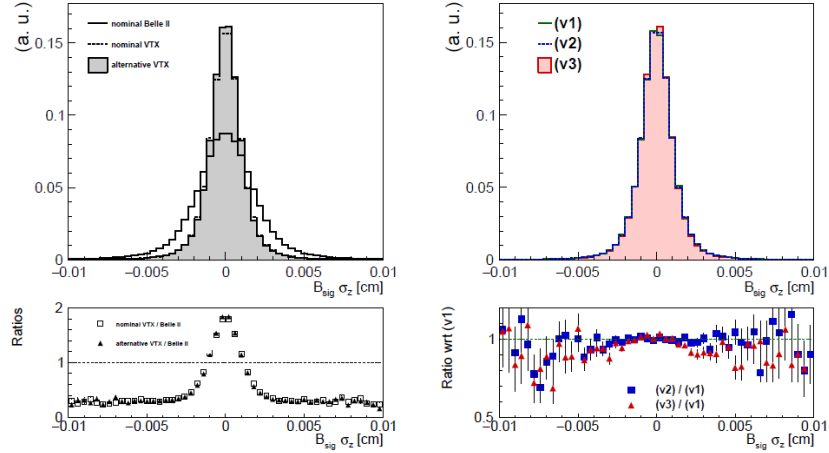


Figure 4.10: On the left: comparison of the B decay vertex resolution along the  $z$  axis in  $B^0 \rightarrow J/\psi K_S^0$  events for the nominal Belle II (solid line), nominal VTX (dotted line) and alternative VTX geometry (filled grey histogram). The bottom plot shows the ratio between the VTX geometries (empty squares the nominal one and filled triangles the alternative) and nominal Belle II.

On the right: B decay vertex resolution along the  $z$  axis for the nominal VTX geometry in the three background scenarios: optimistic **v1** (green solid line), intermediate **v2** (blue dotted line) and pessimistic **v3** (red filled histogram). The bottom plot represents the ratio between the two higher background scenarios and the optimistic one.

Similar studies for the  $K_S^0$  decay vertex resolution are displayed in Figure 4.11 and in the same way, the upgraded geometries reach a better vertexing resolution with respect to the nominal Belle II detector without any significant degradation as the backgrounds increase.

$B_{sig}$ $z$ vertex resolution ( $\mu\text{m}$ )	Bkg (v1)	Bkg (v2)	Bkg (v3)
Belle II	21.9	23.0	24.9
Nominal VTX	14.5	14.4	14.1
Alternative VTX	14.4	14.3	14.0

Table 4.2:  $B_{sig}$  vertex resolution along the  $z$  axis for the three detector layouts and the three background scenarios.

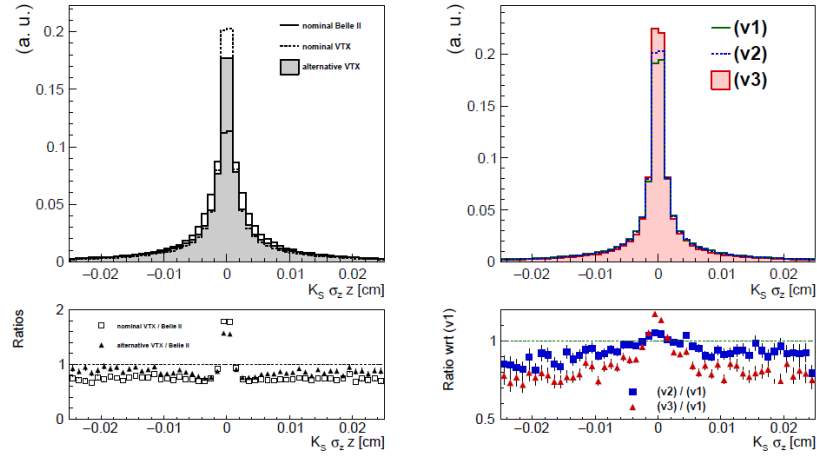


Figure 4.11: On the left: comparison of the  $K_S^0$  decay vertex resolution along the  $z$  axis in  $B^0 \rightarrow J/\psi K_S^0$  events for the nominal Belle II (solid line), nominal VTX (dotted line) and alternative VTX (filled grey histogram). The bottom plot shows the ratio between the VTX geometries (empty squares for the nominal and filled triangles for the alternative) and nominal Belle II detector. On the right:  $K_S^0$  decay vertex resolution along the  $z$  axis for the nominal VTX in the three background scenarios: optimistic **v1** (green solid line), intermediate **v2** (blue dotted line) and pessimistic **v3** (red filled histogram). The bottom plot represents the ratio between the two higher background scenarios and the optimistic one.

## 4.3 OBELIX chip design

The VTX detector is designed with a single type sensor optimized for the specific needs of Belle II, called OBELIX (Optimized BELle II pIXel sensor) and currently under development, based on fast and high granular Depleted Monolithic Active Pixel Sensor (DMAPS). This sensor design comes from an evolution of TJ-Monopix2, whose characterization is the main topic of this thesis, and which will be discussed in Chapter 5. Both of them are fabricated in a modified TowerJazz Semiconductor 180 nm CMOS process.

### 4.3.1 Sensor specification

The main design specifications for the OBELIX chip are listed in Table 4.3.

Pixel pitch	30 to 40 $\mu\text{m}$
Matrix size	512 rows $\times$ 928 to 752 columns
Time stamping	25 to 100 ns precision over 7 bits
Signal Time over threshold	7 bits
Output bandwidth	320 to 640 Mbps
Power dissipation	100 to 200 mW/cm <sup>2</sup>
Radiation tolerance	100 MRad and $10^{14}$ n <sub>eq</sub> /cm <sup>2</sup>

Table 4.3: Designed specifications of the OBELIX sensor.

The pixel pitches<sup>3</sup> are designed to be from 30  $\mu\text{m}$  to 40  $\mu\text{m}$  in both directions. This range is necessary to achieve a spatial resolution below 15  $\mu\text{m}$ , which is required to obtain sufficient tracking performance.

Moreover the sensor thickness has to be below 100  $\mu\text{m}$  to respect the material budget constraint of 0.2%  $X_0$  (100  $\mu\text{m}$  Si correspond to 0.1%  $X_0$ ) which is possible with the DMAPS technology. To deal with the target hit rate of 120 MHz/cm<sup>2</sup>, the timestamp clock signal can reach down to 25 ns, even if studies have demonstrated that a window of 100 ns (*integration time*) is enough to limit to 320 Mbps the data throughput at the same expected hit rate. All characteristics inspected above allow to realize a sensor with high granularity in both space and time.

With respect to TJ-Monopix2, which is equipped with a triggerless column-drain readout without memory at the periphery, OBELIX must have a triggered readout architecture, in order to satisfy the needs of Belle II. Moreover the latency is fixed to 10  $\mu\text{s}$  and it might operate up to 30 KHz trigger rate.

Single Event Upset ?? is a concern for the operation of the future detector but its size has not yet been quantified. Therefore an important feature of the chip must be to ensure that the control system is able to reset the sensor registers to default operational values at least every minutes. The reset frequency will be chosen after the measurement of the SEU cross section with OBELIX and the comparison to the occurrence distribution of large energy loss in the experiment.

The expected power consumption instead, is expected to be about 200 mW/cm<sup>2</sup>, a value which should allow air-cooling for the small areas corresponding to the two inner layers and liquid coolant for the outer ones.

---

<sup>3</sup>The distance between the centers of two contiguous pixels.

### 4.3.2 Sensor implementation

A schematic layout of the chip is shown in Figure 4.12 . The size of the sensor is expected to be  $3 \times 1.9 \text{ cm}^2$ , with an active area of  $3 \times 1.6 \text{ cm}^2$  and an additional part in the periphery of about  $3 \times 0.3 \text{ cm}^2$ , dedicated to data pre-processing and triggering.

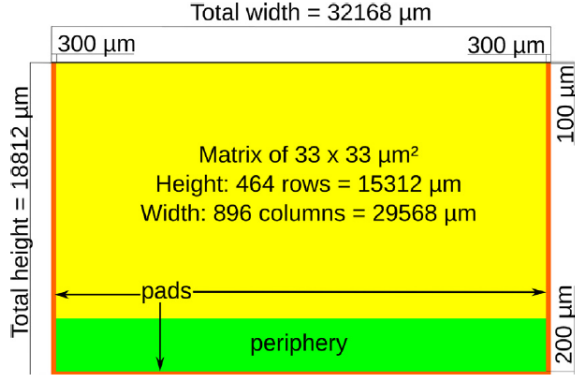


Figure 4.12: OBELIX chip layout.

As mentioned above, this new sensor is the development of TJ-Monopix2, whose characteristics fit already many of the Belle II requirements (Table 4.4).

	Specification	TJ-Monopix2
Pixel pitch	< 40 $\mu\text{m}$	< 33 $\mu\text{m}$
Sensitive layer thickness	< 50 $\mu\text{m}$	30 $\mu\text{m}$ and 100 $\mu\text{m}$
Sensor thickness	< 100 $\mu\text{m}$	-
Hit rate capability in the matrix	> 600 MHz $\text{cm}^{-2}$	> 600 MHz $\text{cm}^{-2}$
Hit rate capability at the sensor output	> 120 MHz $\text{cm}^{-2}$	$\gg$ 100 MHz $\text{cm}^{-2}$
Trigger delay	> 10 $\mu\text{s}$	-
Trigger rate	30 kHz	-
Overall integration time	< 100 ns	-
(optional) Time precision	< 50 ns	-
Total ionizing dose tolerance	100 kGy/year	1 MGy/year
NIEL fluence tolerance	$5 \times 10^{13} \text{n}_{\text{eq}}/\text{cm}^2/\text{year}$	$1.5 \times 10^{15} \text{n}_{\text{eq}}/\text{cm}^2/\text{year}$
SEU tolerance	frequently ( $\text{min}^{-1}$ ) flash configuration	-
Matrix dimensions	around $30 \times 16 \text{ mm}^2$	$19 \times 19 \text{ mm}^2$
Overall sensor dimensions	around $19 \times 19 \text{ mm}^2$	$20 \times 19 \text{ mm}^2$
Powering	through voltage regulators	-
Outputs	one at < 200MHz	one at 160 MHz

Table 4.4: Comparison between BELLE II requirements and TJ-Monopix2 features.

From TJ-Monopix2 design, the pixel size of  $33 \times 33 \text{ }\mu\text{m}^2$  is maintained, as well as the layout of both digital and analog parts (section 3.4.2). Also the Time-Over-Threshold method to digitize the signal is preserved, with a bus width of 7 bit, together with the column-drain readout architecture implemented for pairs of columns. Other features, which will be explained in depth in Chapter 5, have been conserved in the new design like the 3-bit register dedicated to the threshold tuning, but with a larger range of correction for the last bit. Moreover to aim at the integration time of 100 ns, the clock frequency which defines the precision of ToT and BCID (that is the timestamp), has been decreased from 40 to 20 MHz. So the current baseline for OBELIX timestamp precision is 50 ns.

Additionally two new modules have been added to the implementation, related to the Belle II trigger: the Trigger Logic Unit (TRU) and the Track Trigger Transmitter (TTT).

## Trigger Logic Unit (TRU)

The TRU has the task to select the fired pixel information from the matrix which are in-time with the triggers sent by the Belle II system. In more details, this module employs two stages of memory in order to manage the data coming from the pixel matrix (Figure 4.13). These components are designed in order to minimize power dissipation and to optimize the efficiency even in severe operating conditions: maximum hit rate of  $120\text{ MHz}/\text{cm}^2$ , 30 KHz of trigger rate and  $10\text{ }\mu\text{s}$  of trigger delay.

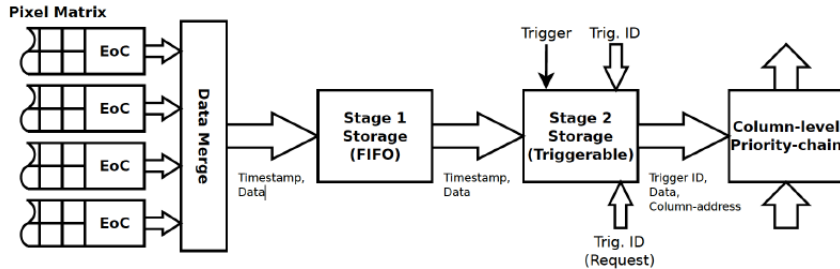


Figure 4.13: Schematic of the Trigger Logic Unit.

The first stage has to store the pixel information during the trigger delay. The second memory instead, has the function to compare the BCID of the fired pixel with each trigger time information buffered in a dedicated global memory which keeps track of received triggers. When they have a match, the pixel data is transferred to the Transmission Unit (TXU). In this way, the physics hits associated to a trigger but timestamped with a later BCID, for example due to timewalk effect, are also considered for further analysis. Considering the BCID precision time, the time integration of the OBELIX sensor becomes  $100\text{ ns}$ .

## Track Trigger Transmitter (TTT)

The TTT module divides the matrix in 8 logic regions (this value is still under study) and generates a one-byte word depending on the region that is fired. It is expected that this information could be transmitted to trigger system within  $100\text{ ns}$  and along a line of transmission parallel to the main data output of the sensor. This component behaviour is still under study and it needs of further simulations in correlation with the whole VTX system.

## Control Unit (CRU) and power dissipation

The OBELIX sensor, as well as TJ-Monopix2, is configured by several registers which allow to set important features for its operation like threshold settings, masked pixels, time response of the pixels, but they also define its power consumption. The Control Unit is responsible for receiving these instructions about the configuration and the trigger information and at the same time sending out data coming from TXU module.

For what concern power dissipation, there are three main features which have the greatest impact: the biasing current flowing into the in-pixel amplifier ( $I_{BIAS}$ ), the BCID clock frequency (on which depends the timestamping precision) and the hit rate. In Figure 4.14 is shown the estimations of power dissipation as these parameters vary.

As we can see, the power consumption at the maximum hit rate of  $120\text{ MHz}/\text{cm}^2$  exceeds by little more than 10% the power budget of  $200\text{ mW}/\text{cm}^2$ , considering the higher precision for

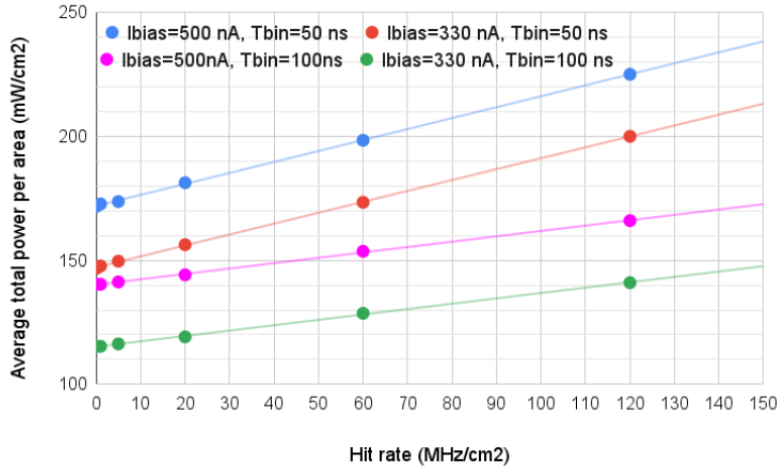


Figure 4.14: OBELIX sensor power dissipation depending on the front edn current ( $I_{bias}$ , the BCID frequency ( $t_{bin}$ ) and the hit rate).

the timestamp of 50 ns. Therefore to stay within the power budget it is necessary to find a compromise: reducing timing precision by worsening the BCID precision to 100 ns or decreasing the pre-amplifier biasing current causing a degradation of the time walk.

The first version of the sensor, called OBELIX-1, is being designed and the submission for fabrication is planned in the last month of 2023. A second improved version, OBELIX-2, will be designed based on performance studies on the first version and it is expected that it will be the final sensor needed for the experiment.

## 5. TJ-Monopix2 characterization

In the previous chapter we have seen the fundamental steps that had lead to the development of the CMOS MAPS sensors technology and the history of their many different prototypes. Here we will go through the main features of TJ-Monopix2 designed to address efficiency degradation after irradiation, one of the main issues of its predecessor TJ-Monopix1. The characterization of the chip is crucial in the VTX upgrade program and in the design of the next OBELIX chip.

The chip W14R12, which is one of the sensors tested during the first Test Beam campaign in Desy (July 2022) has been fully characterized in Pisa and in particular several aspects have been analyzed, among which:

1. TOT calibration by internal charge injection;
2. characterization with radioactive sources and absolute calibration;
3. systematic study of different registers' settings in order to operate the chip at low thresholds;
4. investigation of an important issue with cross-talk, due to digital signal from the readout, discovered trying to operate the matrix at low threshold (below  $250 e^-$ ).

This detailed characterization returned crucial results (1, 2) for the Test Beam data reconstruction and the simulations of the upgraded VTX detector with CMOS MAPS devices. Furthermore the optimization of the registers to reduce the operating threshold was very useful for the preparation of the next TB (July 2023) campaign with irradiated sensors.

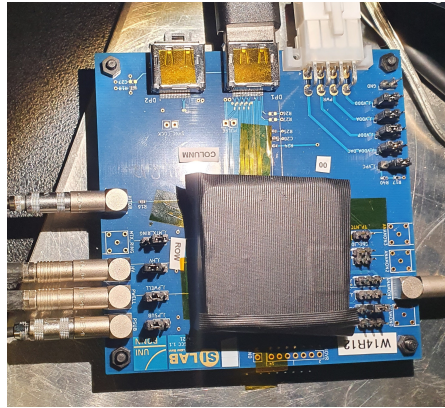


Figure 5.1: The W14R12 chip tested during the Test Beam in Desy.

## 5.1 Matrix and flavors

TJ-Monopix2 is the next generation small collection electrode DMAPS prototype in TowerJazz 180 nm. The need to create a sensor capable to mantain high efficiency even after irradiation, required improvements compared to TJ-Monopix1 in two important fields: a lower operating threshold to keep a good efficiency with the reduced charge collected after irradiation and smaller pixel pitch to increase charge collection efficiency all over its area, expecially in the corners.

To achieve these goals, a different in-pixel front-end circuit was implemented and a lot of efforts have been focused on optimizing pixel layout in order to reduce its size, which has been decreased from  $36 \times 40 \mu\text{m}^2$  in TJ-Monopix1 to  $33.04 \times 33.04 \mu\text{m}^2$  (pixel *pitch*). The pixel dimensions are critical to accomplish faster charge collection across all active area, increasing the lateral electric field. For this reason it was necessary a special effort to design and create a smaller pixel but still adequate to embody the full digital readout. All of this required to work at the technology density limit and also to study for further modifications at the circuit design.

In order to operate with a lower threshold TJ-Monopix2 incorporates an improved front-end circuit that reduces the noise by  $\approx 40\%$  and the threshold dispersion by about 80-90% with respect to TJ-Monopix1. Furthermore, in-pixel threshold tuning has been integrated in order to achieve a more uniform threshold distribution across the pixel matrix, particularly after irradiation. As a result of these improvements, the operating threshold was expected to be at  $\approx 100 e^-$ , three times lower than in TJ-Monopix1.

### 5.1.1 Flavors

The prototype is a  $2 \times 2 \text{ cm}^2$  pixel matrix which consists of  $512 \times 512$  pixels and all of them are designed with a reduced deep p-well geometry (RDPW) because, as it was demonstrated during the testing of TJ-Monopix1, this type of arrangement has superior charge collection properties compared to full deep p-well coverage (FDPW) (Figure 5.2). The total active area of the matrix is approximately  $286 \text{ mm}^2$  and it is  $300 \mu\text{m}$  thick.

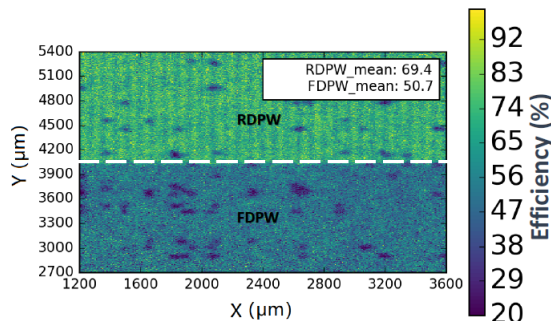


Figure 5.2: Detection efficiency map of a TJ-Monopix1 chip with  $25 \mu\text{m}$  p-epitaxial layer that has been irradiated to  $10^{15} n_{eq}/\text{cm}^2$  NIEL.

As we can see in Figure 5.3, the matrix is divided in four sectors, named **flavors** that implement different variation of the front-end circuit. In the first two flavors the collection electrode is DC-coupled directly with the readout electronics, the continuous baseline reset is implemented by a forward bias diode and they differ for the pre-amplifier circuit design. The second flavor indeed, named **Cascode FE**, includes an extra-cascode transistor that increases the pre-amplifier gain

which in turn leads to a 50% reduction of the threshold dispersion compared to the first flavor, the **Normal FE**. The other two flavors consist of AC-coupled pixels (through a metal-oxide-metal MOM capacitor) and in particular, the **HV-Cascode FE** also incorporates the aforementioned pre-amplifier variation. AC-coupling allows to apply an high positive bias voltage (HV stands for High Voltage) to the collection electrode which potentially enlarges the depleted region, but at the same time it also causes signal losses mainly due to the additional parasitic capacitance introduced at the sensitive input node.

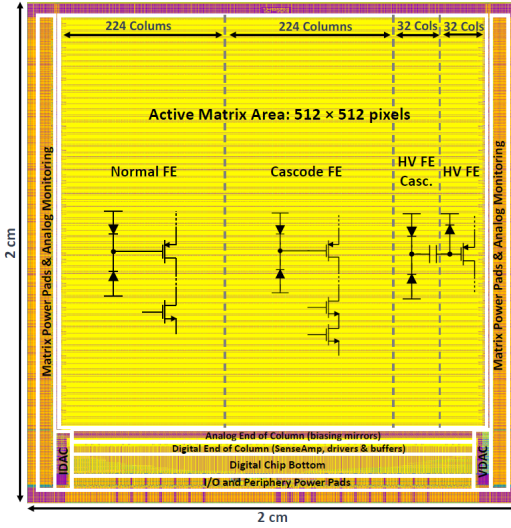


Figure 5.3: The layout of the TJ-Monopix2 prototype divided in four different flavors: **Normal**, **Cascode**, **HV-Cascode** and **HV FE**.

### 5.1.2 Pixel design

The  $2 \times 2$  pixel core layout, shown in Figure 5.4, is fully optimized and is designed in order to share as much features as possible between the four pixels. The analog area incorporates the front-end circuit, the 3-bit threshold tuning DAC and the pixel configuration registers. The digital region is composed by the 7-bit LE and TE memory (14 SRAM cells per pixel), the 10 bit address ROM (2 bit for the pixel position inside the core and 8 for the group address) and the readout control logic.

#### 5.1.2.1 Improved front-end circuit design

As we have seen above, there are two variations of the front-end circuit (Figure 5.5), such as *normal* and *cascode* type. The latter in particular includes an extra cascode transistor which increases the pre-amplifier gain and consequently reduces the threshold dispersion.

Moreover in TJ-Monopix2 it was preferred to incorporate a simple diode to reset the input node instead of a PMOS transistor, which was the technology implemented in TJ-Monopix1. A side effect of this choice is that the relationship between charge injected and the ToT of the detected signal is not linear anymore, because the diode is a not linear element and its discharge rate also depends on the collected charge. Indeed in the following analysis it was necessary to fit the ToT

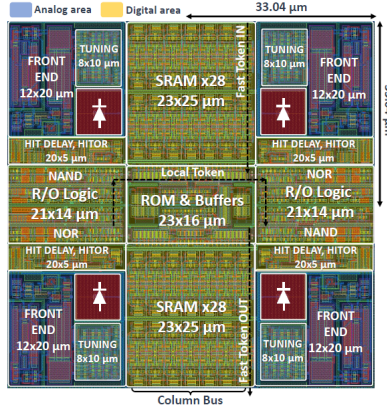


Figure 5.4: Layout of a TJ-Monopix2  $2 \times 2$  pixel core. In blue the analog area and in yellow the digital one.

trend with a more complex function. But at the same time, the advantages are its simplicity ( $p^+$  diffusion within the n-well collection electrode) and also the fact that it allows to increase radiation tolerance to TID effects, which was one of the key working area in the upgrade of the sensor.

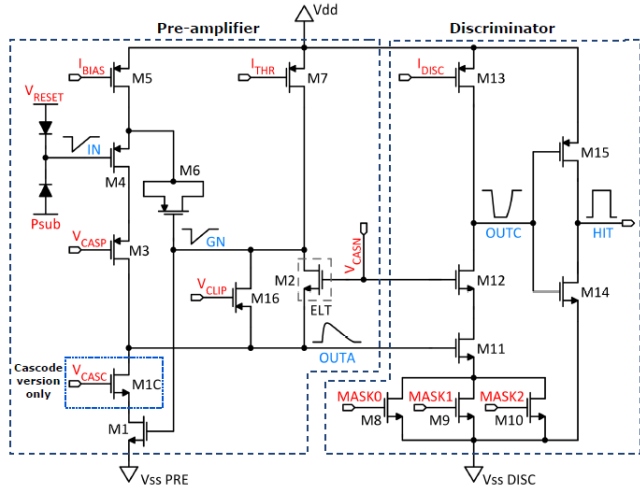


Figure 5.5: Schematic of the improved front-end circuit and its variation (extra-cascode transistor) in TJ-Monopix2.

In the last two AC-coupled flavors are implemented the same improvements, but here the different coupling provokes an important loss in the collected charge, as verified during the testing phase of TJ-Monopix1 (50% losses), due at most to additional parasitic capacitances. Thus a lot of efforts have been made to improve this aspect, working on the coupling capacitor values. A signal loss of 41.5% has been reached in TJ-Monopix2, which is a relevant enhancement with respect to its predecessor.

## 5.2 Threshold and noise

**Explain here what are NOISE, THR and THR dispersion, and why they are important figure of merit for the operation.**

see for example Eleonora's thesis sec 4.1.1.

To measure the threshold and noise of the whole matrix, the response of each pixel has been characterized by means of the internal charge injection.

### 5.2.1 Injection circuit

The hit injection circuit included in TJ-Monopix2 is similar to the one of TJ-Monopix1. It allows to produce artificial hits on each pixel through an injection capacitance  $C_{inj}$  connected at the collection electrode. The injected charge is proportional to the injection voltage pulse amplitude:  $Q_{inj} = C_{inj} \cdot \Delta V_{inj}$ . The injection pulse is set by two registers "V<sub>L</sub>" and "V<sub>H</sub>", with  $\Delta V_{inj} = V_H - V_L$ , and the minimum injection step is given by the DAC resolution, with the *Least Significant Bit (LSB)* = 7.03 mV.

The injected signal is then often expressed in DAC units  $Q_{inj}(DAC)$  and can be converted to electrons using the design value of the injection capacitance  $C_{inj} = 230 \text{ aF}$ , the same for the all the FEs implemented. The nominal conversion factor  $K$  from DAC to e- corresponds to the injected charge given by a voltage step of 1 DAC:

$$K = C_{inj} \cdot LSB = \frac{230 \text{ aF}}{q_{e^-}} \cdot 7.03 \frac{\text{mV}}{DAC} = 1.4375 \frac{e^-}{mV} \cdot 7.03 \frac{mV}{DAC} \approx 10.1 \frac{e^-}{DAC} \quad (5.1)$$

An absolute calibration of the conversion factor  $K$  (i.e. of the injection capacitance  $C_{inj}$ ) has been also performed using radioactive sources, as explained in section 5.4, obtaining results in agreement within 10% from the design value.

The conversion factor of equation 5.1 has been used to convert the information of the injected charge from DAC unit to electrons unit, useful for further analysis.

The response of each pixel to internal injection has been measured to extract their threshold and noise with the *s-curve method* explained in next section. The four flavors have been separately analyzed to be able to study their main differences concerning their performance and features.

### 5.2.2 S-Curve method

The response of the pixels is measured injecting different amounts of charge into the pixel a given number of times and recording the amount of registered hits (i.e. the signal is above the discriminator threshold). For each value of the input signal we measure the occupancy, or hit probability, as the fraction of events where the pixel has registered an hit. This occupancy has the typical S-curve shape shown in Figure 5.6 as an example.

As the injected signal passes the discriminator threshold the pixel starts to register some hits, finally reaching a plateau corresponding to the total number of injected events. This behaviour produces a step function smeared by the fluctuation on the input signal due to the noise. The threshold of the pixel corresponds to the injected signal that gives 50% occupancy, while the noise influences the slope of the S-curve.

Assuming a gaussian noise distribution the S-curve can be fit with the *Cumulative Distribution Function (CDF)*:

$$CDF(x, \mu, \sigma) = \frac{1}{2} \cdot \left( 1 + \operatorname{erf}\left(\frac{x - \mu}{\sigma\sqrt{2}}\right) \right) \quad (5.2)$$

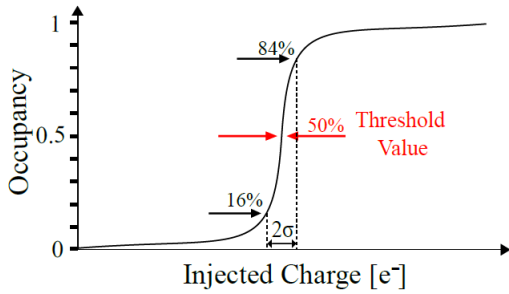


Figure 5.6: An example of the S-Curve fitted by the CDF to evaluate threshold and noise.

where "erf" is the Gauss error function,  $x$  is the injected signal,  $\mu$  and  $\sigma$  are respectively the threshold and noise of the pixel.

This method allows to measure the noise and the threshold of all pixels and also the threshold dispersion across an entire FE.

In the following sections are reported the results of this study for the four flavors of matrix. The injected signal was varied, with the corresponding voltage injection registers "**VL, VH**" , from 0 to 140 equation 5.1 .

#### 5.2.2.1 Normal FE

The first flavor of the matrix is the **Normal FE**, which consist of 512 rows and 224 columns for a total of 114.688 pixels. The chip registers have been set with the same values used during the Test Beam at Desy (July 2022) which are different for the DC and AC-coupling case. They are called for simplicity "**GOE settings**" and they are reported in Table 5.1, where the different biasing voltages used to power up the chip are also added.

Registers	Normal/Cascode FE ( $P_{SUB}/P_{WELL} = -3$ V)	HV/HV-Cascode FE ( $P_{SUB}/P_{WELL} = 0$ V, HV = +5 V)
$I_{THR}$	64	30
$I_{BIAS}$	50	60
$V_{RESET}$	143	100
$I_{CASN}$	0	8
$I_{DB}$	100	100
$I_{TUNE}$	53	53

Table 5.1: Settings of the main registers used for all flavors (W14R12 chip) during the Test Beam in Desy.

In Figure 5.7 are plotted all the s-curves of the all Normal flavor pixels. The width of the figure is a first indication of the threshold dispersion of the whole flavor.

The threshold and noise distributions measured on all pixels with the s-curve method, have been fitted with a gaussian distribution and they are shown in Figure 5.8 with their maps, too.

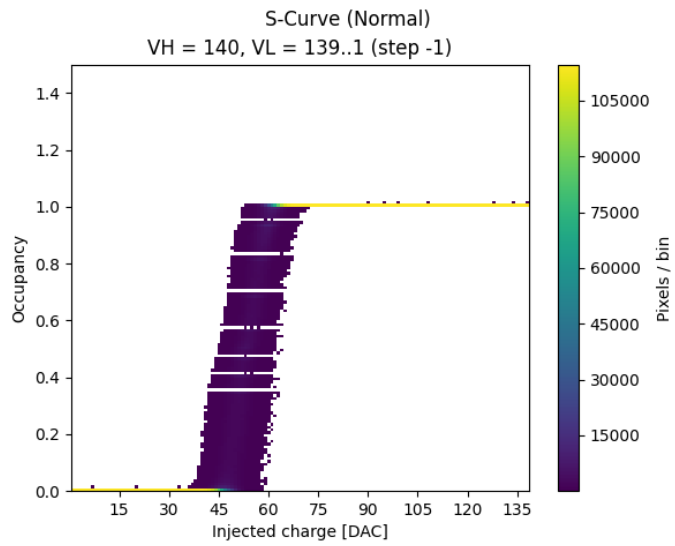


Figure 5.7: S-curves of all pixels of the Normal FE with a maximum injection pulse of 140 DAC.

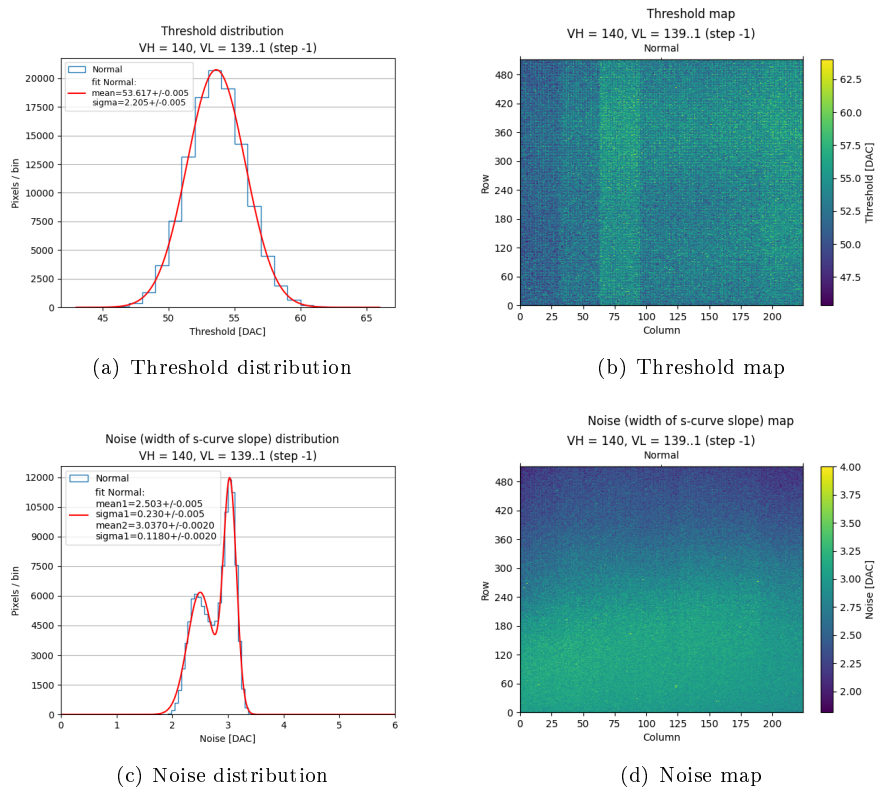


Figure 5.8: Normal FE.

### 5.2.2.2 Cascode FE

**Cascode FE** is the second flavor and like the previous one, it consists of 512 rows and 224 columns for a number of total pixels equal to 114.688. For this flavor the same procedure of Normal FE has been followed and also the same registers' values (Table 5.1) have been used. In Figure 5.9 the s-curves of all pixels are shown.

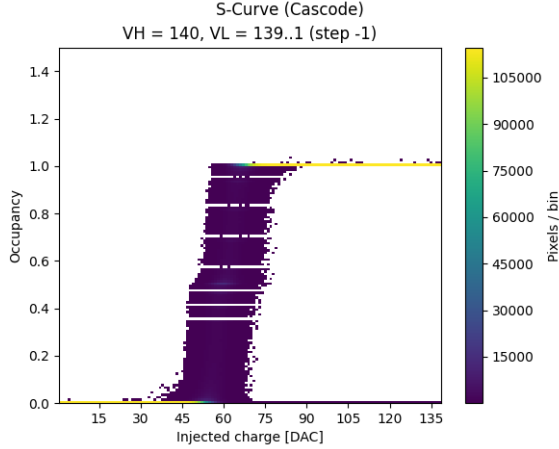


Figure 5.9: S-curves of all pixels in the **Cascode** flavor with a maximum injection pulse of 140 DAC.

The maps and the fit of the threshold and noise distributions instead, are shown in Figure 5.10.

### 5.2.2.3 HV-Cascode FE

The third flavor is **HV-Cascode FE** and it is composed by 512 rows and 32 columns for a total number of pixel equal to 16384. Also for these last two flavors, the main chip registers are set with the same values tested and used during the Test Beam (@Desy) (but different from those used for the first two flavors). They are reported in Table 5.1 .

As we can see from the plot of the alle s-curves in Figure 5.11, with this choice of registers there were a lot of "hot" pixels with occupancy  $> 1$ , but at this stage of measurements they were not masked. These hot pixels with occupancy  $> 1$ , register more hits than the number of injected events. This behaviour seems to indicate that they are stimulated, not by the charge injection, but by some other input, due to "cross-talk", active during the readout of the matrix. The origin of the hot pixel and cross-talk was carefully investigated later (see section 5.6) .

In Figure 5.12 are shown the fit of the threshold and noise distributions.

### 5.2.2.4 HV-Normal FE

The fourth and last flavor is the **HV-Normal FE** which has the same layout and so the same number of pixel of the previous FE. The main registers have been set with the values reported in Table 5.1. In Figure 5.13, the s-curves of all pixel in this flavor. Also here we can see that there were some hot pixels unmasked. Moreover the last 16 columns were not working (visible in the maps in Figure 5.15) and as a matter of fact they had return a peak of threshold near the value 0, which is excluded from the threshold distributions plots.

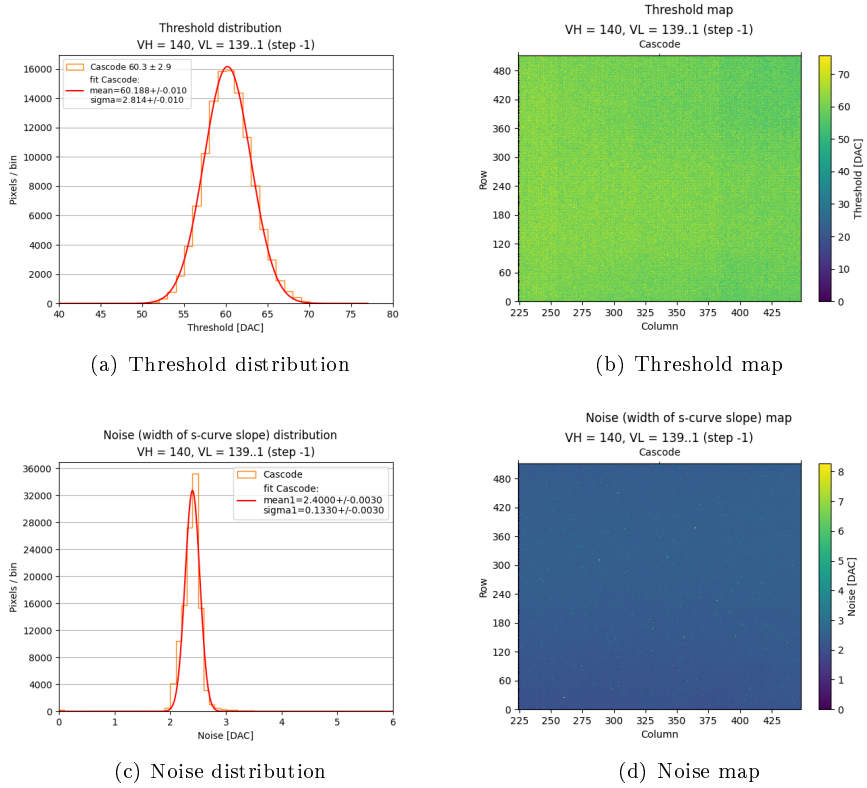


Figure 5.10: Cascode FE.

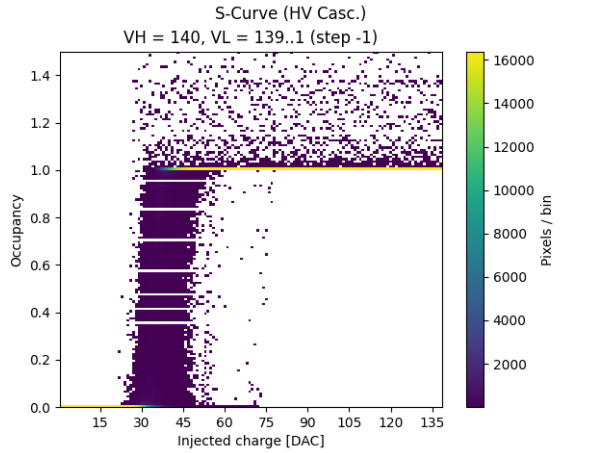


Figure 5.11: S-curves of all pixels in **HV Cascode** flavor with a maximum injection pulse of 140 DAC.

So actually in this part of the matrix, the real number of pixel studied was the half of the total, such as 8192 pixels.

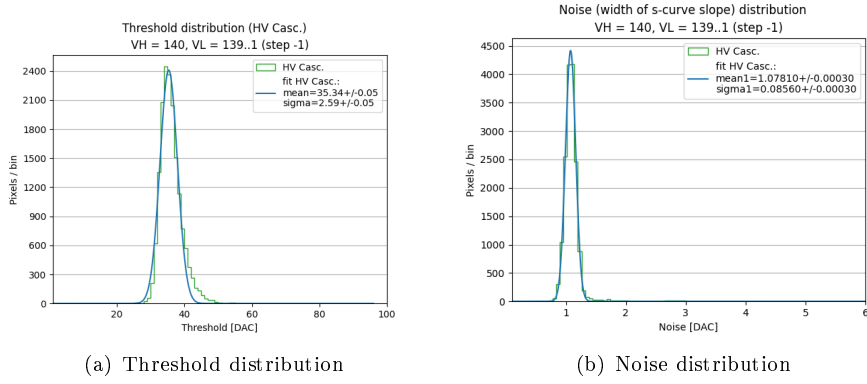


Figure 5.12: HV Cascode FE.

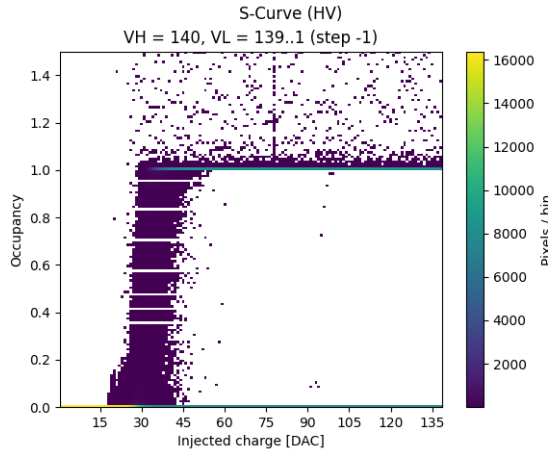


Figure 5.13: S-curves of all pixels in **HV Cascode FE** with an injection pulse of 140 DAC.

In Figure 5.14 the fit of the threshold and noise distributions.

At last, in Figure 5.15 the threshold and noise maps of the whole HV flavor.

As we will see in the following (section 5.6), the atypical s-curves in HVs flavors with many hot pixels, have been the first hint of the cross-talk problem, tied to a global lower threshold in these sectors, compared with the first two threshold measured in the Normal and Cascode sector (with the TB settings).

#### 5.2.2.5 Summary Table

In table on the following page a summary of results for threshold, noise and threshold dispersion of all FE.

#### 5.2.3 Threshold dispersion and tuning

TJ-Monopix2 is equipped with a circuit which allows the *threshold tuning*. We have already mentioned that the analog part of the in-pixel front-end (Figure 5.4) includes the 3-bit threshold

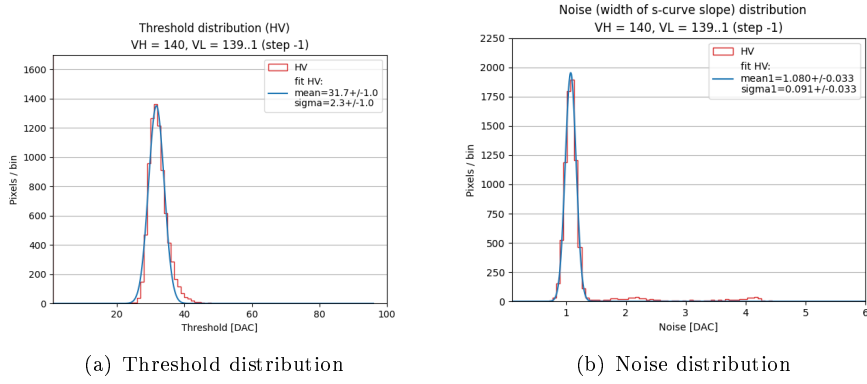


Figure 5.14: HV Normal FE.

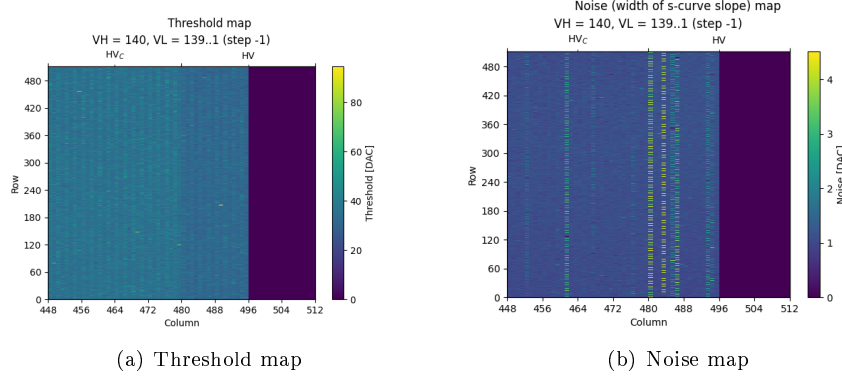


Figure 5.15: HV's FE.

Front-End	Threshold [ $e^-$ ]	Threshold dispersion [ $e^-$ ]	Noise [ $e^-$ ]
Normal	$53.62 \pm 0.01$	$2.21 \pm 0.01$	$2.503 \pm 0.005$
Cascode	$60.19 \pm 0.01$	$2.81 \pm 0.01$	$3.037 \pm 0.002$
HV - Cascode	$35.34 \pm 0.05$	$2.59 \pm 0.05$	$1.0781 \pm 0.0003$
HV	$31.70 \pm 0.10$	$2.30 \pm 0.10$	$1.080 \pm 0.033$

Table 5.2: Summary table of threshold and noise values for all flavors of the W14R12 chip.

tuning DAC, that can be used to adjust the discriminator threshold of each pixel with respect to the global chip threshold level thus reducing the threshold dispersion. In other words it can adjust every pixel threshold, in order to have a threshold on the matrix as uniform as possible, or in any case a dispersion as small as possible, which is especially important to operate the matrix with low threshold, needed with the reduced collection efficiency due to radiation damage. This system has been designed in order to counteract some negative effects that affect the threshold dispersion like systematics (for example related to biasing), process and temperature variations and radiation damage.

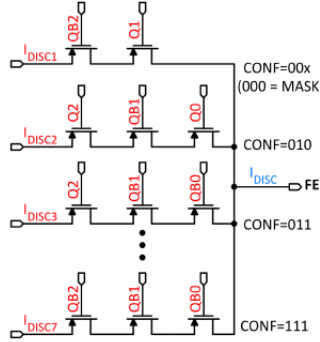


Figure 5.16: Schematic of 3-bit tuning DAC (TDAC)

Specifically the TDAC circuit, shown in Figure 5.16, helps to make threshold trimming of each pixel. This component controls the discriminator active load current  $I_{DISC}$  which is partially responsible of the pixel threshold. It works as an analog multiplexer (consisting of simple PMOS transistor switches), which selects one of seven  $I_{DISC,n}$  lines generated by the main 8-bit biasing DAC. So the possible value of the final  $I_{DISC}$  is given by the sum of two contributions:

$$I_{DISC} = I_{DISC,coarse} + (TCODE - 1) \cdot I_{DISC,fine}, \quad \text{where } 1 \leq TDAC \leq 7 \quad (5.3)$$

$I_{DISC,coarse}$  is the current set by the primary value of threshold, resulting by the setting of the main registers which are responsible for it (listed in ...).  $I_{DISC,fine}$  is the current selected by the fine tuning step (TDAC) and it depends on the 3-bit tuning code that is stored in the in-pixel tuning memory latch (the in-pixel configuration memory). **TCODE** is the decimal representation of the TDAC code.

For example if the 3-bit DAC are set to "111", the decimal representation is 8 and the fine tuning provide a current  $I_{DISC,7}$ , which corresponds to the highest threshold. If the 3-bit are set to "010" the corresponding TCODE is 2 and the current  $I_{DISC,1}$  is provided, which set the lowest threshold possible around the central value  $I_{DISC,coarse}$ . The particular combination "000" instead (TCODE = 0) masks the pixel by disabling the discriminator, without affecting the operation of the others.

### 5.2.3.1 First results from threshold tuning

It has been trying to apply the fine tuning method to level out the threshold of some pixels as much as possible. We have considered about 12.000 pixels of the **Cascode FE** and in Figure 5.17 are shown the results before and after the threshold trimming for the s-curves and threshold distributions.

As we can see the dispersion has been reduced of the 42% after the tuning and as consequence also the estimation of the threshold is more precise. In figure on page 68 are displayed the maps of the threshold and of the TDAC values, such as the value of TCODE assigned at each pixel, in order to obtain a threshold as uniform as possible.

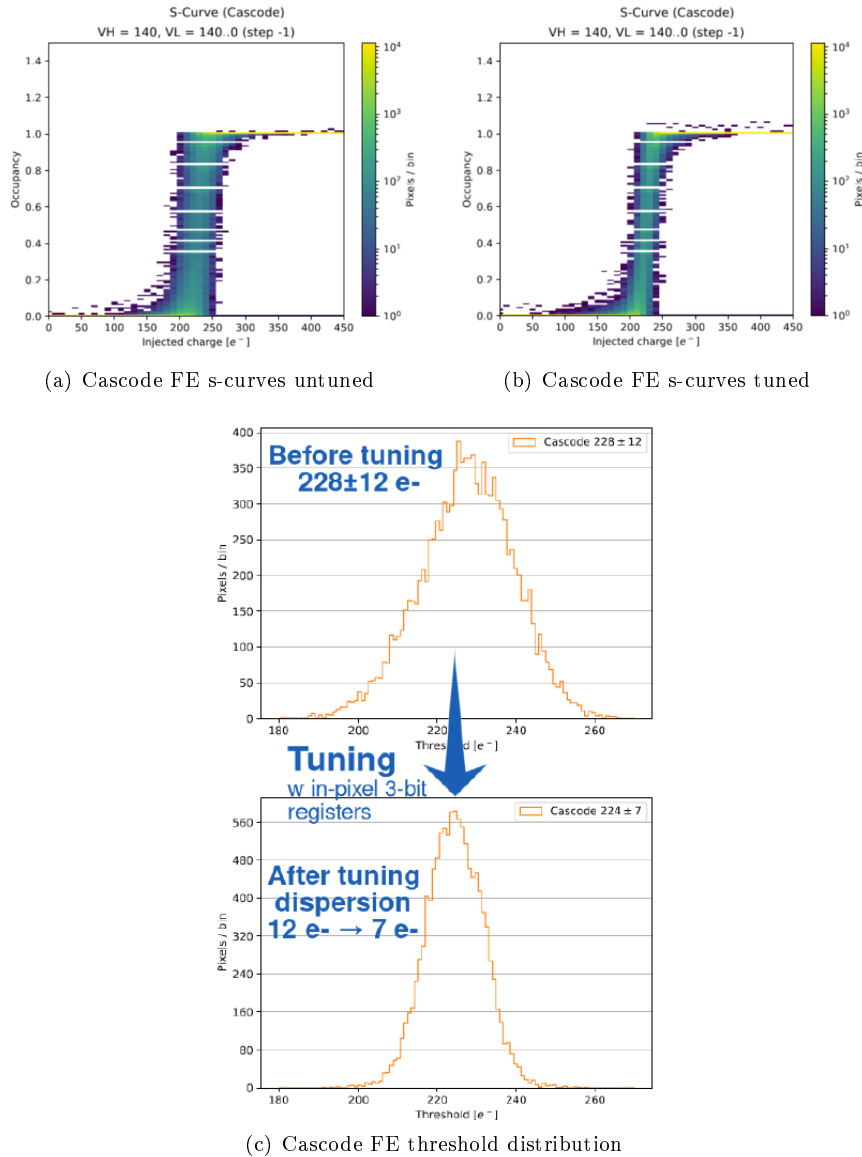


Figure 5.17: Cascode FE before tuning and after tuning comparison.

### 5.3 ToT calibration with internal injection

The analog information on the signal height is provided by the Time Over Threshold (Figure 5.19) digitized with a 25 ns clock (BCID clock-frequency is 40 MHz).

As it has been pointed out in the previous, the choice to use a simple diode instead of a PMOS transistor as reset input baseline element, increases the tolerance to TID radiation but at the same time it implicates a non-linear relationship between the injected charge and the ToT. For this reason, one of the goal of this analysis was to measure the calibration curve ToT vs

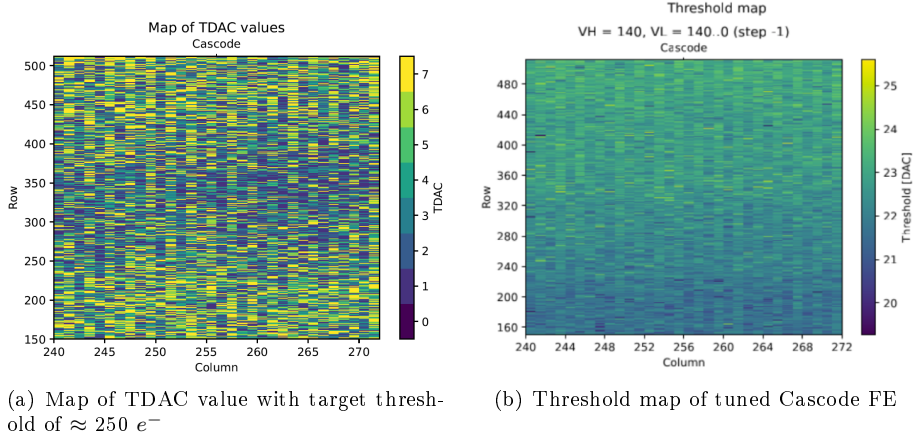


Figure 5.18: Maps of tuned Cascode FE.

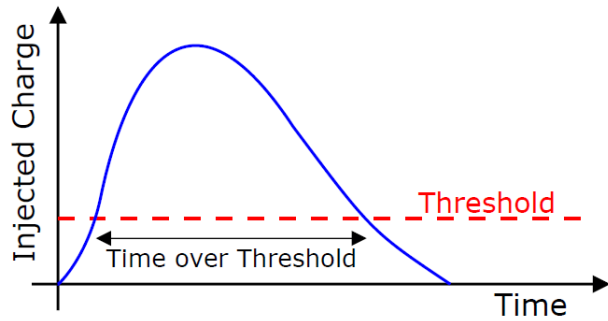


Figure 5.19: ...

$Q_{inj}$  via the internal injection. The fit to the calibration curve allows to find the conversion factor needed to reconstruct the signal amplitude. It also allows an absolute calibration of the injection capacitance comparing the results with the ToT response from the radioactive source with known released signal.

In carrying out the measurements mentioned above, we started to notice some issues with the injection circuit, which showed some saturation in the voltage pulse at high values of the registers. Due to this issue, the ToT response to internal injection could only be measured up to 170 DAC ( $\approx 1700 e^-$ ). This was enough for the absolute calibration using the  $^{55}\text{Fe}$  5.9 KeV line ( $\approx 1616 e^-$ ) as explained below.

A method has been therefore devised to obtain reliable values of threshold and ToT up to a value of 170 DAC of effective charge injected.

The calibration function adopted to describe the  $Q_{inj}$ -ToT relationship was then used to extrapolate ToT values in the region of high charge (above 170 DAC,  $\approx 1700 e^-$ ) not accessible with the injection circuit, to compare with the emission peaks of other radioactive sources and explore a larger range.

### 5.3.1 Time Over Threshold (TOT) curves and fit

The ToT vs  $Q_{inj}$  responses for the four flavors of the matrix (using the same TB register settings) are shown in Figure 5.20. The function chosen to describe the calibration curves is:

$$y(x) = a \cdot x + b - \frac{c}{x - t} \quad (5.4)$$

with  $a$ ,  $b$ ,  $c$  and  $t$  free parameters and where the  $y$  represents the ToT corresponding to a precise value of collected charge, express by  $x$ .

Actually we know that the ToT distribution starts to grow near the threshold, so one of the four free parameters could be computed in function of the threshold value estimated from the previous measurements reported in section 5.2.2.

In more details, knowing that  $y(x_{th})$  must be equal to 0 that is the ToT value at the threshold, it can be imposed for example:

$$0 = a \cdot x_{th} + b - \frac{c}{x_{th} - t} \Rightarrow c = x_{th}^2 \cdot a + x_{th} \cdot (b - a \cdot t) - t \cdot b \quad (5.5)$$

In this way the number of parameters to fit is reduced. In principle a similar equation could be equivalently solved for  $a$ ,  $b$  and  $t$ .

Thus different fits have been made: one imposing a constraint on a free parameter (like shown above) and the other one leaving all parameters free. For all of them the value of  $\chi^2$  (MSE) have been computed and for all flavors it had its minimum when no parameters were fixed. So in the following the results from these last fits with all the parameters left free, have been considered.

The same data collected in the previous measurements of thresholds have been used to fit the ToT curves of all pixels for each frontend. As a matter of fact we want to fully characterized the chip response with "GOE" settings (Table 5.1), in order to use the results to convert ToT to charge collected for the analysis of the TB data. In Table 5.3 are reported the results of the fits for all parameters.

	<b>Normal</b>	<b>Cascode</b>	<b>HV Cascode</b>	<b>HV</b>
$a \pm \Delta a$ [ $\frac{\text{ToT}}{\text{DAC}}$ ]	$0.12 \pm 0.07$	$0.12 \pm 0.01$	$0.257 \pm 0.007$	$0.275 \pm 0.008$
$b \pm \Delta b$ [ $\text{ToT}$ ]	$4 \pm 18$	$1.4 \pm 3.1$	$3.2 \pm 1.4$	$2.3 \pm 1.6$
$c \pm \Delta c$ [ $\text{ToT} \cdot \text{DAC}$ ]	$200 \pm 1100$	$140 \pm 130$	$160 \pm 70$	$140 \pm 80$
$t \pm \Delta t$ [ $\text{DAC}$ ]	$20 \pm 90$	$40 \pm 15$	$17 \pm 6$	$13 \pm 8$

Table 5.3: Parameters obtained from the fit of ToT curve for each frontend.

## 5.4 Response to radioactive source and absolute calibration

The absolute calibration of the matrix consists in characterizing the response of each pixel to a known signal, like the emission peaks of radioactive sources, then comparing the results with the response from the internal injection circuit to the same amount of charge. By the means of the  $Q_{inj}$  - ToT fit (section 5.3.1), it is possible to convert the ToT signal value to collected charge. Three different X-rays radioactive sources were used to study the signal spectrum of the matrix, with emission lines from 6 to 60 KeV (corresponding approximately to 1600 and 16000 e- respectively). In fact the knowledge of the sources emission spectrum (in other words, the charge released in the matrix from particles emitted in decays) allows to compare the spectra obtained irradiating the chip, with the expected value of their peaks. It is worth mentioning that only

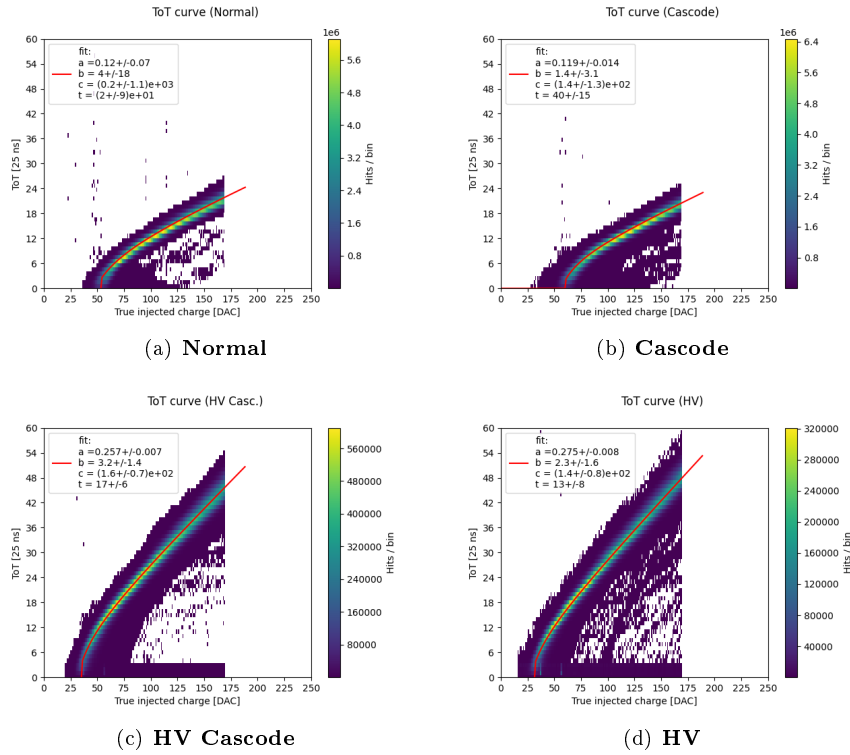


Figure 5.20: ToT curves fit for all frontend.

the events in which all charge induced is collected in a single pixel are part of the peaks reconstructed by the chip.

The absolute calibration of the conversion factor of equation 5.1 (i.e. of the injection capacitance  $C_{inj}$ ) is performed with the 5.9 KeV peak of the  $^{55}\text{Fe}$  source (*approx* 1616  $e^-$ ), that is still in the range explored with the injection circuit. The other radioactive sources allowed to extend the ToT comparison at higher values with respect to the limit imposed by the saturation of the internal injection circuit. In Table 5.4 are shown the energies of the  $\gamma$  emitted by the sources used.

Considering that the average energy necessary to produce an electron/hole pair in silicon is 3.65 eV, it is possible to convert the peak energies in a mean value of electrons released using the equation 5.6. So in Table 5.4 are reported also the equivalent emission in electrons, which will be useful later.

$$N_{e^-} = \frac{E [eV]}{3.65 \left[ \frac{eV}{e/h \text{ pair}} \right]} \quad (5.6)$$

Now we can go through the results obtained from three different sources:  $^{55}\text{Fe}$ ,  $^{241}\text{Am}$  and  $^{109}\text{Cd}$ .

Source	Energy $\gamma$ [KeV]	Equivalent charge [ $e^-$ ]
$^{55}\text{Fe}$	5.9	1616
$^{241}\text{Am}$	13.9	3808
$^{241}\text{Am}$	17.7	4849
$^{241}\text{Am}$	20.7	5671
$^{109}\text{Cd}$	22	6027
$^{241}\text{Am}$	26.4	7233
$^{241}\text{Am}$	59.7	16356

Table 5.4: Emission lines of  $^{55}\text{Fe}$ ,  $^{241}\text{Am}$ ,  $^{109}\text{Cd}$  sources visible by the sensor.

#### 5.4.1 $^{55}\text{Fe}$

The  $^{55}\text{Fe}$  source decays by **electron capture** to  $^{55}\text{Mn}$ . One of the photons emitted in this transition has an energy of 5.9 KeV ( $K_\alpha$ ) and it produces via photoelectric effect an electron, which deposits a ionization charge of about 1616  $e^-$  in the sensor. All flavors were exposed to a  $^{55}\text{Fe}$  source, with activity of 18 MBq. In Figure 5.21 are shown the results for the ToT spectrum of single pixels. The peak corresponds to events where the  $\gamma$  interacts close to the collection diode and the entire signal is on a single pixel. The shoulder at smaller ToT is due to the charge sharing among several pixels, since no clusters are reconstructed. The peak was fitted by a gaussian function, limited in the region of the peak itself.

As it can be seen for the HV's FE a cut has been applied at low ToT, only to make clearly visible the emission line, since a lot of noisy pixels caused a sharp peak at 0 ToT. In those flavors there were several columns of not-functioning pixels. In the box of each plot are also reported the results of the fit that will be crucial in the following.

#### 5.4.2 $^{241}\text{Am}$

The  $^{241}\text{Am}$  source has a more complex spectrum (Figure 5.22) and not all its peaks can be detected by the chip (because of the limited range of ToT available, depending on the number of bits dedicated to it). The spectrum shows other minor peaks besides the usual intense gamma peaks (59.5 and 26.3 keV) and several characteristic L X-rays from  $^{237}\text{Np}$  (20.7, 17.7 and 13.9 keV).

The ToT measured spectra with the  $^{241}\text{Am}$  source on the four flavors are reported in Figure 5.23. Two peaks at lower energy are clearly visible while, for higher ToT values there are larger structures.

In the case of the first two flavors, it could be possible to fit four peaks of the emission lines. In case of the HV's flavors instead, only three peaks for the HV-Cascode FE and two for the HV. As already discussed (subsubsection 5.1.2.1) the AC-coupling causes about 41.5% of signal loss, so they are much less evident and more difficult to fit as isolated peak.

#### 5.4.3 $^{109}\text{Cd}$

The third source employed was the  $^{109}\text{Cd}$ . This isotope decays in  $^{109}\text{Ag}$  by electronic capture, producing a photon of 22 KeV in the transition. The ToT measured spectra with  $^{109}\text{Cd}$  source on the four flavors of the matrix are reported in Figure 5.24.

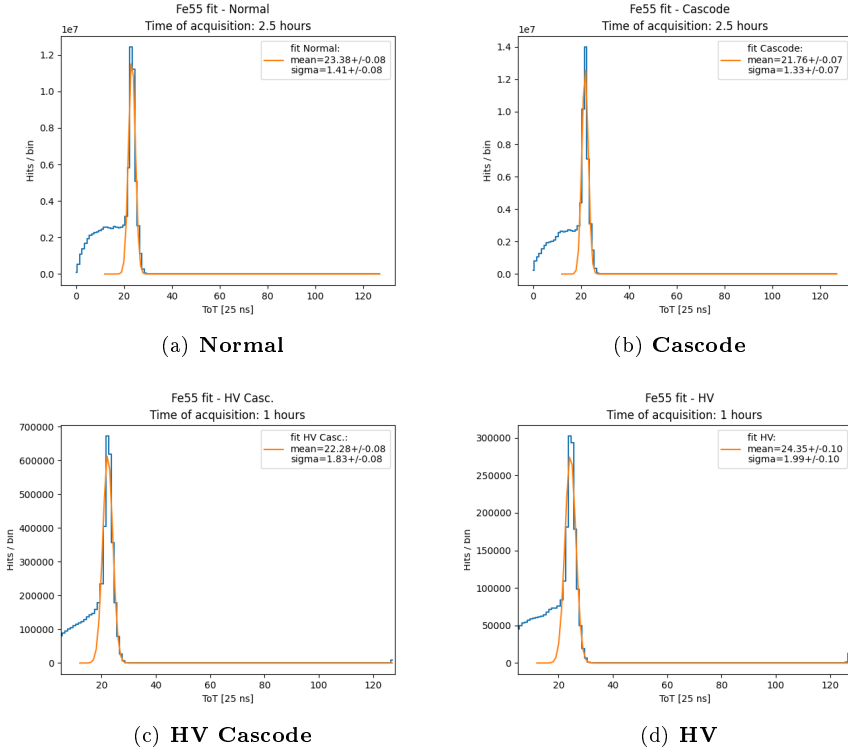


Figure 5.21:  $^{55}\text{Fe}$  peaks for all frontends.

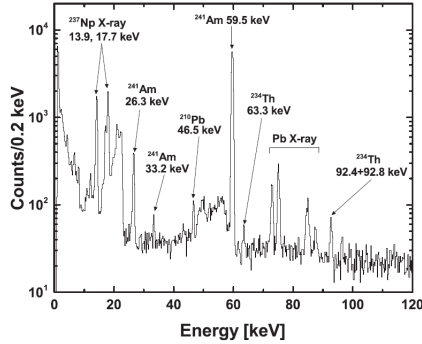


Figure 5. Gamma-ray spectrum of the  $^{241}\text{Am}$  source.

Figure 5.22:  $^{241}\text{Am}$   $\gamma$  emission spectrum.

#### 5.4.4 Injection capacitance calibration

The absolute calibration of the conversion factor  $K$ :

$$K = \frac{C_{inj}}{q_{e^-}} \cdot \Delta V_{LSB} \quad (5.7)$$

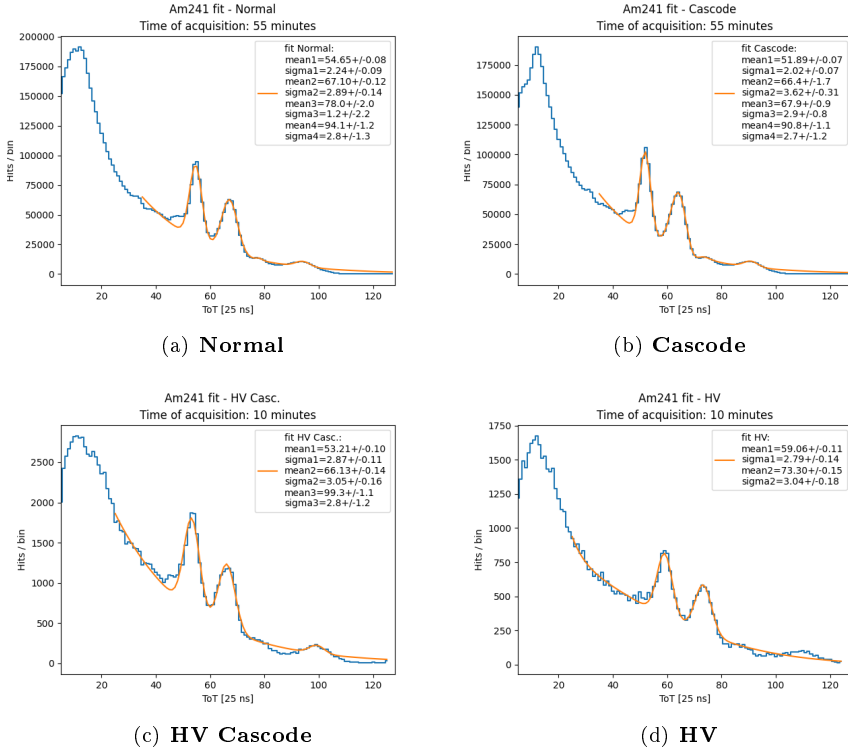


Figure 5.23:  $^{241}\text{Am}$  peaks for all frontends.

and of the injection capacitance:

$$C_{inj} = K \left( \frac{e^-}{DAC} \right) \cdot \frac{1.6 \times 10^{-19} \frac{\text{C}}{e^-}}{7.03 \frac{\text{mV}}{\text{DAC}}} \quad (5.8)$$

that convert a signal charge expressed in DAC units to  $e^-$ , is performed using the data from the  $^{55}\text{Fe}$  source.

As first step the ToT of the peak of the 5.9 KeV  $\gamma$  line is converted to signal charge in DAC using the fitted calibration curve of equation 5.4

Specifically the fit function was inverted obtaining:

$$x(y) = \left( \frac{t}{2} - \frac{b}{2a} + \frac{y}{2a} \right) \pm \sqrt{\left( \frac{t}{2} + \frac{b}{2a} - \frac{y}{2a} \right)^2 + \frac{c}{a}} \quad (5.9)$$

where  $x$  represents the charge in DAC corresponding to the ToT labeled by  $y$ .

As shown in Table 5.4, the charge released in the sensor by the 5.9 KeV  $\gamma$  corresponds roughly to  $Q_{5.9\text{ KeV}}(e^-) = 1616 e^-$ . Therefore the conversion factor  $K$  for each pixel can be calculated as:

$$K \left[ \frac{e^-}{DAC} \right] = \frac{1616 e^-}{Q_{5.9\text{ KeV}}[\text{DAC}]} \quad (5.10)$$

By these steps, a value of the conversion factor was estimated for each well-functioning pixel.

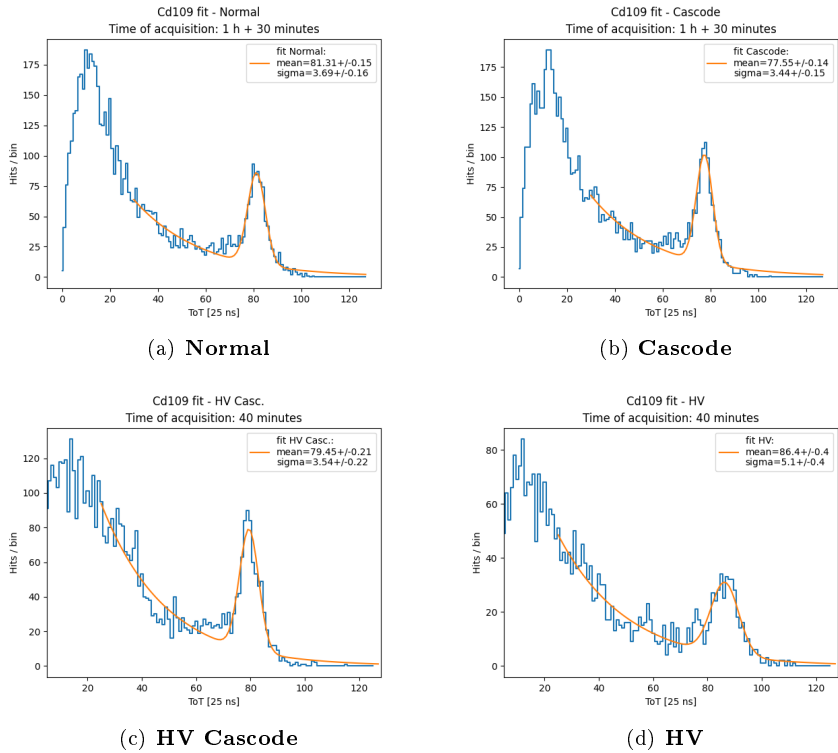


Figure 5.24:  $^{109}\text{Cd}$  pekas for all frontends.

In Figure 5.25 is reported the distributions of the conversion factor estimated, fitted by a gaussian function.

Source peak	$K_{Normal}$ ( $\frac{e^-}{DAC}$ )	$K_{Cascode}$ ( $\frac{e^-}{DAC}$ )
$^{55}\text{Fe}$ (5.9 KeV)	9.37	9.00

Table 5.5: Estimation of injection capacitance of Normal and Cascode flavors using the  $^{55}\text{Fe}$  radioactive source emission line at 5.9 KeV.

????????????? Here it is necessary to point out that for iron source more statistics were collected so in this case a complete analysis of each pixel has been done. For the other sources instead, there weren't enough statistics on every pixel so the injection capacitance has been estimate only as a mean value for the whole front-end, just to compare with the results obtained from the iron analysis. In case of  $^{55}\text{Fe}$  source, we managed to fit the emission peak for each working pixel of the whole matrix.

?????????????????

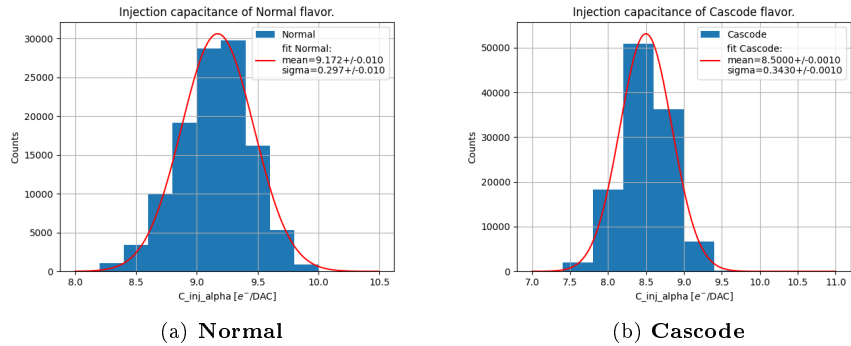


Figure 5.25: Injection capacitance distributions of Normal and Cascode FE.

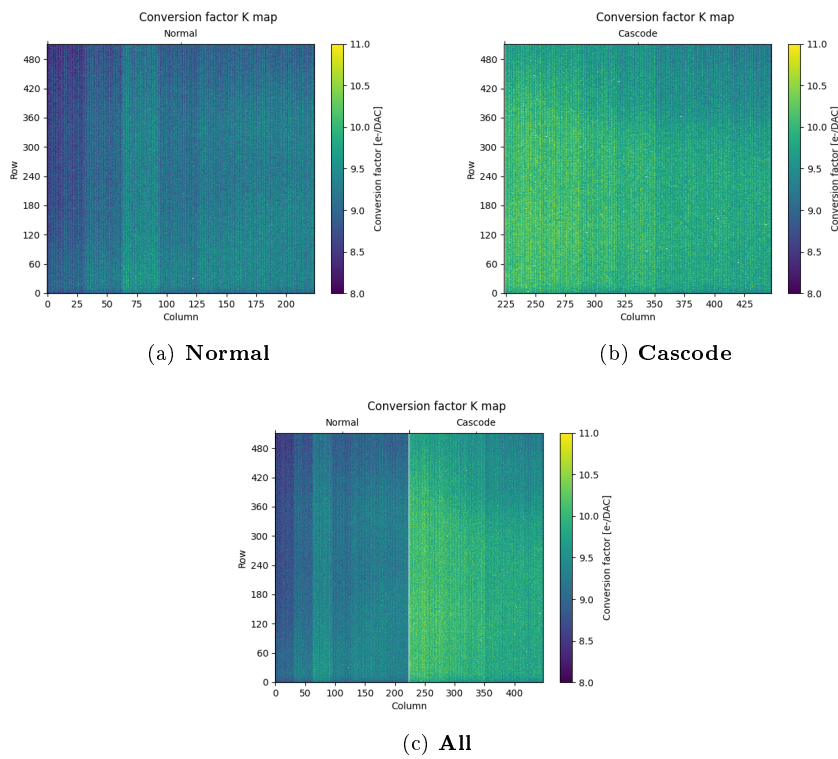


Figure 5.26: ???

#### 5.4.5 Check on calibration curve ToT vs $Q_{inj}$ with radioactive sources

The calibration of the ToT vs  $Q_{inj}$ (DAC) with the injection circuit could be performed only up to  $\approx 170$  DAC. The radioactive sources can be used up to higher energy to check the agreement with the fitted function in equation 5.4 .

Initially the signal charge in DAC corresponding to each  $\gamma$  peak, has been calculated using the nominal conversion factor equal to  $10.1 \frac{e^-}{DAC}$ . As it could be seen from results in Figure 5.27 there is a reasonable agreement between data and ToT relationship studied in section 5.3.1.

After the absolute calibration, assuming the average value of the conversion factor  $K$  (*Mean value*) measured with  $^{55}\text{Fe}$ , the charge in DAC corresponding to the emission peaks have been recalculated and results are shown in Figure 5.28.

In Table 5.6 and in Table 5.7 ....(descrizione, specifica quale K usi, richiama tabella?)

Source	Energy $\gamma$ [KeV]	$Q_{expected} [e^-]$	$ToT_{measured}$	$Q_{measured} [DAC]$	$Q [e^-]$ with nominal K factor = $10.1 e^-/\text{DAC}$	$Q [e^-]$ with $^{55}\text{Fe}$ K factor = $9.37 e^-/\text{DAC}$
$^{55}\text{Fe}$	5.9	1616	23.4	172	1742	1616
$^{241}\text{Am}$	13.9	3808	54.7	426	4304	3993
$^{241}\text{Am}$	17.7	4849	67.1	529	5344	4958
$^{241}\text{Am}$	20.7	5671	78.0	619	6256	5804
$^{109}\text{Cd}$	22	6027	81.3	647	6534	6062
$^{241}\text{Am}$	26.4	7233	94.1	753	7606	7057

Table 5.6: Emission lines of  $^{55}\text{Fe}$ ,  $^{241}\text{Am}$ ,  $^{109}\text{Cd}$  sources for Normal frontend.

Source	Energy $\gamma$ [KeV]	$Q_{expected} [e^-]$	$ToT_{measured}$	$Q_{measured} [DAC]$	$Q [e^-]$ with nominal K factor = $10.1 e^-/\text{DAC}$	$Q [e^-]$ with $^{55}\text{Fe}$ K factor = $9.00 e^-/\text{DAC}$
$^{55}\text{Fe}$	5.9	1616	21.8	180	1813	1616
$^{241}\text{Am}$	13.9	3808	51.9	427	4316	3846
$^{241}\text{Am}$	17.7	4849	66.4	549	5540	4937
$^{241}\text{Am}$	20.7	5671	67.9	561	5667	5050
$^{109}\text{Cd}$	22	6027	77.6	642	6483	5777
$^{241}\text{Am}$	26.4	7233	90.8	753	7604	6776

Table 5.7: Emission lines of  $^{55}\text{Fe}$ ,  $^{241}\text{Am}$ ,  $^{109}\text{Cd}$  sources for Cascode frontend.

As we can see, a better agreement is therefore obtained and this shows that through calibration we are now able to interpret data with greater precision, which was the main purpose of this analysis.

#### 5.5 Operation with low threshold

One of the most important target in sensor design is to keep high efficiency even after irradiation damages. All experimental environments indeed, are exposed to high doses of radiations, so it's

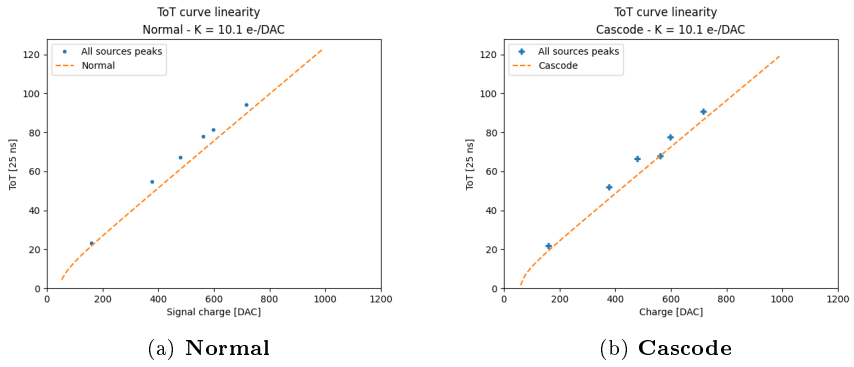


Figure 5.27: ToT of all flavors assuming the nominal(expected) conversion factor equal to 10.1  $\frac{e^-}{DAC}$ .

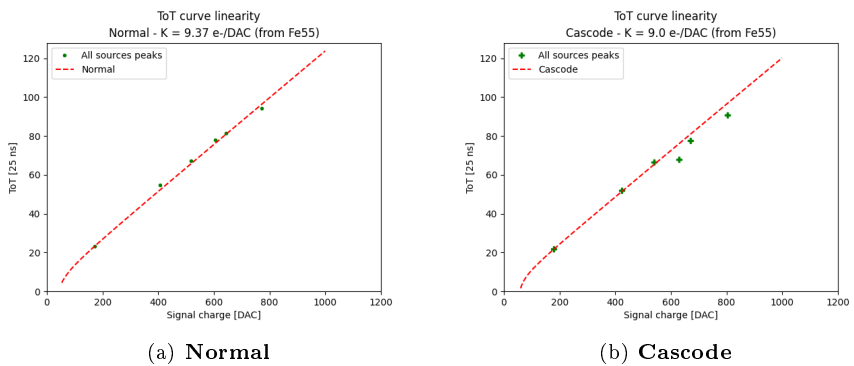


Figure 5.28: ToT linearity of all flavors assuming the conversion factor obtained from  $^{55}\text{Fe}$ .

crucial to ensure the functionality of the detectors, even after being irradiated.

For this reason, many tests were done in order to understand the chip behaviour at low threshold where a good value of efficiency could be preserved. Moreover working at low threshold allows to detect low charge events due to charge sharing or charge trapping (effect which increases after irradiation), especially in case of thin epitaxial material.

### 5.5.1 Register optimization

As we have seen in section (REFERENCE), there are a lot of registers which control the discriminator threshold and also the readout sequence. So preliminary it was necessary to explore their possible settings in order to operate the chip at low threshold.

Now we will go through the main registers used for this purpose, in order to explain their functionality. There are several dozens of registers but we focused on some of the most important and crucial to set the threshold and its dispersion.

- $I_{CASN}$  : this current is responsible of the output baseline signal. In particular it sets the baseline of the FE output that goes to the input discriminator. In a few words, higher this

value, higher the baseline, lower the threshold and also a little bit the gain and vice versa by decreasing it.

- $I_{THR}$ : it controls the pre-amplifier feedback strength and speed, so it is responsible for the output reset rate. Increasing this current increases the gain and the time that the analog output takes to get back to the baseline and as consequence, it increases a lot the maximum value of the ToT. In fact it is recommended to set  $I_{THR}$  to low value (e.g. 8 nA[ref]) in order to avoid high ToT slope.
- $I_{DB}$ : this current corresponds to  $I_{DISC,coarse}$  explained in section ?? on page ???. It represents the primary current that sets the discriminator threshold, to which another current is added by the tuning.
- $I_{TUNE}$ : it corresponds to  $I_{DISC,fine}$  instead (always section on page ??). Remembering the equation from tuning<sup>1</sup> (on page ??), this is the current to multiply by the TDAC value, which is added to  $I_{DB}$ , during the tuning process.
- $I_{BIAS}$ : this current acts on the pre-amplifier input transistor and influences the threshold dispersion and the gain. In particular increasing this value, the dispersion decreases and the gain becomes greater. Nevertheless it can't be increased a lot because it affects the power consumption, too.

### 5.5.2 Comparison between data and simulation

In the interest of understanding how the registers' setting of the chip influences the threshold, several measurements have been taken with different configuration of their values. The results are compared with simulations done by Hung Pham. (...). [??]

$I_{CASN}$

In figure 5.29, we can see the simulated behaviour of the threshold and the gain, increasing the value of  $I_{CASN}$ .



Figure 5.29: Trends of Gain and Threshold increasing  $I_{CASN}$ .

To verify the trend of threshold as this current varies, three different acquisitions have been taken by fixing  $I_{THR} = 20, 40, 64$  and increasing  $I_{CASN}$  from 0 to 30 DAC, with a step of 5

<sup>1</sup>

$I_{DISC} = I_{DISC,coarse} + (TCODE - 1) \cdot I_{DISC,fine}, \quad \text{where} \quad 1 \leq TDAC \leq 7 \quad (5.11)$

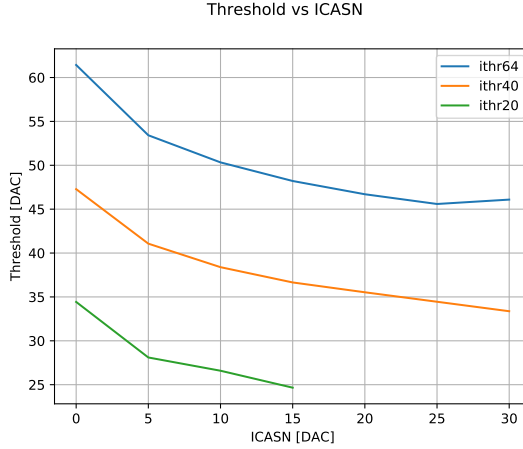


Figure 5.30: Threshold vs.  $I_{CASN}$  for  $I_{THR}=20, 40, 64$ .

DAC. We have done this enabling 200 pixels in the Cascode FE (rows: 472 - 512, cols: 225 - 230).[??]

Each threshold distribution has been fitted with a gaussian function in order to estimate the average threshold value and its dispersion.

In figure 5.30 are reported all trends obtained.

$I_{THR}$

Reusing the same data of the previous measurements, the trend of the threshold have been studied by changing the value of  $I_{THR}$  and fixing that of  $I_{CASN}$ . In this case only  $I_{CASN}$  from 0 to 15 DAC is considered, because for higher values we don't have enough measures of the threshold (specifically only two for  $I_{THR}=40, 64$ ). The results are shown in figure 5.31.

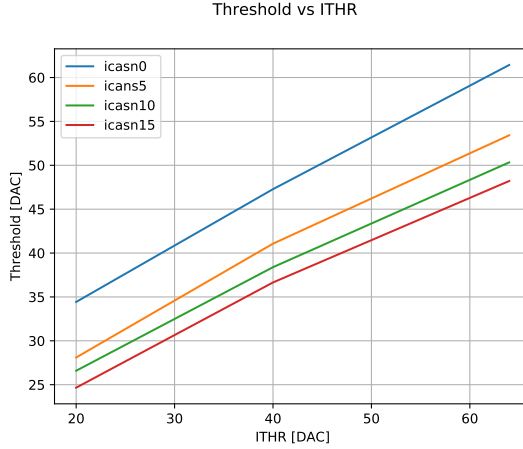


Figure 5.31: Threshold vs.  $I_{THR}$  for  $I_{CASN}=0, 5, 10, 15$ .

As expected, increasing  $I_{THR}$  results to lower gain and faster return to baseline, so higher threshold. We can compare them with the simulation shown in figure 5.32.

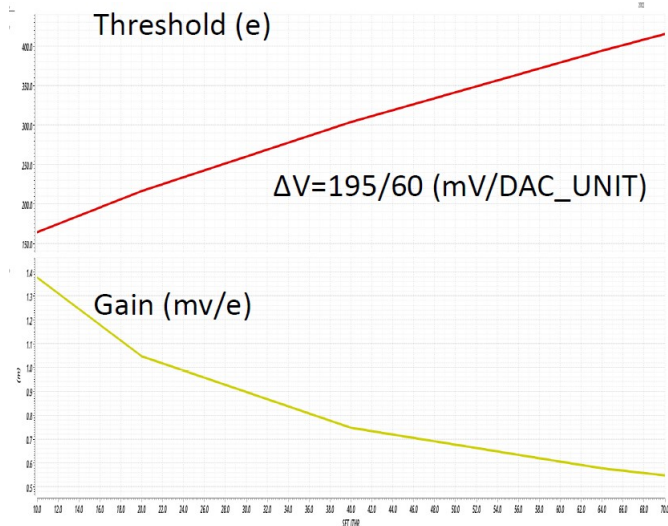


Figure 5.32: Trends of Gain and Threshold increasing  $I_{CASN}$ .

### Time over Threshold (ToT)

The last analysis done to make a comparison with the simulations, is about the trend of the ToT changing the value of  $I_{CASN}$  for a fixed value of  $I_{THR}$  and vice versa. In particular we consider the data obtained with  $I_{CASN}$  fixed to 0 DAC and  $I_{THR}$  to 64 DAC, which are the values studied and used for these registers during the Test Beam in Desy.

Results are reported in figure on the next page and on page 82. Also here we can see a good agreement between data and simulations.

#### 5.5.2.1 some nice picture of the optimized thr and tuning

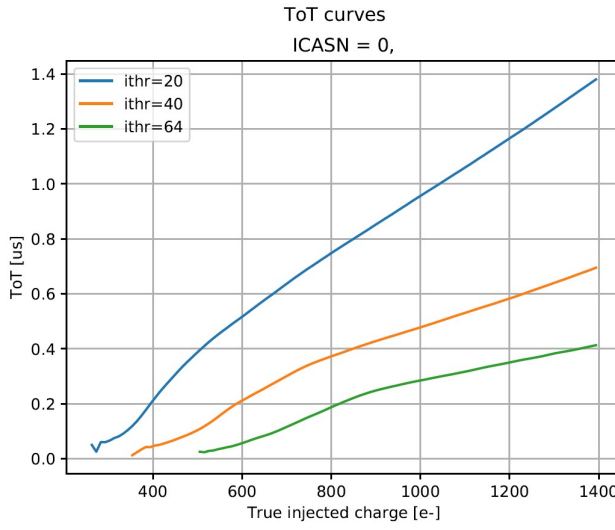
!!!!

## 5.6 Cross talk issue and mitigation

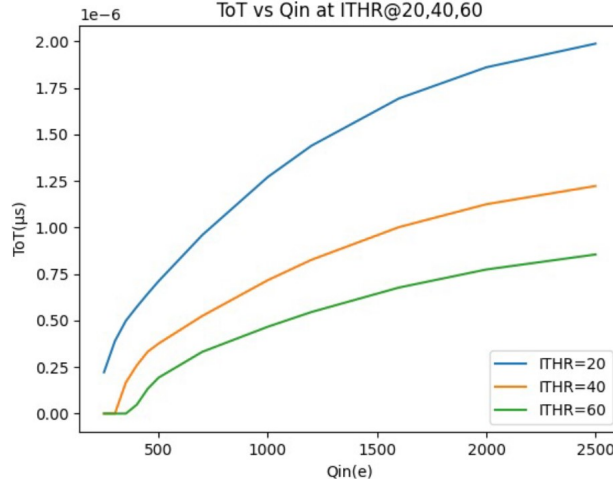
As it was already pointed out, during the measurements of the average threshold of all FEs, there were something atypical in the s-curves of the HV flavors (subsection ?? on page ??), indeed some pixels seem to have occupancy greater than 1. This behavior threatens the good functionality of the overall matrix response, because these *noisy pixels* flood the readout, giving unreliable results.

Also the systematic study of different register configurations has revealed the presence of the hot pixels which prevent to use certain settings and as consequence to reach lower global thresholds.

For this reason an investigation has been conducted in order to understand the reasons why they start to fire and how to cure them as far as possible. In the meantime an important issue



(a) ToT vs  $I_{THR}$  ( $I_{CASN}=0$  DAC) - Data (**Cascode**)



(b) ToT vs  $I_{THR}$  ( $I_{CASN}=0$  DAC) - Simulation

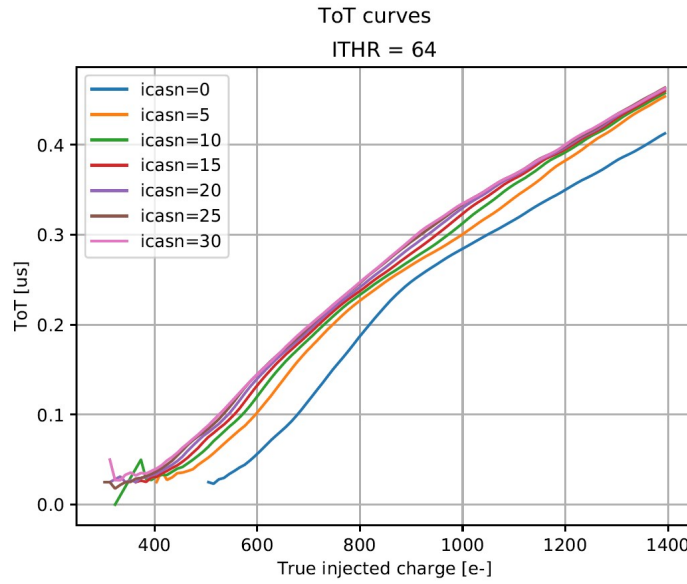
Figure 5.33: ToT vs  $I_{THR}$

with cross-talk of the readout signals was discovered, and so in this section we examine this effect and some attempts to mitigate it using different settings/bias.

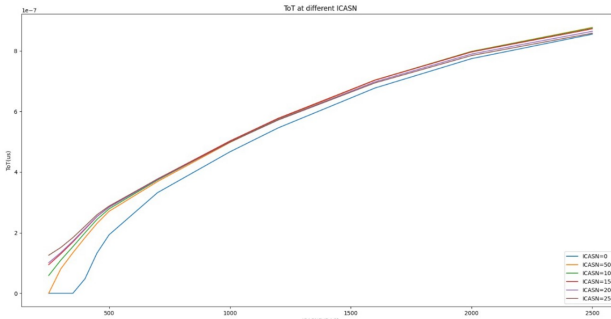
### 5.6.1 Hot pixel issue

First of all we noticed that in the s-curves oh the HV flavors (e.g. that of HV-Cascode reported in figure on page 83), the atypical behavior could be triggered by a digital signal sent to the matrix during the readout activity at low threshold. This consideration is based on two main reasons:

- when the matrix has high threshold, like for Normal and Cascode FE, all pixels seem to



(a) ToT vs  $I_{CASN}$  ( $I_{THR}=64$  DAC) - Data (Cascode)



(b) ToT vs  $I_{CASN}$  ( $I_{THR}=64$  DAC) - Simulation

Figure 5.34: ToT vs  $I_{CASN}$

behave as expected, without *hot pixels*.

Lowering the threshold and running some source acquisitions without any source, no strange behaviour was observed. Acquiring data with a radioactive source instead, even Normal and Cascode FE seem to reveal the same problem. This led to thinking that during the readout of good pixels an induced signal is created which couples with some other pixels, in particular with those at lower threshold with respect to the average value. If the height of this signal exceeds the threshold of the single pixel, it causes some spurious hits, making the pixel "hot".

- Moreover, always considering the HV Cascode s-curves, it could be noticed that in the region before the threshold ( $Q_{inj} < \text{threshold}$ , pointed by the blue arrow) there isn't an anomalous activity which means that the induced signal is not due to the BCID tha is always sent to the matrix during the injection or an acquisition with the source, regardless of being above or below the threshold. The atypical behaviour indeed, is in the region

above the threshold ( $Q_{inj} >$ threshold, pointed by the red arrow) where the occupancy of some pixels becomes greater than 1. This means that these *hot pixels* detect more hits of those injected.

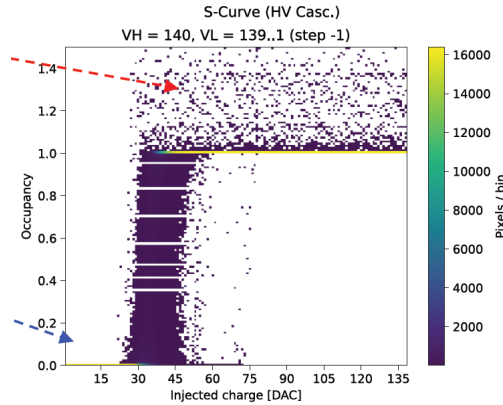


Figure 5.35: HV-Cascode s-curves.

From these first observations, we have reached the conclusion that the cross talk could be tied to the readout activity. So we have started investigating the timestamp of those hits not synchronize with the timestamp of the injection.

### 5.6.2 Hot pixel strategy (study)

At first, it has been lowered the threshold in order to "create" hot pixel also in the first two flavors of the matrix. In fact with TB settings the threshold was too high and the hypothetical induced signal did not cause spurious hits. For this purpose different settings were tried, changing some fundamental registers responsible for the threshold like those listed and explained on page 77.

Then several tests have been run under controlled conditions:

- one healthy(good) pixel was injected;
- one *hot pixel* (two or three in different tests) was enabled but not injected;
- the all matrix except these pixels was disabled.

In this way (remembering the readout sequence [REFERENCE]) the readout cycle has a known duration and two different timing info has been used to study the induced signal with greater precision:

- $\Delta TS$  (TimeStamp) between two consecutive hits: the TimeStamp is assigned from the FPGA when the TOKEN rises on the TE of the first hit to read, but only if the previous readout frame is completed. So, if the hit coming from a *hot pixel* is after the hit from the injected one, the minimum  $\Delta TS$  has to be equal to the readout time of 1 pixel and so to the duration of the FREEZE\_STOP signal .

This info has allowed to verify if the hot pixel fires after the good injected one or not.

- LE(hit) - TE(previous hit): this quantity measures the elapsed time between a hit and the previous one. This is a finer info than the  $\Delta TS$  because it allows to correlate the hit with the induced digital signal, originate from the readout cycle.

Moreover, since a 7-bit BCID is sent to the matrix during its activity, it was important to keep short ( $< 128$  clock cycle) the duration of the full readout sequence and to not enable too many pixels in order to not extend too much the readout frame. Otherwise the information on the leading edge of the pixel could not be correlated with the token of the previous hit. In other words, if the readout frame exceed 128 clock cycles, since the token could be raised if the matrix is **not** freeze, even if an hit is arrived before it could be read only in the next frame when it could rise again the token, but in this case it will have different TimeStamp. So in this case the TS is useless for our purpose.

### 5.6.3 Cross-talk (Results)

Referring to the readout sequence, in order to understand which signal could induce cross talk, each register value has been moved one by one. In table on this page just an example from the several settings tried is reported.

Register	Value
FREEZE_START_CONF	10
READ_START_CONF	13
READ_STOP_CONF	15
LOAD_CONF	30
FREEZE_STOP_CONF	31
STOP_CONF	31

Table 5.8: Register values of the Readout cycle.

Doing so indeed, the LE-TE info has to shift by the same value with which the signal that cause the cross talk has been changed. This step of the procedure is tied with the necessity to keep the readout sequence within the maximum 128 BCID range.

For example, if FREEZE\_START\_CONF is responsible for the cross talk signal, we expect that shifting its value by a certain amount, the hot pixels start to fire after that this signal arises due to the hit on the injected pixel. So the value of LE-TE has to be FREEZE\_START\_CONF + some potential delay. Same argument for the other registers.

By this procedure, repeated for each readout register, we have come to the conclusion that the cross-talk could be related to the raising and falling edge of the FREEZE signal.

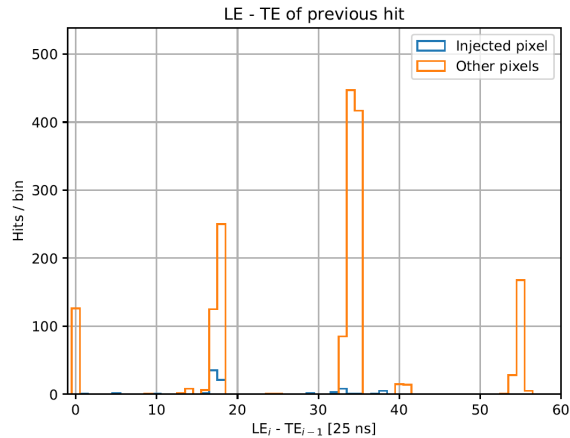
In figure on the next page an example of some results obtained. It is the histogram of the time last between the leading edge of an hit and the trailing edge of the previous hit, when one pixel is injected and two are read. It's possible to see several peaks (referring to the readout setting reported in table on this page):

- one at 0, that represent the situation in which both hits come from hot pixel firing simultaneously after the injection. This means that they are activated by the same signal and so it is the most important confirmation that is cross-talk and not random firing pixel signal;
- one at  $\approx 18$  equal to FREEZE STAR raising + 8  $\rightarrow$  first induced signal;

- one at  $\approx 35$  equal to FREEZE STOP falling + 4  $\rightarrow$  second induced signal;
- one at  $\approx 55$  equal to FREEZE STOP falling + 4 when two different pixels are read. In more details, after the first 30 time unit until the first LOAD CONF, a distinct pixel reading starts and it takes another 20 time unit (LOAD - FREEZE START) + 1 unit time to conclude the frame with the FREEZE STOP and so 51 + 4 unit time wrote above. Therefore when two pixels are read, the FREEZE STOP falls after 51 clock cycles, and it is compatible with the last peak in the plot.

Injected pixel: (217, 140) Other pixels: [(218, 155) (222, 188)] Assuming timestamp clock = 40.00 MHz Green = injected pixels						
Row	Col	LE	TE	ΔLE	ΔTE	ΔTS[25ns] TS[25ns]
140	217	12	29	124	123	5627.0000 635972.0000
140	217	8	25	124	124	5628.0000 641600.0000
155	218	60	60	52	35	35.0000 641635.0000
188	222	59	60	127	0	0.0000 641635.0000
155	218	115	115	56	55	55.0000 641690.0000
188	222	114	115	127	0	0.0000 641690.0000
155	218	42	43	56	56	55.0000 641745.0000
188	222	42	42	0	127	0.0000 641745.0000
140	217	4	21	90	107	5482.0000 647227.0000

(a) An example of the time quantity used in the analysis.



(b) An example of the LE(hit)-TE(previous hit) histogram.

Figure 5.36: Some results of the cross-talk studies.

As already stated, we run several tests varying the number of pixels to read, the value of the readout registers, different combination of hot and good pixels and also different spatial location of them in the matrix to exclude the possibility that the problem was related to particular columns. All results are in agreement with the interpretation explained above.

?????...

Furthermore it has been tried to estimate the height of the induced signal from the threshold of the hot pixel. For this reason we have tried different setting of the currents cited above to make a pixel *hot* in order to understand when the induced signal went above the threshold.

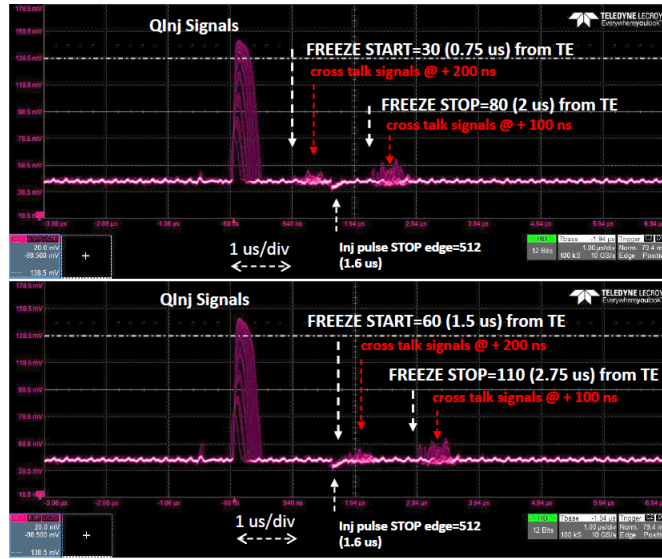


Figure 5.37: Cross-talk of the FREEZE signal on oscilloscope's analog output, for different value of FREEZE\_START\_CONF register.

We have found that the signal could (may) correspond to  $100/150 e^-$ .  
??????

In figure on the current page an analog acquistion of the readout signals taken by an oscilloscope.

In these tests one pixel was injected from 0 to 140 DAC (in the acquisition it can be seen in the increasing signal height). There are two different group of spikes: the first which is smaller and represent the cross-talk from the raising of the FREEZE signal and the second, larger and corresponding to the cross talk from the falling edge of the same signal. Moreover it's possible to see that in the two different pictures, the cross talk signals move according to the different settings of the FREEZE START/STOP edge.

#### 5.6.4 Mitigation

As seen in the previous, the problem of the hot pixel is tied to the induction signal produced during the readout, which cause cross-talk. It becomes even more serious when there is a grater dispersion threshold.

Potentially every pixel could become *hot* if its threshold is lower than the height of the cross-talk signal, since the FREEZE is sent across the entire matrix.

As an example, in figure on the following page it si possible to compare the behaviour of pixel (218, 123) for different register settings adopted in order to reduce the threshold.

##### Threshold trimming

Therefore a possible treatment could be related to the threshold tuning, explained in section (?? on page ??), which could allow to make the pixel threshold more uniform (less threshold dispersion) and simultanously to target a value greater than the induced signals.

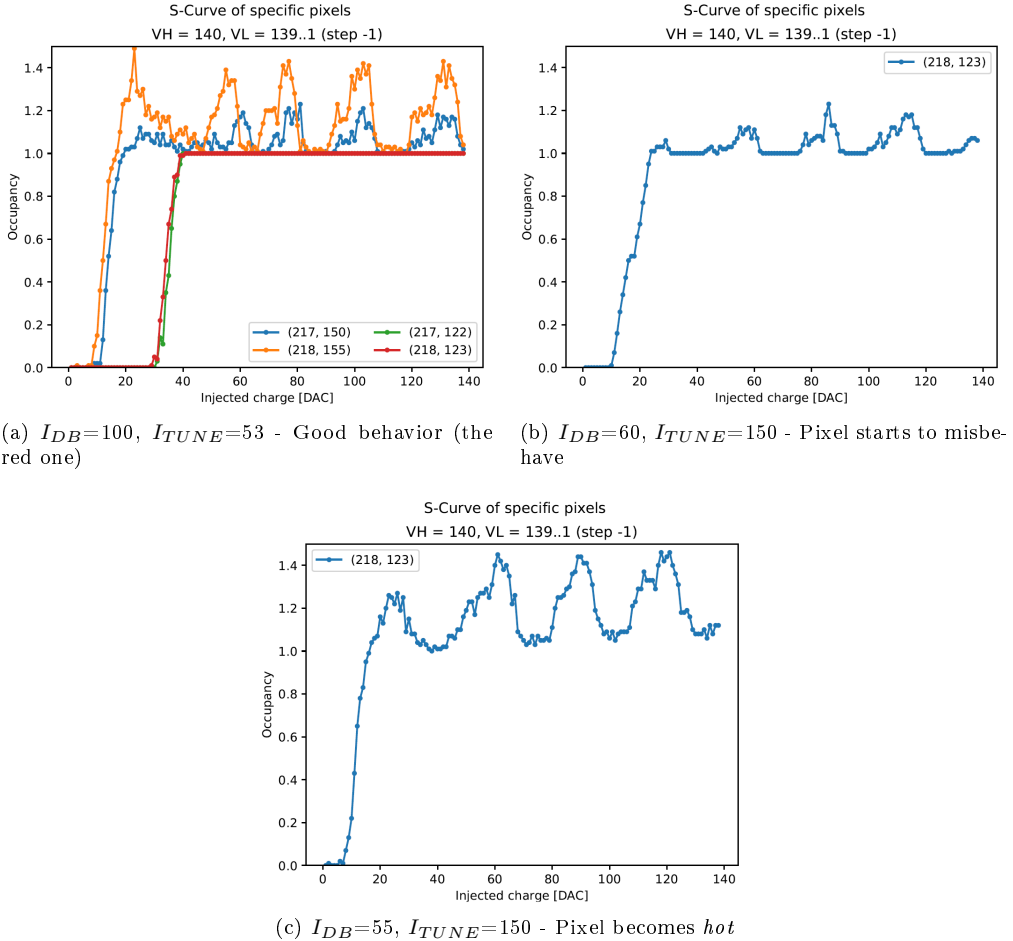


Figure 5.38: S-curve of the pixel (218, 123) for different register settings.

In figure on the following page an example of the results obtained.

It's evident the reduction of the tail in the threshold distribution, in fact the dispersion is reduced by 56%. Also the hot pixels decrease from 18% to 1.2% of the total number of pixels studied. We can also notice that the peak at 0 threshold disappears.

### Bias Voltage

Moreover it has been tried to increase the voltage bias of the all matrix, too. We remember that all previous test has been run with  $P_{WELL}/P_{SUB}$  set to -3 V. This value was increased to -6 V and indeed there were some improvements. In fact increasing the bias, we expected a decrease of the diode capacitance thus higher gain and lower thresold dispersion. In addition the coupling with the cross talk signal is reduced too and so the induced signal height.

In figure on the next page a comparison between the threshold distribution respectively at -3 V and -6 V, with same registers setting and without tuning.

At higher bias voltage not only is the threshold lower (higher gain), but also its dispersion, as expected. And despite that there are fewer hot pixels: 1.3% at -6V against 17% at -3 V. Also

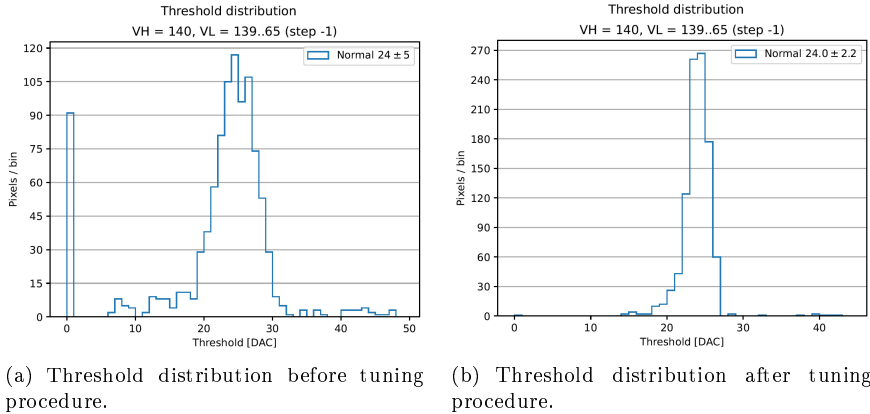
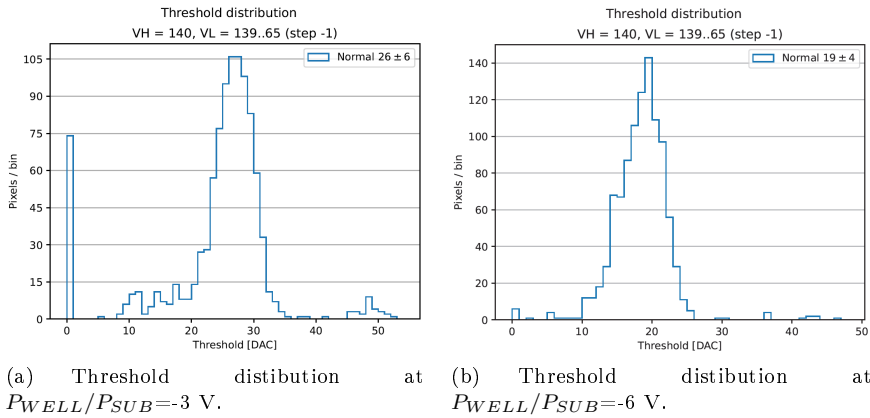


Figure 5.39: Threshold tuning to reduce hot pixels.



here there is clear a reduction of the threshold distribution tail.

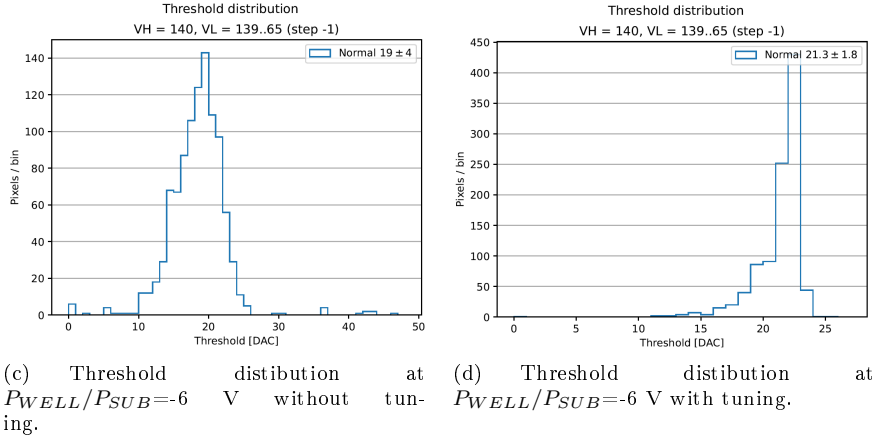
#### 5.6.4.1 Final results?

Eventually the final results obtained with both threshold tuning and a bias voltage on  $P_{WELL}/P_{SUB} = -6$  V.

As we can see in figure on the following page, the threshold dispersion decreases together with the number of the hot pixels. In fact without the tuning, there are 1.3% of them, instead with tuning procedure there are none at all.

## 5.7 Test Beam results

This full characterization of the chip allowed to interpret data collected during the Test Beam done in Desy in June 2022. Several measurements have been taken, among which: pixel response, noise level, cluster signal, full depletion depth, voltage scan and angular scan. In particular the aim was to study electrical characteristics and hit detection efficiency of unirradiated modules.



### 5.7.1 Experimental apparatus and DUTs

The measurements have been performed in a 4 (or 5) GeV electron beam at DESY II testbeam facility at DESY, Hamburg. The experimental apparatus consisted of a beam telescope, a Trigger Logic Unit to provide trigger and control signals employed during test beams, a scintillator trigger and a rotation-translation stage on which install the device under test. (figure on the current page).

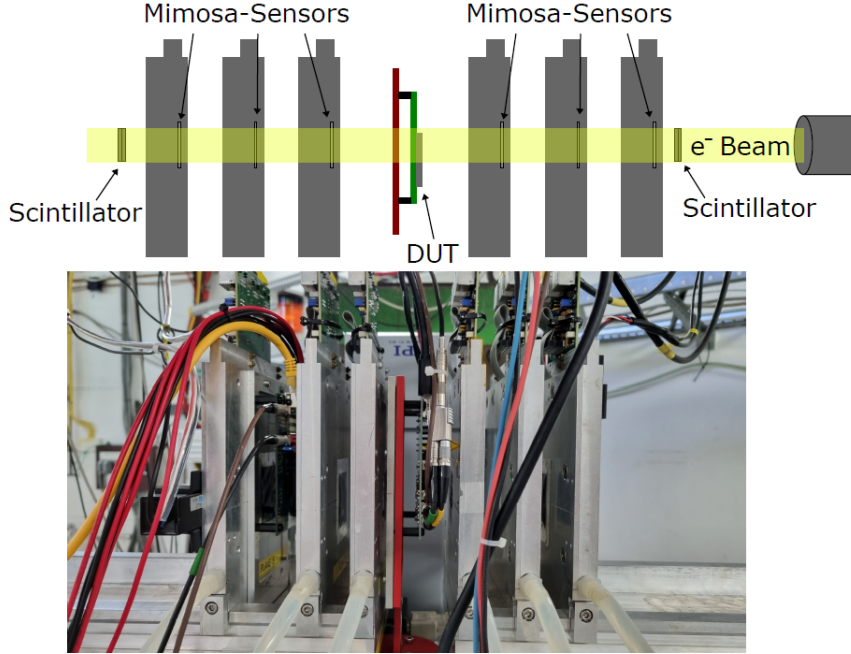


Figure 5.40: Test Beam experimental apparatus.

Three different modules have been tested with different sensor geometry, among which the chip W14R12 that we have studied in depth through laboratory measurements. All results

described in previous sections have been crucial to interpret data obtained during these tests.

In the following we will briefly mention the results obtained.

### 5.7.2 Hit detection efficiency measurements

Initially a depletion depth study have been done and with a voltage bias of -3 V (Normal and Cascode FE), for the chip W14R12 resulted  $33\mu\text{m} \pm 0.04$  (stat.)  $\pm 2.53$  (sys.).

Voltage scan measurements have been performed for both the two type of pixel couplings, such as DC and AC coupled. For the latter, only some first results have been obtained.

#### Normal FE

In figure on this page are reported results obtained for **Normal FE** of all modules. As expected, efficiency and clusters grow as the bias voltage is increased.

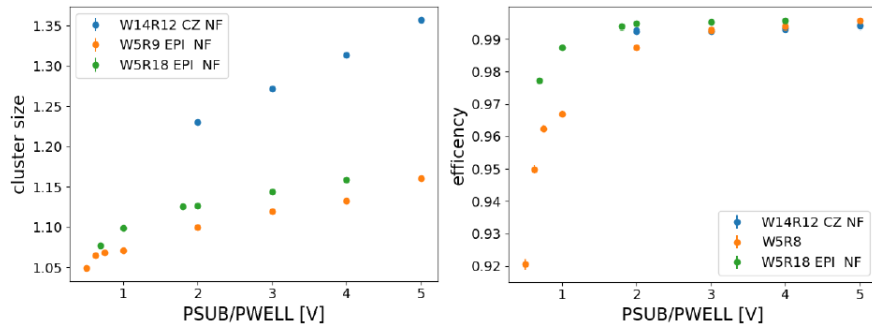


Figure 5.41: Cluster size and efficiency results for Normal FE.

#### Cascode FE

Same trends for **Cascode FE** are shown in figure on the current page.

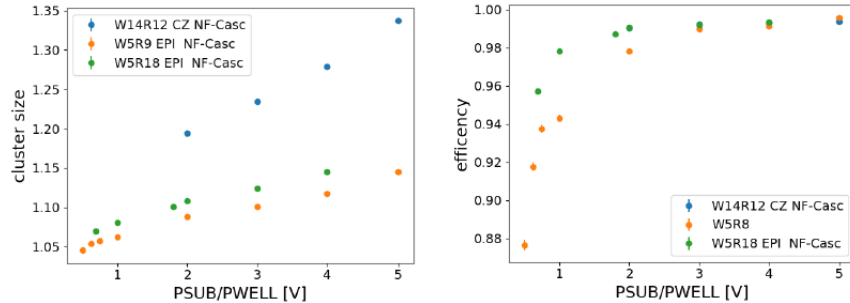


Figure 5.42: Cluster size and efficiency results for Cascode FE.

In particular in figure on the following page are reported the hit map efficiency for DC-coupled pixels for the W14R12 chip, which includes Normal and Cascode FE.

#### HV Casc. FE

#### HV FE

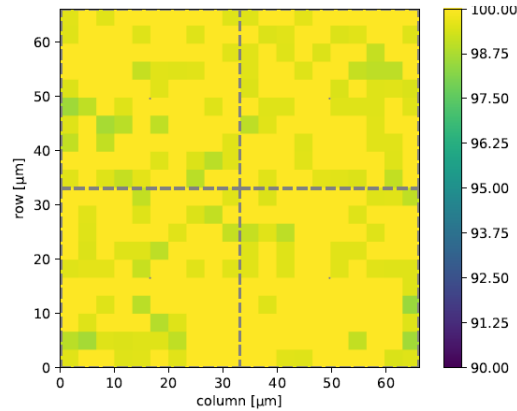


Figure 5.43: Efficiency for DC-coupled pixel of W14R12 chip:  $(99.79 \pm 0.10)$  %

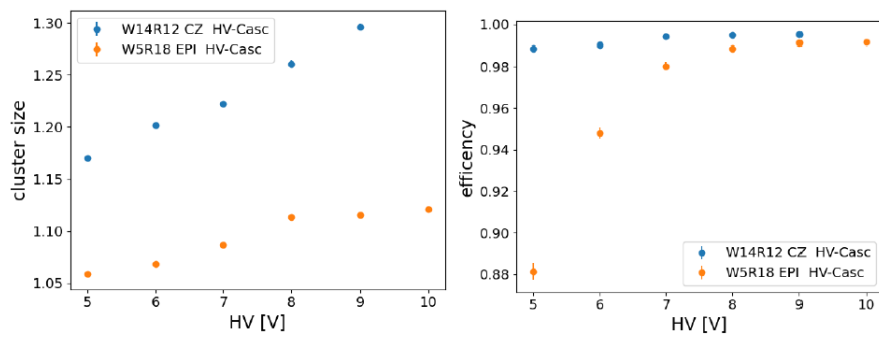


Figure 5.44: Cluster size and efficiency results for HV Cascode FE.

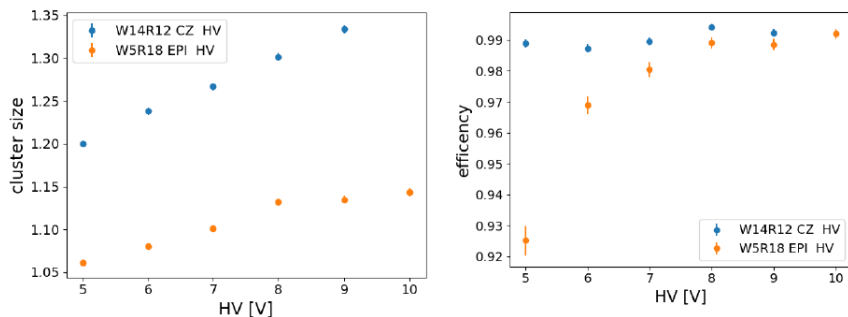


Figure 5.45: Cluster size and efficiency results for HV FE.

## 6. Conclusions

# Bibliography

- [1] E. Kou et al. The Belle II Physics Book. *Progress of Theoretical and Experimental Physics*, 2019(12), December 2019.
- [2] Yukiyoshi Ohnishi et al. Accelerator design at SuperKEKB. *PTEP*, 2013:03A011, 2013.
- [3] A. Natochii et al. Beam background expectations for Belle II at SuperKEKB. In *Snowmass 2021*, 3 2022.
- [4] M. Baszczyk et al. SuperB Technical Design Report. 6 2013.
- [5] Francesco Forti. Snowmass Whitepaper: The Belle II Detector Upgrade Program. In *Snowmass 2021*, 3 2022.
- [6] Maurice Garcia-Sciveres and Norbert Wermes. A review of advances in pixel detectors for experiments with high rate and radiation. *Rept. Prog. Phys.*, 81(6):066101, 2018.
- [7] Hermann Kolanoiski and Norbert Wermes. 1Introduction. In *Particle Detectors: Fundamentals and Applications*. Oxford University Press, 06 2020.
- [8] L. Greiner, E. C. Anderssen, H. G. Ritter, J. Silber, T. Stezelberger, X. Sun, C. Q. Vu, H. H. Wieman, J. Schambach, and M. Szelezniak. A MAPS based pixel vertex detector for the STAR experiment. *PoS*, Vertex2012:010, 2013.
- [9] B Abelev et al. Technical Design Report for the Upgrade of the ALICE Inner Tracking System. *J. Phys. G*, 41:087002, 2014.
- [10] Gianluca Aglieri Rinella. The ALPIDE pixel sensor chip for the upgrade of the ALICE Inner Tracking System. *Nucl. Instrum. Meth. A*, 845:583–587, 2017.
- [11] W. Snoeys et al. A process modification for CMOS monolithic active pixel sensors for enhanced depletion, timing performance and radiation tolerance. *Nucl. Instrum. Meth. A*, 871:90–96, 2017.
- [12] M. Barbero et al. Radiation hard DMAPS pixel sensors in 150 nm CMOS technology for operation at LHC. *JINST*, 15(05):05, 2020.
- [13] K. Moustakas et al. Development in a Novel CMOS Process for Depleted Monolithic Active Pixel Sensors. In *2017 IEEE Nuclear Science Symposium and Medical Imaging Conference*, page 8533114, 2017.
- [14] I. Caicedo et al. The Monopix chips: Depleted monolithic active pixel sensors with a column-drain read-out architecture for the ATLAS Inner Tracker upgrade. *JINST*, 14(06):C06006, 2019.

- [15] Magdalena Munker, Mathieu Benoit, Dominik Dannheim, Amos Fenigstein, Thanushan Ku-gathasan, Tomer Leitner, Heinz Pernegger, Petra Riedler, and Walter Snoeys. Simulations of CMOS pixel sensors with a small collection electrode, improved for a faster charge collection and increased radiation tolerance. *JINST*, 14(05):C05013, 2019.
- [16] Alessandra Fantoni. Upgrade of the ALICE inner tracking system: Construction and commissioning. *Phys. Scripta*, 95(8):084011, 2020.